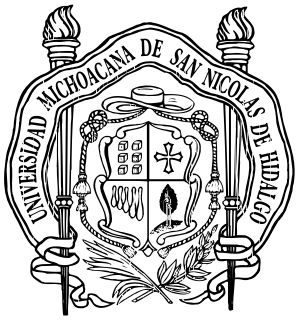


UNIVERSIDAD MICHOACANA DE

SAN NICOLÁS DE HIDALGO

FACULTAD DE INGENIERÍA ELÉCTRICA
DIVISIÓN DE ESTUDIOS DE POSGRADO

# "Electric power systems state estimation using SCADA and PMU measurements"

by
Boris Adrián Alcaide Moreno

A thesis submitted in fulfilment of the requirements

for the degree of

**Doctor of Science in Electrical Engineering**

Advisor
Dr. Claudio Rubén Fuerte Esquivel

MORELIA, MICHOACÁN February 2016

# ELECTRIC POWER SYSTEMS STATE ESTIMATION USING SCADA AND PMU MEASUREMENTS

Los Miembros del Jurado de Examen de Grado aprueban
la **Tesis de Doctorado en Ciencias en Ingeniería Eléctrica Opción en Sistemas Eléctricos**
de ***Boris Adrian Alcaide Moreno***

Dr. Fernando Ornelas Tellez
*Presidente del Jurado*

Dr. Claudio Rubén Fuerte Esquivel
*Director de Tesis*

Dra. Elisa Espinosa Juárez
*Vocal*

Dr. Jaime Cerda Jacobo
*Vocal*

Dr. Arturo Roman Messina
*Revisor Externo* (CINVESTAV, Guadalajara)

Dr. Félix Calderón Solorio
*Jefe de la División de Estudios de Posgrado*
*de la Facultad de Ingeniería Eléctrica. UMSNH*
*(Por reconocimiento de firmas)*

UNIVERSIDAD MICHOACANA DE SAN NICOLÁS DE HIDALGO
Febrero 2016

*To my wife Maryuli, my daughter Sofía*

*my parents Benjamin and Imelda for their love and incentive...*

# *Abstract*

This thesis proposes an approach to incorporate the mathematical models of wind turbine generators, automatic load frequency controls as well as voltage magnitude and frequency dependent loads into a weighted least squares-based state estimation algorithm suitable for the analysis of flexible AC transmission systems. As opposed to conventional static state estimators, where the inclusion of these electric components has been neglected so far, the proposed approach permits the determination of the steady state operation of a power system in the event of a supply-demand unbalance by estimating the magnitude of the frequency deviation from its nominal value. The state estimation is based on measurements related to those that should be obtained by a Supervisory Control and Data Acquisition (SCADA) system and Phasor Measurement Units (PMU). For purpose of this thesis, the set of values associated with SCADA measurements and PMU measurements are generated from a power flow analysis of the network under study. The computational burden of processing a large set of measurements collected from large-scale power systems is reduced by performing a multi-area state estimation based on measurements provided by a SCADA system and phasor measurement units.

This thesis also proposes a novel tracking state estimator which simultaneously processes SCADA measurements as and when they arrive to the control center along with a limited number of synchrophasor measurements. The time skew effects are reduced by only processing the SCADA measurements received since the last execution of the estimator. In order to assure observability, after each execution all SCADA measurements are forecasted and used as pseudo-measurements in the next estimation. An event detection analysis is performed for assessing if the system is operating in its quasi-static state; if so, an innovation analysis is then performed for identifying and eliminating grossly inaccurate measurements. Lastly, the system state is estimated by solving a constrained least-squares optimization problem by using Hachtel's augmented matrix method. In order to improve the tracking state estimation, the option of having time-tagged SCADA measurements is also considered in order to have a larger number of measurements associated with the real system's operation state at a given time.

# *Resumen*

En esta tesis se propone un método para incorporar los modelos matemáticos de generadores eólicos, controles de frecuencia, así como también cargas dependientes de voltaje y frecuencia en un algoritmo de mínimos cuadrados ponderados desarrollado para el análisis de los sistemas de transmisión flexible de corriente alterna. A diferencia de los estimadores de estado estático convencionales, donde la inclusión de estos componentes eléctricos no habia sido considerado hasta ahora, la investigación propuesta permite la determinación de la operación en estado estacionario de un sistema de potencia en el caso de un desequilibrio de oferta y demanda mediante la estimación de la magnitud de la desviación de frecuencia a partir de su valor nominal. Los estimadores de estado utilizan mediciones obtenidas mediante un sistema de control supervisorio y adquisición de datos (SCADA) y unidades de medición de fasores (PMU), sin embargo, para propósito de esta tesis, el conjunto de valores asociados con las mediciones SCADA y las mediciones de PMUs se generan a partir de un análisis de flujo de potencia de la red bajo estudio. La carga computacional de procesar un amplio conjunto de mediciones se reduce mediante la implementación de una estimación de estado multi-área.

Se propone además, un nuevo estimador de estado de seguimiento que procesa simultáneamente mediciones SCADA cuando estas llegan al centro de control, junto con un número limitado de mediciones de sincrofasores. Solamente se procesan las mediciones SCADA recibidas desde la última ejecución del estimador con el objetivo de evitar procesar información recolectada mucho tiempo atras, y esto degrade el desempeño del estimador de estado. Con el fin de asegurar observabilidad, después de cada ejecución del estimador, se calcula una pseudomedición para cada medición SCADA. Además, se realiza un análisis de detección de eventos para evaluar si el sistema está funcionando en su estado cuasi-estático; de ser así, entonces se realiza un análisis de innovación para identificar y eliminar las mediciones erroneas. Por último, el estado del sistema se calcula mediante la resolución de un problema de optimización de mínimos cuadrados ponderados utilizando el método de la matriz aumentada de Hachtel. Con el fin de mejorar la estimación de estado de seguimiento, se considera la opción de tener mediciones SCADA con estampa de tiempo.

**Palabras clave:** Estimación de estado, SCADA, PMU, seguimiento, estimador de seguimiento.

# *Acknowledgements*

First of all, I am deeply grateful to my research advisor, PhD. Claudio Rubén Fuerte Esquivel for giving me the opportunity and confidence to work with him throughout this research and from whom I have learnt so much. I would like to express my profound gratitude, and sincere thanks to him for his guidance, invaluable advice and continuous encouragements throughout these years.

Equally thankful PhD. Thierry Van Cutsem for having facilitated my research internship in the University of Liege which played a crucial role during this research work, his research expertise has undoubtedly nurtured my professional career. Thanks to PhD. Mevludin Glavic for their valuable guidance I received during the course of the research internship. Thanks also to the Prof. Van Cutsem's research group who helped me so much since my first days of arrival to Liege city.

Thank to DSc. Enrique A. Zamora-Cardenas for his support in the publication of two journal papers.

I express my gratitude to the faculty and teaching staff of UMSNH.

The National Council for Science and Technology (CONACyT) also deserves my recognition and acknowledgment for the financial support throughout my doctoral study.

Thank all the people who made this possible.

Boris Alcaide, February 2016.

# Contents

# List of Figures

# List of Tables

# Abbreviations

| | |
|---|---|
| **AC** | **A**lternating **C**urrent. |
| **ALFC** | **A**utomatic **L**oad **F**requency **C**ontrol. |
| **DFIG** | **D**oubly-**F**ed **I**nduction **G**enerator. |
| **EMS** | **E**nergy **M**anagement **S**ystems. |
| **FACTS** | **F**lexible **AC** **T**ransmission **S**ystems. |
| **FSWG** | **F**ixed-**S**peed **W**ind **G**enerator. |
| **GPS** | **G**lobal **P**ositioning **S**ystem. |
| **GR** | **G**lobal **R**eference. |
| **HL** | **H**olt's **L**inear method. |
| **LTC** | **L**oad **T**ap **C**hanger. |
| **MAE** | **M**ean **A**bsolute **E**rrors. |
| **MAPE** | **M**ean **A**bsolute **P**ercentage **E**rrors. |
| **MASE** | **M**ulti-Area **S**tate **E**stimator. |
| **OEL** | **O**ver-**E**xcitation **L**imiter. |
| **PF** | **P**ower **F**low. |
| **PMSG** | **P**ermanent **M**agnet **S**ynchronous **G**enerator. |
| **PMU** | **P**hasor **M**easurement **U**nits. |
| **PS** | **P**hase **S**hifter. |
| **RTU** | **R**emote **T**erminal **U**nits. |
| **SCADA** | **S**upervisory **C**ontrol **a**nd **D**ata **A**cquisition. |
| **SE** | **S**tate **E**stimator. |
| **SSWG** | **S**emi-variable **S**peed **W**ind **G**enerator. |
| **SVC** | **S**tatic **V**ar **C**ompensator. |
| **TCSC** | **T**hyristor **C**ontrolled **S**eries **C**ompensator. |

| | |
|---|---|
| **TSE** | **T**racking **S**tate **E**stimation. |
| **UPFC** | **U**nified **P**ower **F**low **C**ontrollers. |
| **VSWG** | **V**ariable-**S**peed **W**ind **G**enerators. |
| **WECS** | **W**ind **E**nergy **C**onversion **S**ystems. |
| **WLS** | **W**eighted **L**east **S**quare. |
| **WTG** | **W**ind **T**urbine **G**enerators. |

# Nomenclature

| | |
|---|---|
| $\boldsymbol{e}$ | Vector of measurement errors. |
| $\boldsymbol{g}$ | Matrix of partial derivative of the objective function with respect to the state vector. |
| $\boldsymbol{h}$ | Vector of mathematical models of each device measurements. |
| $\boldsymbol{r}$ | Measurement residual vector. |
| $\boldsymbol{x}$ | State vector |
| $\boldsymbol{z}$ | Vector of SCADA or PMU measurements. |
| $\bar{\boldsymbol{z}}$ | Vector of SCADA Pseudomeasurements. |
| $\boldsymbol{G}$ | Gain matrix. |
| $\boldsymbol{H}$ | Matrix of partial derivative of mathematical model of measurements $h$ with respect to the state vector. |
| $\boldsymbol{I}_{branch,r}$ | Real part of current flow. |
| $\boldsymbol{I}_{branch,i}$ | Imaginary part of current flow. |
| $J$ | Objective function to minimize. |
| $N$ | Number of buses in the system. |
| $N_{CBB}$ | Number of common boundary buses for two control areas. |
| $\boldsymbol{P}_{branch}$ | Active power flow. |
| $\boldsymbol{Q}_{branch}$ | Reactive power flow. |
| $\boldsymbol{P}_{inj}$ | Active power injection. |
| $\boldsymbol{Q}_{inj}$ | Reactive power injection. |
| $\boldsymbol{R}, \boldsymbol{U}, \boldsymbol{M}$ | Error covariance matrices for SCADA, PMU and SCADA pseudo-measurements, respectively. |
| $\boldsymbol{S}$ | Residual covariance matrix. |
| $\boldsymbol{T_i}$ | Time between two communication of RTU and SCADA system. |

| | |
|---|---|
| $\boldsymbol{T_r}$ | Period of time between two consecutive TSE executions. |
| $\boldsymbol{V}$ | Voltage magnitude. |
| $\boldsymbol{W}$ | Weight matrix. |
| $\chi^2_{(m-n),\alpha}$ | Chi-square distribution with $(m-n)$ degrees of freedom and a significance value $\alpha$. |
| $\boldsymbol{\epsilon}$ | Vector of uncorrelated measurement residuals. |
| $\boldsymbol{\epsilon^N}$ | Vector of normalized residuals. |
| $\phi$ | Shift angle added to all phase angles estimated with respect to a local reference to produce a coherent state in two control areas. |
| $\boldsymbol{\sigma}$ | Vector of standard deviation of measurements. |
| $\boldsymbol{\tau_i}$ | Transmission delay of substation $i$. |
| $\Delta f$ | Frequency deviation. |
| $\boldsymbol{\theta}$ | Voltage phase. |

# List of publications

## Journal Papers


[1] E.A. Zamora-Cárdenas, **B.A. Alcaide-Moreno** and C.R. Fuerte-Esquivel, "State estimation of flexible AC transmission systems considering synchronized phasor measurements" Electr. Power Syst. Res. 106 (August (7)) (2014) 120–133.

[2] **B.A. Alcaide-Moreno**, Luis M. Castro, C.R. Fuerte-Esquivel and E.A. Zamora-Cárdenas "Generalized State Estimation of Power Systems Considering Wind Generators and Primary Frequency Control", Electric Power Components and Systems, 43(13):1534–1547, 2015.

[3] **Boris A. Alcaide-Moreno**, Thierry Van Cutsem, Mevludin Glavic and Claudio R. Fuerte-Esquivel, "A Tracking Power System State Estimation from Multirate Measurements" submitted to IEEE Trans. on Smart Grid, October 2015.


## Conference Papers


[1] **Boris A. Alcaide-Moreno**, Thierry Van Cutsem, Mevludin Glavic and Claudio R. Fuerte-Esquivel, "Hybrid processing of SCADA and synchronized phasor measurements for tracking network state" in Proceedings of IEEE Power and Energy Society General Meeting (PESGM 2015), Denver CO, USA, July 2015.

# Chapter 1

# Introduction

## 1.1 Overview of state estimation in electric power systems

Since its introduction in the late 1960s, the state estimator (SE) has become the core of modern energy management systems (EMS) used by operators to maintain the power system in its normal operation state. Based on the continuous monitoring of the system, the SE provides accurate information about the power system state at a given point of time, and a reliable data input for other EMS application functions such as online power flow and optimal power flow studies, economic power dispatch, security analysis, as well as automatic generation and voltage control [1].

The SE comprises basically the following functions [2]:

1. **Measurement prefiltering**: Detect and discard measurements that are clearly wrong (negative voltage magnitudes, out of range power flows, etc.).
2. **Topology processor**: Determines the bus bar connectivity, the status of switching devices and the physical layout of substations in order to build the electrical network model (electrical nodes, nonenergized islands, etc.).
3. **Observability analysis**: Using the available measurements, determines if the whole system is observable or identifies the observable islands.
4. **State estimation**: Computes the state variables (bus voltage magnitude, phase angles and transformer/phase shifter tap positions), that best fits the

telemetered analog measurements (line flows, injections, voltage magnitude, and transformer/phase shifter tap positions, etc.) for a given set of network parameters and network connectivity.

5. **Bad data processor**: This function detects, identified and removed errors in the set of measurements.

Figure 1.1 shows the functional relationships and data exchanges among these blocks [2]:

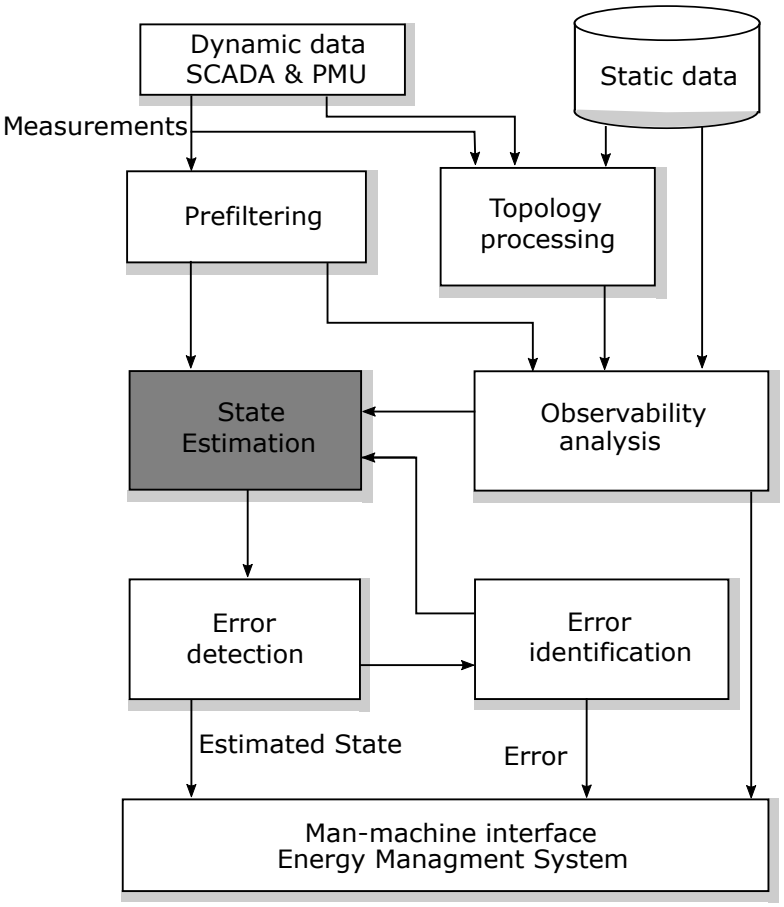


FIGURE 1.1: State estimator process.

Furthermore, there are different kinds of state estimation techniques according with the state variables (quantities) to estimate [3], a basic classification is shown in Fig. 1.2 and can be briefly described as follows:

1. **Static State Estimation**: refers to an optimization procedure in order to obtain all voltage phasors of the network buses at a given point in time, by processing a single set of redundant measurements and other available information.

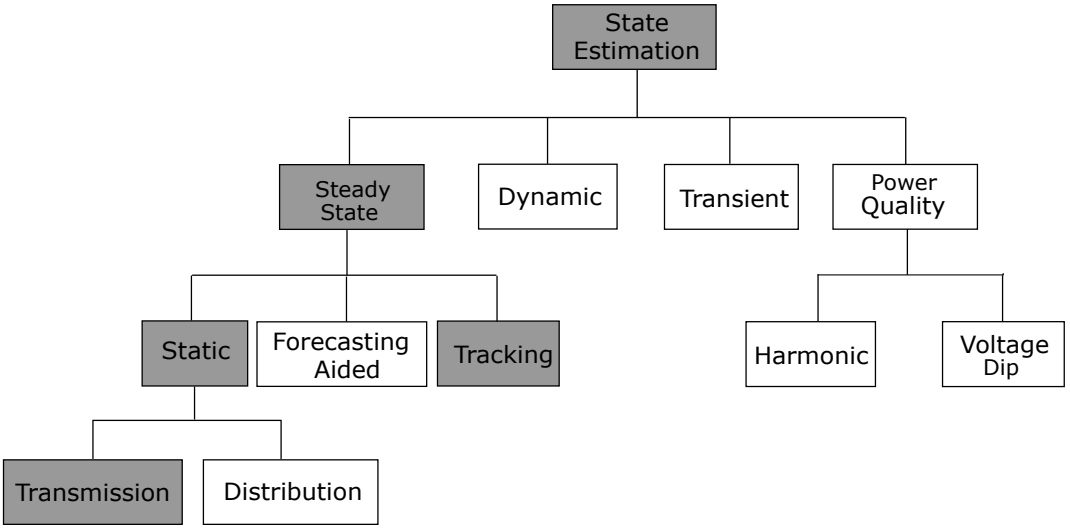


FIGURE 1.2: State estimation classification

2. **Forecasting-Aided State Estimation**: this algorithm incorporates the "dynamic" model for assessing the time behavior of the system states through a Kalman filter-based state estimation which forecasts changes in time of static state variables when a new set of measurements has not been processed.

3. **Tracking State Estimation**: this method is designed to track network's static state evolution after a disturbance based on a sequential application of a static state estimator and upgraded sets of measurements.

4. **Dynamic State Estimation**: estimates *dynamics* states of power system, e.g. the values of rotor angle and speed of generators, along with static states in order to track the dynamic state of the system.

5. **Transient State Estimation**: while transient simulation is used to analyze the consequences of a disturbance on a power system states (voltage, current, etc.), transient state estimation is exploited to identify the cause of transient change in system parameters.

6. **Harmonic State Estimation**: generates the best estimate of static or time-varying harmonics levels from a limited number of measured harmonic data corrupted with measurement noise..

7. **Voltage dip estimation**: it is an extension of state estimation techniques to estimate the number of voltage dips or voltage sags as well as the duration of these kinds of disturbances at a given point of the network.

The present research work focuses on the *static state estimation* and the *tracking state estimation* in electric power transmission networks.

## 1.2 Research motivation

From the smart grid initiative viewpoint, applying advanced sensing, measurement and intelligent control devices in existing electric power systems will be necessary to support decisions in control centers concerned with increasing the utilization, efficiency, quality and security of the power systems. These advanced applications will transform the way in which most power systems have been operated [4]. In order to achieve this goal, phasor measurement units (PMUs) and flexible AC transmission systems (FACTS) controllers have been installed at selected substations for accurately monitoring and controlling the state of the power system as the operating conditions change during its daily operation [4, 5].

PMUs are devices that provide positive sequence phasors of voltage and currents from the measured voltage and current waveforms, respectively. Since these measurements are sampled at the same time using a common synchronizing signal from the global positioning system (GPS) satellites [6, 7], all positive sequence phasors, referred to as phasor measurements, at different substations are also synchronized with respect to that time reference to create a coherent picture of the system state at a given instant [8]. On the other hand, FACTS controllers is another technology that permits direct control of active and reactive power flows as well as voltage magnitudes in an AC network, such that the use of these controllers will be very important in the smart operation of future transmission networks to satisfy the requirements of fast wide area control actions [5].

Even though the number of PMUs and FACTS controllers installed in practical systems has gradually increased, the transition for transforming the present transmission networks and control centers into smart infrastructures will require many years to accomplish and must be carefully planned and executed [5]. However, an important step forward can be done in this long awaited transition if the software used to operate electric power systems is upgraded considering the operation characteristics of the existing PMUs and FACTS devices already installed in the network. Arguably, the estimation of the network's states constitutes the main core of the on-line security analysis and other energy management system applications [9], such that the development of suitable strategies to upgrade state

estimators (SEs) is one of the main objectives in the transition toward smart control centers and transmission networks [10]. Until today most of the SEs used in control centers have been designed based on a centralized solution scheme: the state estimation of the entire system is performed by simultaneously processing all wide area measurements provided by a Supervisory Control and Data Acquisition (SCADA) system. Recent studies on the further development of SEs show two clear directions: (i) The development of distributed state estimators [10, 11]; and (ii) the integration of PMUs [12, 13] and FACTS controllers [14, 15] into the conventional state estimation approaches. In the first case, which is addressed in this thesis, the whole system is first decomposed into several control areas and a local state estimation is carried out for each area. All local estimations are then gathered to generate a single coordinated estimation for the entire power system [10, 11]. The second direction of research, which is also addressed in this thesis, has shown that the incorporation of phasor measurements into existing SEs improves the speed and accuracy of the estimation, improves the network observability, provides better bad data processing and enhances the ability to provide a better initialization for the iterative process required to estimate the current operation state [12, 13].

In addition to the mentioned above, nowadays wind energy conversion systems (WECS) are the fastest growing type of renewable energy resources used in electric power systems for generating electricity [16]. From the power system operation viewpoint, however, two of the major challenges in using wind as a source of power are associated with the unpredictable nature of wind speed, which translates into generation output variability, and with the possible unavailability of wind power when it is required. Consequently, the quantification of the impact that the high-level of penetration of wind turbine generation will cause on the operation of power systems is of paramount importance.

In this context, and considering the technical and business challenges that the increasing penetration of the wind turbine generators (WTGs) will produce in the operation of power systems, the integration of WTGs' models into SE algorithms is crucial for the accurate real-time information about the power system operation and for estimating WTGs' state variables along with the power system's state variables. The practical solution of this challenging problem is the main motivation of this thesis.

On the other hand, from the system operator viewpoint, the real-time (for instance $< 1s$) monitoring of the steady-state voltage is extremely valuable to know power

system time-varying conditions [1]. In this context, dynamic changes in the state, resulting from the continuous variation of loads and renewable generation, or the occurrence of disturbances, need to be monitored continuously for early detection of potential operational problems in order to perform the corresponding preventive or corrective remedial actions which steer the system to a normal operation state. This motivates the execution of power system state estimations at shorter intervals of time, using all the available measurements, for better situational awareness in smart grids. In this sense, tracking state estimation can be used to track network state evolution at a much higher rate than static state estimation.

## 1.3 State of the art

### 1.3.1 Static State Estimation

An example of how PMU measurements can be employed without modifying the conventional state estimation approach is reported in [12]. In this proposal, the estimation obtained from traditional measurements is improved by a linear SE that only uses synchronized measurements in a post-processing step. Alternative hybrid distributed SEs that combine both SCADA and synchronized measurements are proposed in [17, 18]. Since the phase angles estimated in each control area are measured with respect to their own local reference bus, a global reference must be specified to merge in a coordinated way all local estimations through the computation of a reference angle difference, such that all voltage phase angle estimations are in the same reference. In these proposals, the voltage phasor measurements are represented in polar coordinates to maintain the linear relation between these measurements and state variables. Details of how the reference angle difference can be computed are given in [19], while the effect of the PMU measurements on the choice of the reference bus is discussed in [20]. On the other hand, hybrid nonlinear SEs based on a centralized scheme are proposed in [15, 21, 22] where both voltage phasors and current phasors measurements are considered in the formulation. In [13], the current phasor measurements are represented in rectangular coordinates and are related to the state variables by a nonlinear function. Furthermore, the reference angle is chosen in one of the buses with PMUs under the assumption that the PMU functions perfectly. In order to avoid the selection of a reference angle at one of the network's buses, all voltage angles are measured with respect to the time dictated by the GPS satellites [21].

On the other hand, extensive research has been undertaken to develop steady-state mathematical models of FACTS devices which have been integrated into state estimation algorithms [14, 15, 23, 24, 25, 26].

In this context, a state estimation approach for power systems embedded with FACTS devices and multi-terminal DC systems was proposed in [23]. The conventional Weighted Least Square (WLS)method is applied to estimate the equilibrium point of a power system by decoupling the gain matrix into three sets of equations, which are solved sequentially for the state variables of the AC system, DC system and FACTS devices, respectively. Two FACTS devices, namely the Unified Power Flow Controller (UPFC) and the Thyristor Controlled Series Capacitor (TCSC), are considered in the SE formulation. The UPFC is modeled as a controllable series injected voltage source and a controllable shunt-injected current source, whose magnitudes and angles define its state variables. It is assumed that the UPFC is directly connected to the transmission grid, such that the coupling transformers and losses are not considered in the model. Additionally, the constraint of active power balance in the UPFC's DC-link, which must be satisfied unconditionally, is not included in the formulation. On the other hand, the TCSC is modeled as a variable capacitance directly connected to the series impedance of the transmission line. Due to the proposed modeling of FACTS devices, it is not possible to have measurements at the line side node where the controller is connected. Additionally, controllers' operating constraints are not included in the SE formulation. In [27], an unconstrained UPFC controller is modeled by a set of nodal power injections, such that the conventional WLS method is used to estimate the state of the power system considering only the magnitudes and phase angles of nodal voltages as state variables. The proposal does not take into account neither the controller constraints nor the upgrade of its state variables during the iterative process.

An approach to tackle the problem of considering controller's operating constraints is to formulate the state estimation problem as a nonlinear optimization problem with equality and inequality constraints [24, 25, 28, 29, 30]. In [24, 25, 28, 29]; the state estimation of a power system containing UPFCs is formulated as a constrained nonlinear optimization problem, which is solved by means of the primal-dual interior point method. The UPFC is modeled by means of an equivalent circuit consisting of two ideal voltage sources connected to lossless coupling transformers. The magnitude and phase of the shunt and series voltage sources are considered as UPFC's state variables to be estimated. The DC-link active power balance is considered as an equality constraint, while the inequality constraints

are defined by the power limits of converters and voltage magnitudes of the shunt and series voltage sources. The circuit representation of the transmission line compensated by a UPFC is simplified to an equivalent circuit by assuming that the former does not have a capacitive effect. The optimization problem is then formulated as a nonlinear Weighted Least Squares problem in [24, 28] and based on the Weighted Least Absolute Value (WLAV) criterion in [25, 29]. Similarly to [23], the equivalent circuit used in these proposals prohibits measurements at the node where the converter is inserted in series with the line. Furthermore, a UPFC cannot be connected to the same node at which multiple transmission lines are also connected. The proposal described in [30] considers multiple types of FACTS devices, i.e. Static Var Compensator (SVC), TCSC, and UPFC; in addition, the power system's estimation is formulated as a constrained nonlinear optimization problem solved by using the predictor-corrector interior point algorithm. The series connected FACTS devices are modeled including a PI equivalent circuit of the transmission line, such that solely the complex power flow through the sending node of the series controller and receiving node of the transmission line are considered in the SE formulation. In the case of the UPFC, the equation representing the active power transferred between the shunt and series voltage sources is considered an equality constraint, while voltage magnitudes and angles of these sources are the estimated states of the UPFC, whose values are restricted by inequality constraints. The SVC and TCSC are taken to be variable reactances that are adjusted automatically as a function of the firing angle, which is considered as the state variable for both controllers. It should be noted that near the resonant point, small variations of the firing angle will induce large changes in the reactances, which in turn may lead to ill-conditioned controller's power flow equations and Jacobian terms.

Despite that state estimation has become a critical function of the EMS, there are only few proposals that include WTGs in this application [31, 32, 33, 34]. The conventional and simplified resistance-reactance (R-X) models of a fixed-speed wind generator (FSWG) are adopted in [31, 32, 33] and [32, 33, 34], respectively, to estimate the slip of the asynchronous generators along with the nodal voltages using a centralized weighted least square-based (WLS) state estimator. This kind of generator was the most commonly used in the early stages of wind power developments, but is expected to be its use reduced in future years due to the penetration of power electronic-based variable speed WTGs, which present higher efficiency and controllability [35].

Based on the above, this thesis propose the direct integration of both fixed-speed and variable-speed wind generators models into a weighted least squares (WLS)-based state estimator for an accurate estimation of the values of WTGs' state variables together with the power system's state variables. In this context, a unified approach to compute the state variables of WTGs along with the nodal voltage magnitude and angles of the entire network was suggested in [36], and implemented in [37, 38] for several types of WTGs, within the power flow problem perspective; accordingly a similar idea has been adopted in this thesis for estimating the state variables related to the network and WTGs. Since the development of steady state models of WTGs is not new by any means, the detailed steady state mathematical models of WTGs included in the estimator are those previously reported in [37, 38, 39] for the FSWG, the semi-variable speed wind generator (SSWG) as well as two variable-speed wind generators (VSWG) based on a doubly-fed induction generator (VSWG-DFIG) and on a permanent magnet synchronous generator (PMSG), respectively.

In real-time operation, the wind power randomness provokes a generation-load unbalance, causing a deviation of the system's frequency from its nominal value [40]. This frequency deviation could be aggravated by the increasing penetration of variable speed-based WTGs: the converters used in these generators decouple the turbines' rotational speed from the network frequency, which translates into a reduction of the effective inertia response of the overall power system, such that the grid is more susceptible to an imbalance between generation and demand [41]. In this context, the unbalance must be promptly corrected through automatic control actions, being the primary frequency regulation which reacts immediately to reestablish a proper balance at an off-nominal frequency. Bearing this in mind, the second contribution of the proposed approach is that it permits estimating the system operating point after the action of the primary frequency regulation by considering the frequency deviation as a state variable to be estimated. For this purpose, we assume that only conventional generators participate in frequency regulation as well as the voltage and frequency dependence of loads [38, 42].

A hybrid state estimator recently reported in [43], which permits a centralized state estimation of a power system with embedded flexible AC transmission systems (FACTS) controllers based on measurements provided by a supervisory control and data acquisition (SCADA) system and phasor measurement units (PMUs), has been extended for the inclusion of the WTGs and automatic load frequency control (ALFC) models mentioned above. Monitoring large-scale power systems comprising multiple areas, however, requires an enormous computational burden

since the sets of measurements to be processed and state variables to be estimated become extremely large. An approach for alleviating this problem was proposed in [44] as early as 1981 and consisted of decentralizing the estimation in two stages: the power system under study was first decomposed into several control areas, and their corresponding local operation states were estimated; these local estimations were then gathered to generate a single coordinated state estimation for the entire power grid. By following this line of reasoning, several decentralized multi-area state estimators (MASE) have been proposed, according to [45] and the references therein, to reduce the amount of memory requirements and computation time. As a follow-up to this kind of analysis, the concepts of tie-line overlapping areas [45] and common reference shift angle [46] have been merged in our proposal for developing the MASE reported in this thesis. Finally, and to the best of the authors' knowledge, the proposed approach that permits a unified estimation of the operating condition of a power system containing wind farms, FACTS devices and ALFCs, from a given set of measurements provided by a SCADA system and PMUs, has not been reported or examined by past literature and it is also a contribution of this thesis.

### 1.3.2 Tracking State Estimation

Early proposals of Tracking State Estimation (TSE), for better following of the system behavior, can be traced back to [47], [48], [49], and [50] based on the available technology at that time. Those publications suggested the use of a Kalman filter or extended the techniques developed for static estimation to the time-varying case. Slow dynamic changes in the system state can be tracked through Kalman filter-based state forecasting approaches that require a complete set of Supervisory Control And Data Acquisition (SCADA) measurements in order to carry out successive estimations, as proposed in [51] and [52].

Traditionally, measurements used for power system monitoring are collected by low updating rate SCADA systems via remote terminal units (RTUs) [53]. Estimations based on those measurements, however, could not be accurate enough in capturing how the system states evolve in time. On the other hand, Phasor Measurement Units (PMUs), which provide synchronized measurements at 30 or more samples per second, are expected to improve the efficiency and accuracy in which the time-varying nature of the power system is captured [1, 54]. Depending on the number of PMUs installed in the network, linear state estimation [55], a fully dynamic

state estimator [56] or a complete measure of all system state variables could be the foundation to enable a true real-time monitoring [57].

For economic and technical reasons the penetration of PMUs is low and far from being rich enough for ensuring full system observability [54, 57]. Therefore, as long as there are not enough PMUs deployed in power networks, it will be relevant to take advantage of both SCADA and scarce PMU measurements to track the system evolution.

Several approaches combining SCADA and PMU measurements have been proposed to estimate and track the system state. Leaving existing state estimation software unchanged, Ref. [58] proposed a post-processing linear state estimator using synchrophasor measurements to enhance accuracy. Following the idea to keep existing state estimation software unchanged, it was proposed in [59] to process separately SCADA (by existing software) and phasor measurements (as an additional estimation module), with techniques from fusion theory to combine both results. In [60], bus injection estimates obtained from previous state reconstructions were used as pseudo-measurements to restore observability. This approach was extended in [61], by processing at each TSE execution the last received SCADA measurements, the synchrophasor measurements and pseudo-measurements stemming from the previous TSE run.

The idea of combining SCADA and synchrophasor measurements has been further elaborated in a number of recent publications. A weighted least absolute value based tracking estimator has been proposed in [62] that uses the incoming PMU measurements and the last set of estimated SCADA measurements as pseudo-measurements. In [63], a linear state estimation has been proposed assuming a rich deployment of PMUs but not enough to make the system observable; observability is then restored by computing missing measurements using network equations. In [64], missing SCADA measurements are extrapolated through the exponential moving average method between SCADA successive communications, and an optimization problem is solved using an extended Kalman filter. In [65], as in [66], the states of PMU unobservable buses are interpolated taking advantage of regularly updated SCADA measurements [66] or when a disturbance is detected considering recursive a priori state information [65].

The Tracking State Estimator proposed in this thesis extends the work presented in [61, 67], pseudo-measurements are treated in a more uniform manner and their values are obtained by a prediction based on previous TSE results. Furthermore, event detection and innovation analysis are performed to discriminate between a

change in system state and the occurrence of erroneous SCADA measurements. Finally, the exploitation of time-tagged SCADA measurements is also proposed.

## 1.4 Research objectives

There are two main objectives in the present research work, that can be summarized as follows:

1. To develop a decentralized multi-area state estimation (MASE) approach suitable for estimating the steady state operation of a flexible AC transmission system with wind generator devices and imbalances between generation and demand of electric power.

2. To develop a tracking state estimator suitable for assessing how the system states evolve in time based on the processing of both synchronized phasor and SCADA measurements according to as and when they are received in the control center.

## 1.5 Methodology

The following research methodology has been adopted to achieve the objectives set for this research work:

1. To carry out a comprehensive review of the existing literature in the area of FACTS, WG and ALFC with a particular emphasis on the mathematical models.

2. To derive a general set of nonlinear equations relating a set of measurements, provided by a SCADA system and PMUs to the states variable of SVC, TCSC, UPFC, Phase Shifter (PS) and Load-Tap changer (LTC) devices.

3. To develop a complete general set of nonlinear equations relating a set of measurements, provided by a SCADA system and PMUs, to the state variables associated with both fixed-speed and variable-speed wind generators (FSWG, SSWG, VSWG and PMSG).

4. To include the effects of governor characteristics as well as voltage and frequency dependence of loads into the proposed approach to assess the current state of the whole system considering the frequency deviation as a state variable to be estimated.

5. To compute the state variables of both fixed-speed and variable-speed wind generators together with the state variables associated with the power system, FACTS controllers and frequency deviation in a single frame of reference defined by an extended state estimator.

6. To develop a decentralized MASE that requires only information exchange between border buses.

7. To test the performance of the proposed state estimator considering a modified IEEE 118-bus test system.

8. To develop a tracking state estimator (TSE) by processing synchronized phasor and SCADA measurements based on the Hachtel's method.

9. To include a prediction, an innovation analysis and a correction step into the TSE formulation in order to detect and eliminate bad data in the measurements set.

10. To test the proposed TSE in the Nordic system undergoing large disturbances to verify that the proposed method is capable to track the overall network's states evolution.

## 1.6 Thesis contributions

The specific contributions of the proposed approach with respect to other proposals are as follows:

1. Developing a theoretical framework that permits a centralized state estimation of a power system with embedded FACTS controllers considering in a single frame of reference measurements provided by a SCADA system and PMUs as well as all the points mentioned above. In this proposal, a complete general set of nonlinear equations relating current phasor measurements and state variables associated with static var compensators (SVC), thyristor controlled series compensators (TCSC) and unified power flow controllers

(UPFC) are derived from first principles and are directly included into the state estimation problem. Note that despite the number of PMUs installed in the network could permit a direct measurement of the system's state, the operation state of FACTS controllers cannot be directly measured because the PMU measurements and FACTS state variables are related by nonlinear functions. Hence, an iterative process is still necessary to solve the state estimation problem that remains nonlinear. By solving this problem, we cannot only estimate the state variables of both power system and FACTS devices, but we can also determine the controller settings of FACTS devices for a desired operating condition.

2. A new tracking state estimator (TSE) aimed at following some of the dynamics of the network state (bus voltage phasors) by a hybrid processing of SCADA and limited number of synchronized phasor measurements and using a constrained least-squares optimization.

## 1.7 Thesis outline

The remainder of this thesis is organised into 4 Chapters. A brief overview of each one of these Chapters is given below:

**Chapter 2** presents a generalized approach to incorporate into WLS-based static hybrid state estimation different models of FACTS, wind turbine generators, the primary frequency control of generators and a load model depending on voltage and frequency values. This generalized approach is then tested with a multiarea state estimation scheme.

**Chapter 3** details a novel state estimation aimed at tracking the changes of network state. The main feature is the simultaneous processing of measurements gathered at different rates: SCADA measurements are processed as and when they arrive to the control center together with a limited number of synchrophasor measurements.

**Chapter 4** gives the general conclusions of this research work and makes suggestions about related areas that require further investigation.

# Chapter 2

# Static State Estimation

## 2.1 Introduction

A practical approach is proposed in this chapter to incorporate the mathematical models of both fixed-speed and variable-speed wind turbine generators, automatic load frequency controls as well as voltage magnitude and frequency dependent loads into a weighted least squares-based state estimation algorithm suitable for the analysis of flexible alternating current (AC) transmission systems. As opposed to conventional static state estimators, where the combined inclusion of all these electric components has been neglected so far, the proposed approach also permits the determination of the steady state operation of a power system in the event of a supply-demand unbalance by estimating the magnitude of the frequency deviation from its nominal value. Since the state estimation is based on measurements related to those that should be obtained by a supervisory control and data acquisition (SCADA) system and phasor measurement units (PMUs), equations relating SCADA and PMUs measurements to state variables of both fixed-speed and variable-speed wind generators are derived from first principles in order to directly append these equations to the set of measurements used to estimate the equilibrium point of the electric power system. In this context, the proposed approach simultaneously upgrades the estimated values of the state variables of wind generators, FACTS devices and the electric network for a unified estimation of the system state. For the purpose of this chapter, the set of values associated with SCADA measurements (nodal power injections, power flows, and voltage magnitudes) and PMU measurements (voltage and current phasors) are generated from a power flow analysis of the network under study. Furthermore, the synchronized

current phasor measurements are transformed to rectangular coordinates to enhance the convergence properties of the proposed state estimation approach. In this case, the variance of the new set of synchronized measurements is calculated based on the uncertainty propagation theory. Lastly, numerical simulations are reported to demonstrate the effectiveness of the proposed approach.

## 2.2 Mathematical formulation

### 2.2.1 Classical state estimation

Consider a vector $\boldsymbol{z}$ containing the set of $m$ measurements that can be expressed in terms of the $n$ the system states as follows:

$$\boldsymbol{z} = \begin{bmatrix} z_1 \\ z_2 \\ \vdots \\ z_m \end{bmatrix} = \begin{bmatrix} h_1(x_1, x_2, \cdots, x_n) \\ h_2(x_1, x_2, \cdots, x_n) \\ \vdots \\ h_m(x_1, x_2, \cdots, x_n) \end{bmatrix} + \begin{bmatrix} e_1 \\ e_2 \\ \vdots \\ e_m \end{bmatrix} = \boldsymbol{h}(\boldsymbol{x}) + \boldsymbol{e} \tag{2.1}$$

where
$\boldsymbol{h}^T = [h_1(x), h_2(x), \cdots, h_m(x)]$
$h_i(x)$ is the nonlinear function relating the measurement $i$ to the state vector $\boldsymbol{x}$
$\boldsymbol{x}^T = [x_1, x_2, \cdots, x_n]$ is the system state vector
$\boldsymbol{e}^T = [e_1, e_2, \cdots, e_m]$ is the vector of measurement errors

The following assumptions regarding the statistical properties of the measurement errors are also considered in the formulation:

- Errors are distributed according to a normal distribution.

$$f(z) = \frac{1}{\sqrt{2\pi\sigma}} e^{\frac{-\mu^2}{2}} \tag{2.2}$$

- Expected values of all errors are zero, that is, $E(e_i) = 0$, $i = 1, ..., m$.
- Errors are independent each other: $E(e_i e_j) = 0$. Hence,

$$Cov(e) = E\left[e \cdot e^T\right] = \boldsymbol{R} = diag\left\{\sigma_1^2, \sigma_2^2, \cdots, \sigma_m^2\right\} \tag{2.3}$$

If errors are independent, then the joint probability density function of a set of $m$ measurements can be obtained by:

$$f_m(z) = f(z_1)f(z_2)\cdots f(z_m) \tag{2.4}$$

The objective of maximum likelihood estimation is to maximize this function by varying the assumed parameters of the density function, namely its mean $\mu$ and its standard deviation $\sigma$ [53]. The logarithm of the likelihood function $L$ is usually used to simplify the problem:

$$\begin{aligned} L = logf_m(z) &= \sum_{i=1}^{m} logf(z_i) \\ &= -\frac{1}{2}\sum_{i=1}^{m}\left(\frac{z_i-\mu_i}{\sigma_i}\right)^2 - \frac{m}{2}log2\pi - \sum_{i=1}^{m} log\sigma_i \end{aligned} \tag{2.5}$$

The maximum likelihood estimation will maximize the likelihood function for a given set of observations $z_1, z_2, ..., z_m$ and can be obtained by solving the following optimization problem:

$$\text{Maximize} \quad logf_m(z) \tag{2.6}$$

or

$$\text{Minimize} \quad \sum_{i=1}^{m}\left(\frac{z_i-\mu_i}{\sigma_i}\right)^2 \tag{2.7}$$

Equation (2.7) can be expressed by the following optimization problem:

$$\begin{aligned} &\text{Minimize} \quad \sum_{i=1}^{m} W_{ii}r_i^2 \\ &\text{subject to} \quad z_i = h_i(x) + r_i, \quad i = 1, \cdots, m \end{aligned} \tag{2.8}$$

known as Weighted Least Square (WLS) method, where $W$ is a diagonal matrix with diagonal entries of $W_{ii} = \frac{1}{\sigma_i^2}$ and the measurement residuals are defined as: $r_i = z_i - h_i(x)$.

The WLS method is usually formulated as an unconstrained minimization problem for the objective function (2.8), defined as the weighted square sum of the difference

between the measured values $\boldsymbol{z}$ and their estimated values $\boldsymbol{h}(\boldsymbol{x})$:

$$\begin{aligned} J(x) &= [\boldsymbol{z} - \boldsymbol{h}(\boldsymbol{x})]^T \boldsymbol{W} [\boldsymbol{z} - \boldsymbol{h}(\boldsymbol{x})] \\ &= \sum_{i=1}^{m} \frac{[z_i - h_i(x)]^2}{\sigma_i^2} \end{aligned} \tag{2.9}$$

At the solution, the following $n$ first-order optimality conditions must be satisfied,

$$\begin{aligned} g(x) &= \frac{\partial J(\boldsymbol{x})}{\partial \boldsymbol{x}} \\ &= -2 \sum_{i=1}^{m} \frac{[z_i - h_i(x)]}{\sigma_i^2} \frac{\partial h_i(x)}{\partial x} \\ &= \boldsymbol{H}^T(\boldsymbol{x}) \boldsymbol{W} [\boldsymbol{z} - \boldsymbol{h}(\boldsymbol{x})] = 0 \end{aligned} \tag{2.10}$$

where $\boldsymbol{H}(\boldsymbol{x}) = \frac{\partial \boldsymbol{h}(\boldsymbol{x})}{\partial \boldsymbol{x}}$ is the $m$ x $n$ Jacobian matrix of vector $\boldsymbol{h}(\boldsymbol{x})$. The goal is to obtain the vector $\hat{\boldsymbol{x}}$ satisfying the nonlinear equation (2.10). Like in the load flow problem, the most effective way to do so lies in the application of the Newton–Raphson (NR) iterative process, that converges quadratically to the solution [2].

Expanding $\boldsymbol{g}(\boldsymbol{x})$ in its Taylor series and neglecting those terms that contain the second-order or higher derivatives of $\boldsymbol{h}(\boldsymbol{x})$, the linearized system of $n$ equations that must be solved at each iteration is

$$\boldsymbol{G}\left(\boldsymbol{x}^k\right) \Delta \boldsymbol{x}^k = \boldsymbol{H}^T\left(\boldsymbol{x}^k\right) \boldsymbol{W} \left[\boldsymbol{z} - \boldsymbol{h}\left(\boldsymbol{x}^k\right)\right] \tag{2.11}$$

where $\boldsymbol{G}\left(\boldsymbol{x}^k\right) = \frac{\partial \boldsymbol{g}(\boldsymbol{x})}{\partial \boldsymbol{x}}$, given by (2.12), is known as the gain matrix and $\boldsymbol{x}^k$ denotes the value of $\boldsymbol{x}$ at the k$th$ iteration and

$$\boldsymbol{G}(\boldsymbol{x}^k) = \boldsymbol{H}^T(\boldsymbol{x}^k) \boldsymbol{W} \boldsymbol{H}(\boldsymbol{x}^k) \tag{2.12}$$

If $\boldsymbol{H}$ is of full rank, then the symmetric matrix $\boldsymbol{G}$ is positive definite and the system equation (2.11) has an unique solution. After solving (2.11) for $\Delta \boldsymbol{x}^k$, the state vector is updated before repeating the process:

$$\boldsymbol{x}^{k+1} = \boldsymbol{x}^k + \Delta \boldsymbol{x}^k \tag{2.13}$$

The iterative procedure described above can be summarized as follows:

1. Initialize the state vector $\boldsymbol{x}_0$ with flat start ($V_i = 1, \theta_i = 0$).
2. Compute the measurement residuals $[\boldsymbol{z} - \boldsymbol{h}(\boldsymbol{x})]$.
3. Compute the weight matrix $W_{ii} = \frac{1}{\sigma_i^2}$.
4. Obtain $\boldsymbol{H}$ and $\boldsymbol{G} = \boldsymbol{H}^T \boldsymbol{W} \boldsymbol{H}$.
5. Solve the linearized system of equations (2.11) by Cholesky decomposition.
6. Update the state vector $\boldsymbol{x}^{k+1}$.
7. If any of the elements of $\Delta \boldsymbol{x}$ exceeds a specified convergence threshold then return to step 2. Otherwise, the estimation of the system states has been achieved.

### 2.2.2 Generalized state estimation considering FACTS, WTG and ALFC

State estimation is the statistical process in which the best estimate of the state of the system is obtained at a given point of time based on a set of redundant real-time measurements and a predetermined system model [19]. In the context of this chapter, the power system state $\boldsymbol{x}$ is defined by the estimated values of the nodal voltage angles and magnitudes, the state variables of FACTS controllers and WTGs as well as the frequency deviation from its nominal value: $\hat{\boldsymbol{x}} = \left[\hat{\boldsymbol{\theta}}\ \hat{\boldsymbol{V}}\ \hat{\boldsymbol{x}}_{FACTS}\ \hat{\boldsymbol{x}}_{WTG}\ \hat{\boldsymbol{x}}_{\Delta f}\right]^T$, where the superindex $T$ indicates transposition. Furthermore, the set of physical measurements $\boldsymbol{z}$ collected from the network are provided by a SCADA system and PMUs: $\boldsymbol{z} = [\boldsymbol{z}_{SCADA}\ \boldsymbol{z}_{PMU}]$. The SCADA system is used by the electric power industry to gather and to transmit measurement data to the control centers, where these data are processed for optimizing, supervising and controlling the generation and transmission systems. Substations are typically equipped with remote terminal units which are used to gather different types of measurements from the field and transmit them to the control centers using a SCADA system. These measurements are power flows, power injections and voltage magnitudes measurements, $\boldsymbol{z}_{SCADA} = [\boldsymbol{P}_{branch}\ \boldsymbol{Q}_{branch}\ \boldsymbol{P}_{inj}\ \boldsymbol{Q}_{inj}\ \boldsymbol{V}]^t$, while PMUs provide a set of synchronized phasor measurements associated with nodal voltages and current flows, $\boldsymbol{z}_{PMU} = [\boldsymbol{\theta}_{PMU}\ \boldsymbol{V}_{PMU}\ \boldsymbol{I}_{branch,r}\ \boldsymbol{I}_{branch,i}]^t$ . In our proposal the current measurements are represented in the rectangular system of coordinates to avoid the convergence problems reported in [19,20]. The uncertainty propagation theory must be applied, however, to compute the variances of

this new set of measurements in terms of variance on the magnitude and phase angle of currents [15,20,21].

In general, the measured values are mathematically represented by $\boldsymbol{z} = \boldsymbol{h}(\hat{\boldsymbol{x}}) + \epsilon$ [2], where $\boldsymbol{h}(\hat{\boldsymbol{x}})$ is a vector of nonlinear functions, referred to as estimated measurements, relating $\boldsymbol{z}$ and $\hat{\boldsymbol{x}}$ through the mathematical model of the system, and $\boldsymbol{\epsilon}$ is the vector of uncorrelated measurement residuals with mean value $E[\epsilon] = 0$. Based on this representation, the WLS method is employed to estimate the state variable values that best fit the available set of measurements by minimizing the weighted sum of the squares of the measurement residuals, which are given by the differences between the estimated and physical measurement values:

$$\boldsymbol{J}(\hat{\boldsymbol{x}}) = [\boldsymbol{z} - \boldsymbol{h}(\hat{\boldsymbol{x}})]^T \boldsymbol{R}^{-1} [\boldsymbol{z} - \boldsymbol{h}(\hat{\boldsymbol{x}})] \tag{2.14}$$

where $\boldsymbol{R} = diag\{\sigma_{ii}^2\}$ is the error covariance matrix, and $\sigma_{ii} = \sigma_i$ is the standard deviation of the $i$th measurement.

The minimization of $\boldsymbol{J}(\hat{\boldsymbol{x}})$ with respect to $\hat{\boldsymbol{x}}$ results in a set of nonlinear equations,

$$\boldsymbol{H}(\hat{\boldsymbol{x}})^T \boldsymbol{R}^{-1} [\boldsymbol{z} - \boldsymbol{h}(\hat{\boldsymbol{x}})] \tag{2.15}$$

where $\boldsymbol{H}(\hat{\boldsymbol{x}}) = \partial \boldsymbol{h}(\hat{\boldsymbol{x}}) / \partial \hat{\boldsymbol{x}}$ is the Jacobian matrix of the estimated measurements given by (2.16):

$$\boldsymbol{H}(\hat{\boldsymbol{x}}) = \begin{bmatrix} \boldsymbol{H}^{SCADA} \\ \boldsymbol{H}_{\vec{V}}^{PMU} \\ \boldsymbol{H}_{\vec{I}}^{PMU} \end{bmatrix} = \begin{bmatrix} \frac{\partial \hat{\boldsymbol{P}}_{inj}}{\partial \hat{\boldsymbol{\theta}}} & \frac{\partial \hat{\boldsymbol{P}}_{inj}}{\partial \hat{\boldsymbol{V}}} & \frac{\partial \hat{\boldsymbol{P}}_{inj}}{\partial \hat{\boldsymbol{x}}_{FACTS}} & \frac{\partial \hat{\boldsymbol{P}}_{inj}}{\partial \hat{\boldsymbol{x}}_{WTG}} & \frac{\partial \hat{\boldsymbol{P}}_{inj}}{\partial \hat{\boldsymbol{x}}_{\Delta f}} \\ \frac{\partial \hat{\boldsymbol{Q}}_{inj}}{\partial \hat{\boldsymbol{\theta}}} & \frac{\partial \hat{\boldsymbol{Q}}_{inj}}{\partial \hat{\boldsymbol{V}}} & \frac{\partial \hat{\boldsymbol{Q}}_{inj}}{\partial \hat{\boldsymbol{x}}_{FACTS}} & \frac{\partial \hat{\boldsymbol{Q}}_{inj}}{\partial \hat{\boldsymbol{x}}_{WTG}} & \frac{\partial \hat{\boldsymbol{Q}}_{inj}}{\partial \hat{\boldsymbol{x}}_{\Delta f}} \\ \frac{\partial \hat{\boldsymbol{P}}_{branch}}{\partial \hat{\boldsymbol{\theta}}} & \frac{\partial \hat{\boldsymbol{P}}_{branch}}{\partial \hat{\boldsymbol{V}}} & \frac{\partial \hat{\boldsymbol{P}}_{branch}}{\partial \hat{\boldsymbol{x}}_{FACTS}} & \frac{\partial \hat{\boldsymbol{P}}_{branch}}{\partial \hat{\boldsymbol{x}}_{WTG}} & \frac{\partial \hat{\boldsymbol{P}}_{branch}}{\partial \hat{\boldsymbol{x}}_{\Delta f}} \\ \frac{\partial \hat{\boldsymbol{Q}}_{branch}}{\partial \hat{\boldsymbol{\theta}}} & \frac{\partial \hat{\boldsymbol{Q}}_{branch}}{\partial \hat{\boldsymbol{V}}} & \frac{\partial \hat{\boldsymbol{Q}}_{branch}}{\partial \hat{\boldsymbol{x}}_{FACTS}} & \frac{\partial \hat{\boldsymbol{Q}}_{branch}}{\partial \hat{\boldsymbol{x}}_{WTG}} & \frac{\partial \hat{\boldsymbol{Q}}_{branch}}{\partial \hat{\boldsymbol{x}}_{\Delta f}} \\ 0 & I & 0 & 0 & 0 \\ I & 0 & 0 & 0 & 0 \\ 0 & I & 0 & 0 & 0 \\ \frac{\partial \boldsymbol{I}_{branch,r}}{\partial \hat{\boldsymbol{\theta}}} & \frac{\partial \boldsymbol{I}_{branch,r}}{\partial \hat{\boldsymbol{V}}} & \frac{\partial \boldsymbol{I}_{branch,r}}{\partial \hat{\boldsymbol{x}}_{FACTS}} & \frac{\partial \boldsymbol{I}_{branch,r}}{\partial \hat{\boldsymbol{x}}_{WTG}} & \frac{\partial \boldsymbol{I}_{branch,r}}{\partial \hat{\boldsymbol{x}}_{\Delta f}} \\ \frac{\partial \boldsymbol{I}_{branch,i}}{\partial \hat{\boldsymbol{\theta}}} & \frac{\partial \boldsymbol{I}_{branch,i}}{\partial \hat{\boldsymbol{V}}} & \frac{\partial \boldsymbol{I}_{branch,i}}{\partial \hat{\boldsymbol{x}}_{FACTS}} & \frac{\partial \boldsymbol{I}_{branch,i}}{\partial \hat{\boldsymbol{x}}_{WTG}} & \frac{\partial \boldsymbol{I}_{branch,i}}{\partial \hat{\boldsymbol{x}}_{\Delta f}} \end{bmatrix} \tag{2.16}$$

while the covariance matrix is expressed as:

$$\boldsymbol{R} = diag\left[\boldsymbol{R}^{SCADA} \ \boldsymbol{R}_{\vec{V}}^{PMU} \ \boldsymbol{R}_{\vec{I}}^{PMU}\right]^T \tag{2.17}$$

with

$$\left[\boldsymbol{R}^{SCADA}\right] = diag\left\{\boldsymbol{\sigma}^2_{Pinj}\ \boldsymbol{\sigma}^2_{Qinj}\ \boldsymbol{\sigma}^2_{Pbranch}\ \boldsymbol{\sigma}^2_{Qbranch}\ \boldsymbol{\sigma}^2_{V}\right\} \tag{2.18}$$

$$\left[\boldsymbol{R}^{PMU}_{\vec{V}}\right] = diag\left\{\boldsymbol{\sigma}^2_{\theta_{PMU}}\ \boldsymbol{\sigma}^2_{V_{PMU}}\right\} \tag{2.19}$$

$$\left[\boldsymbol{R}^{PMU}_{\vec{I}}\right] = diag\left\{\boldsymbol{\sigma}^2_{I_{branch,r}}\ \boldsymbol{\sigma}^2_{I_{branch,i}}\right\}. \tag{2.20}$$

Note that depending on the location of the SCADA devices and PMUs, some of the Jacobian elements associated with the estimated measurements of power injections, power flows and/or current flows will be zero because there could not exist a relation between these measurements with some of the state variables to be estimated.

In order to perform the state estimation, (2.15) is linearized using the first-order approximation of the Taylor's series, and the Hessian term is neglected in the resulting approximation to obtain

$$\boldsymbol{G}\left(\hat{\boldsymbol{x}}\right)\Delta\hat{\boldsymbol{x}} \approx \boldsymbol{H}\left(\hat{\boldsymbol{x}}\right)^T \boldsymbol{R}^{-1}\left[\boldsymbol{z} - \boldsymbol{h}\left(\hat{\boldsymbol{x}}\right)\right] \tag{2.21}$$

where $\boldsymbol{G}\left(\hat{\boldsymbol{x}}\right)$ is the gain matrix $\boldsymbol{H}\left(\hat{\boldsymbol{x}}\right)^T \boldsymbol{R}^{-1}\boldsymbol{H}\left(\hat{\boldsymbol{x}}\right)$.

These linearized equations are iteratively solved for the vector of estimated adjustments $\Delta\hat{\boldsymbol{x}}^k$, by considering initial values $\hat{\boldsymbol{x}}^k_0$ , to obtain new estimated values of state variables $\hat{\boldsymbol{x}}^{k+1} = \hat{\boldsymbol{x}}^k_0 + \Delta\hat{\boldsymbol{x}}^k$, where $k$ is the iteration number. This iterative process is repeated for new initial conditions $\hat{\boldsymbol{x}}^{k+1}_0 = \hat{\boldsymbol{x}}^{k+1}$ until an acceptable tolerance $Max\left|\Delta\hat{\boldsymbol{x}}^k\right| < Tol$ is achieved or the maximum number of iterations has been exceeded.

Similarly to the estimation of network state variables, the nonlinear functions $\boldsymbol{h}\left(\cdot\right)$ used to determine the state variables of WTGs and ALFCs are directly derived from the measurements provided by the SCADA system and PMUs at the nodes at which these electric components are connected. The nonlinear functions and also the contribution to Jacobian matrix of each device modeled in proposed approach is presented in Appendix B. Based on Figure 2.1, the set of estimated measurements are as follows.

The conventional formulation of the SE problem assumes that the system frequency is constant, with voltage and frequency characteristics of loads and generators neglected, so the physical measurement of active (reactive) power injected at the $k$th system's node is only represented in terms of the estimated active

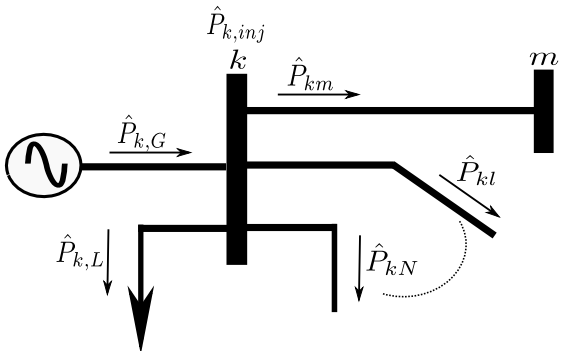


FIGURE 2.1: Bus with voltage and frequency dependent loads, WTGs, and ALFC

(reactive) power flows through all transmission elements embedded at this node: $P_{k,inj} = \sum_{\substack{i=1 \\ i \neq k}}^{N} \hat{\boldsymbol{P}}_{ki}$ ($Q_{k,inj} = \sum_{\substack{i=1 \\ i \neq k}}^{N} \hat{\boldsymbol{Q}}_{ki}$), where $N$ is the number of nodes in the system. On the other hand, when steady state models of several types of wind generators are considered in the SE formulation together with the effects of governor characteristics as well as voltage and frequency dependence of loads, the measurement of active (reactive) power injected at node $k$ must be mathematically expressed from both a grid and a generator side perspective: $P_{k,inj} = \hat{\boldsymbol{P}}_{k,WTG} + \hat{\boldsymbol{P}}_{k,G} + \hat{\boldsymbol{P}}_{k,L} = \sum_{\substack{i=1 \\ i \neq k}}^{N} \hat{\boldsymbol{P}}_{ki}$ ($Q_{k,inj} = \hat{\boldsymbol{Q}}_{k,WTG} + \hat{\boldsymbol{Q}}_{k,G} + \hat{\boldsymbol{Q}}_{k,L} = \sum_{\substack{i=1 \\ i \neq k}}^{N} \hat{\boldsymbol{Q}}_{ki}$).

From the mismatch active power flow equation, the following two estimated measurement equations are formulated and included in the proposed SE approach to represent the measurement of an injected active power at node $k$

$$\boldsymbol{h}\left(\hat{\boldsymbol{x}}_{WTG}, \hat{\boldsymbol{x}}_{\Delta f}\right) = \hat{\boldsymbol{P}}_{k,WTG}\left(\hat{\boldsymbol{x}}_{WTG}\right) + \hat{\boldsymbol{P}}_{k,G}\left(\boldsymbol{\Delta}\hat{\boldsymbol{f}}, \hat{\boldsymbol{V}}_k\right) - \hat{\boldsymbol{P}}_{k,L}\left(\boldsymbol{\Delta}\hat{\boldsymbol{f}}, \hat{\boldsymbol{V}}_k\right), \quad (2.22)$$

$$\boldsymbol{h}\left(\hat{\boldsymbol{\theta}}, \hat{\boldsymbol{V}}\right) = \sum_{i=1}^{N} \hat{\boldsymbol{P}}_{ki,cal}\left(\hat{\boldsymbol{\theta}}, \hat{\boldsymbol{V}}\right), \quad (2.23)$$

where $\boldsymbol{h}\left(\hat{\boldsymbol{x}}_{WTG}, \hat{\boldsymbol{x}}_{\Delta f}\right)$ relates the physical measurement to the WTG and ALFC (network) state variables. Note that some terms on the right-hand side of (2.22) can be zero if the electric components represented by these terms are not connected to this node. A similar formulation is carried out for a measurement related to an injected reactive power.

A PMU can provide a phasor measurement of the branch current of a WTG, a generator participating in the frequency regulation, and/or a voltage and frequency dependent load embedded at the kth node. Accordingly, the current equations at the terminals of one of these electric components are used for relating the measurement to the state variables, as given by (2.24), (2.25), and (2.26) for

WTGs, generators participating in the frequency regulation as well as voltage and frequency dependent loads, respectively. In addition to this set of equations, the current phasor measurement is also represented as a function of the network state variables by (2.27), which is included in the proposed SE approach together with (2.24)-(2.26)

$$\begin{aligned} \boldsymbol{h}_{I_{WTG,r}}\left(\hat{\boldsymbol{x}}_{WTG}\right) &= real\left\{\bar{\boldsymbol{I}}_{k,WTG}\left(\hat{\boldsymbol{x}}_{WTG}\right)\right\} \\ \boldsymbol{h}_{I_{WTG,i}}\left(\hat{\boldsymbol{x}}_{WTG}\right) &= imag\left\{\bar{\boldsymbol{I}}_{k,WTG}\left(\hat{\boldsymbol{x}}_{WTG}\right)\right\}, \end{aligned} \tag{2.24}$$

$$\begin{aligned} \boldsymbol{h}_{I_{G,r}}\left(\hat{\boldsymbol{x}}_{\Delta f}\right) &= real\left\{\bar{\boldsymbol{I}}_{k,G}\left(\hat{\boldsymbol{x}}_{\Delta f}\right)\right\} \\ \boldsymbol{h}_{I_{G,i}}\left(\hat{\boldsymbol{x}}_{\Delta f}\right) &= imag\left\{\bar{\boldsymbol{I}}_{k,G}\left(\hat{\boldsymbol{x}}_{\Delta f}\right)\right\}, \end{aligned} \tag{2.25}$$

$$\begin{aligned} \boldsymbol{h}_{I_{L,r}}\left(\hat{\boldsymbol{x}}_{\Delta f}\right) &= real\left\{\bar{\boldsymbol{I}}_{k,L}\left(\hat{\boldsymbol{x}}_{\Delta f}\right)\right\} \\ \boldsymbol{h}_{I_{L,i}}\left(\hat{\boldsymbol{x}}_{\Delta f}\right) &= imgag\left\{\bar{\boldsymbol{I}}_{k,L}\left(\hat{\boldsymbol{x}}_{\Delta f}\right)\right\}, \end{aligned} \tag{2.26}$$

$$\begin{aligned} \boldsymbol{h}_{I_{branch,r}}\left(\hat{\boldsymbol{\theta}}, \hat{\boldsymbol{V}}\right) &= real\left\{\sum_{i=1, i\neq k}^{N} \bar{\boldsymbol{I}}_{ki,cal}\left(\hat{\boldsymbol{\theta}}, \hat{\boldsymbol{V}}\right)\right\} \\ \boldsymbol{h}_{I_{branch,i}}\left(\hat{\boldsymbol{\theta}}, \hat{\boldsymbol{V}}\right) &= imag\left\{\sum_{i=1, i\neq k}^{N} \bar{\boldsymbol{I}}_{ki,cal}\left(\hat{\boldsymbol{\theta}}, \hat{\boldsymbol{V}}\right)\right\}. \end{aligned} \tag{2.27}$$

## 2.3 Multi-Area State Estimation (MASE)

The proposed SE algorithm has been implemented following the centralized and decentralized MASE approaches. In the former approach, all measurements are simultaneously processed for solving the large-scale SE problem. The decentralized MASE is based on a decomposition and aggregation procedure [45, 46, 68]. For the purpose of our implementation, the entire power system is decomposed into a certain number of overlapping control areas based on a geographical basis. In this decomposition, the system buses are categorized as follows [17]: (i) an internal bus with all its neighboring buses within the subarea to which this bus belongs; (ii) an internal boundary bus with some of its neighboring buses in the same subarea to which this bus belongs, while the rest of its neighbors are external boundary buses; and (iii) an external boundary bus, which is an internal boundary bus of another subarea. Based on the above, a tie-line overlapping or an extended overlapping is used according to the type of transmission element employed for connecting the control areas, as shown in Figure 2.2. The former is used for transmission lines and transformers, while the latter is used for FACTS controllers in order to avoid convergence problems.

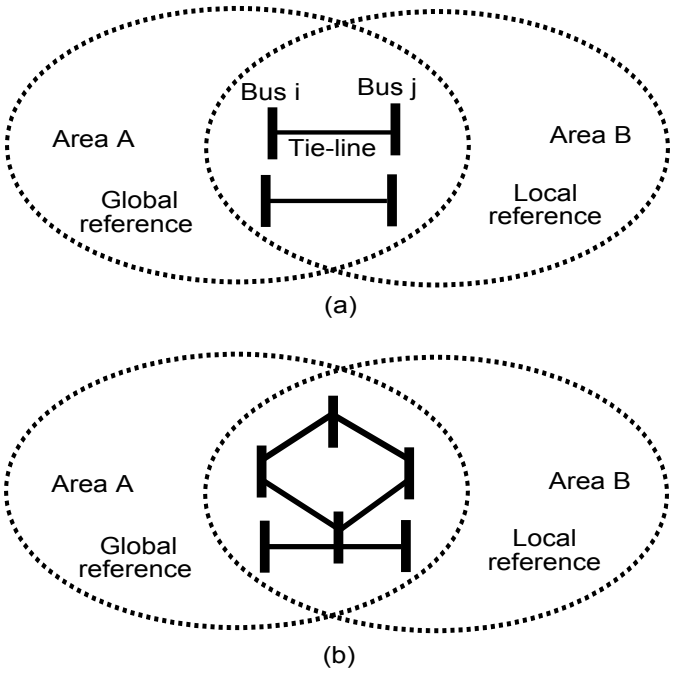


FIGURE 2.2: (a) Tie-line overlapping control areas and (b) extended overlapping control areas.

Once the decomposition has been carried out, an independent local estimation is performed on each overlapped subarea using the proposed WLS-based SE algorithm considering the measurements received from its own local substations and its own reference bus. In this case, each subarea is responsible for detecting and eliminating bad data. In those control areas where no PMUs are installed, one internal bus is chosen as the reference bus with respect to which all other voltage phase angles are estimated. When PMUs are installed, however, the estimation is performed considering no reference bus, and all estimated voltage phase angles are referred to the time reference provided by the global positioning system (GPS).

In the aggregation stage, a single coordinate estimation is generated for the entire power system by gathering all the local state estimations. Since this global estimation must be established with all voltage phase angles referred to the same reference, the local reference of one subarea is selected as a global reference angle, and all estimated phase angles in the rest of the control areas refer to this global reference. The transformation between two frames of reference is determined by computing a common reference shift angle [46] based on the estimated values of voltage phase angles at internal and external boundary buses. Note that each of the boundary buses that are common to two overlapped control areas will have two estimated values of the phase angle, each of them associated with the corresponding local estimation. In addition, these values can be different for the same

bus depending on the phase angle reference chosen at each overlapped subarea. Considering that the phase angles of one of these two control areas are estimated with respect to the global reference, which in our proposal is the reference dictated by the GPS system, the common reference shift angle is defined as the average of the differences between the two estimated values of phase angle for each boundary bus:

$$\phi_{ref}^{G-L} = \frac{sum_{i=1}^{N_{CBB}} \left(\theta_i^G - \theta_i^L\right)}{N_{CBB}} \tag{2.28}$$

where $N_{CBB}$ is the number of common boundary buses, while the superscripts G and L indicate that the phase angle value has been estimated with respect to the global and local reference buses, respectively. This shift angle $\phi_{ref}^{G-L}$ must be added to all phase angles estimated with respect to a local reference to produce a coherent state for both control areas. This procedure is used to upgrade all phase angles of other control areas to the same reference frame, even for those control areas with PMUs in order to avoid the condition of PMU data loss or the PMU measurement offset issue caused by different vendors. If these two problems do not exist, then the common reference shift angle should be nearly zero.

## 2.4 Practical implementation of the proposed algorithm

Apart from the mathematical formulation described above, the following issues were considered in the practical implementation of the proposed algorithm.

### 2.4.1 Reference for the voltage phase angle states

The voltage angles must be estimated with respect to a global reference angle, which is nothing more than setting a time reference in order to avoid an inconsistency between possible different references adopted to estimate voltage angles in buses with and without PMUs and to establish a single angle profile throughout the network. Based on this observation, the global reference can be selected with respect to the time reference provided by the global positioning system (GPS) to which all phase angle measurements are synchronized [21] or with respect to a phase angle of a selected bus [69]. When the time signal from the GPS is selected as a reference without using a reference bus, all voltage angles are considered in

the state vector [21]. Similarly, an artificial phase angle measurement at a selected bus can be adopted as a reference and all voltage angle measurements are synchronized with respect to this common angle reference. In this case, the reference angle is also included in the set of states [21].

### 2.4.2 Initialization process

Initial conditions for the system states must be provided for the iterative minimization problem. A flat start is used to initialize the nodal voltage states: voltage magnitude equal to 1 pu and all bus angles equal to zero. On the other hand, the FACTS state variables and WTG are initialized as reported in Section 4.2 of [15] and Section 3 of [37], respectively.

### 2.4.3 Bad data identification

A common assumption is that the inaccuracy in a given datum can be represented by a normal distribution with known mean and covariance, such that erroneous measurements can be processed by means of statistical tests in such a way that the resulting estimation is very close ($10^{-6}$) to the true value of the state. The presence of bad data is detected based on the chi-square distribution test $\chi^2_{(m-n),\alpha}$, with $(m-n)$ degrees of freedom and a significance value $\alpha$ of the test [70]. If the $\chi^2_{(m-n),\alpha}$ test is positive, the largest normalized residual test is performed to identify and eliminate any bad data in the set of measurements [70].

## 2.5 Study cases

The SE performance is reported in this section using the following two study cases: the former called *Case A*, analyze the implementation of a state estimation of flexible AC transmission system considering phasor measurements and the latter called *Case B* analyze a generalized state estimation of flexible transmission system considering wind generator and primary frequency control, both cases use a modified IEEE-118 bus test system.

The random errors added to traditional measurements are considered with mean zero and standard deviation values of $\sigma_{inj} = 0.01$, $\sigma_{flow} = 0.008$ and $\sigma_{volt} = 0.004$, for nodal power injections, power flows through transmission elements and voltage

TABLE 2.1: FACTS controllers' control targets in the IEEE-118 system

| FACTS controller | Controlled variable | Original value | Target value |
|---|---|---|---|
| TCSC | $P_{30-38}$ | 62.5329 MW | 80.0 MW |
| UPFC | $P_{81-68}$ | 44.3602 MW | 70.0 MW |
| UPFC | $Q_{81-68}$ | −75.5453 MVAR | 10.0 MVAR |
| UPFC | $V_{81}$ | 0.9968 pu | 1.05 pu |
| SVC | $V_{48}$ | 1.0206 pu | 1.02 pu |

magnitudes, respectively [54]. In the case of PMU measurements, the standard deviations of the errors for both voltage and current phasors are set at 0.0017 rad for phase angles and 0.002 pu for magnitudes [13]. Lastly, a numerical convergence criterion of $Tol = 1\text{x}10^{-6}$ has been considered in all study cases.

### 2.5.1 Case A

The IEEE 118-bus system, shown in Fig. 2.3, has been modified to include one SVC connected at bus 48, one TCSC and one UPFC, which are coupled in series with the transmission lines connected at buses 30−38 and 81−68, respectively. The SVC step-down transformer impedance is $X_T = j0.037$ pu and the capacitive and inductive reactance are $X_C = 9.365\text{x}10^{-3}$ pu and $X_L = 1.60\text{x}10^{-3}$ pu, respectively, at a base frequency. The TCSC reactance parameters at fundamental frequency are regarded as $X_C = 9.375\text{x}10^{-3}$ pu and $X_L = 1.625\text{x}10^{-3}$ pu. On the other hand, the UPFC's coupling transformers have the same impedances: $Z_{vR} = Z_{cR} = 0.05 + j0.1$ pu. The set of input measurements provided to the SE is obtained from a power flow program including FACTS devices [71]. The FACTS controllers were embedded to perform the control of power flow and voltage magnitude at specified target values reported in Table 2.1. The original values of the variables to be controlled before the FACTS devices were embedded in the network are also reported in this table. Note that the UPFC was used to decrease and divert the direction of the reactive power flow in branch 81-68. The initial conditions of the SVC and TCSC firing angles are $SVC = 139°$ and $TCSC = 145°$, respectively, while the initial conditions of the voltage sources representing the UPFC's shunt and series converters are $\bar{V}_{cR} = 0.0707\angle 81.86°$ and $\bar{V}_{vR} = 1.0\angle 0.0°$, respectively.

The set of traditional measurements provided by the SCADA system is composed of 376 pairs of power flow measurements, where 372 are associated with transmission lines and transformers and four are related to the TCSC and UPFC controllers, respectively. In addition, one pseudomeasurement is also included to take into account the active power balance constraint at the DC link of the UPFC. Lastly, one measurement of reactive power flow through the SVC is also considered.

TABLE 2.2: Estimated FACTS state variables in the IEEE-118 system.

| FACTS controller | State variables | Estimated states | Calculated states |
|---|---|---|---|
| TCSC | $\alpha_{TCSC}$ | 144.737° | 144.737° |
| UPFC | $V_{vR}\angle\theta_{vR}$ | $1.29007\angle 17.2211°$ | $1.29007\angle 17.221°$ |
| | $V_{cR}\angle\theta_{cR}$ | $-0.153452\angle 113.12°$ | $-0.153452\angle 113.12°$ |
| SVC | $\alpha_{SVC}$ | 136.001° | 135.991° |

TABLE 2.3: UPFC converters powers in the IEEE-118 system.

| Source | Active power (pu) | Reactive power (pu) |
|---|---|---|
| Shunt | 0.00453812 | 3.18834 |
| Series | -0.00453812 | 0.106574 |

On the other hand, PMUs are installed at bus 69, which is considered a reference bus, and at those buses where the FACTS controllers are connected: buses 30 and $ftcsc$ for the TCSC controller and buses 81 and $fupfc$ for the UPFC. In this case, PMUs provide both nodal voltage and branch current phasor measurements for a total of five measurements of voltage phasors and 28 measurements of phasors of branch currents through transmission lines, transformers and FACTS controllers. The phase angle measurement of the reference bus is not considered in the SE algorithm. Lastly, the SCADA system and PMU devices provide a total number of 820 measurements, which are employed to estimate 239 nodal voltage states, the SVC's firing angle value $\alpha_{SVC}$, the TCSC's firing angle value $\alpha_{TCSC}$ and the UPFC's voltage phasors $V_{vR}\angle\theta_{vR}$ and $V_{cR}\angle\theta_{cR}$. The relation between the number of available measurements and state variables to be estimated yields a degree of freedom of $k = 575$ and a test threshold of $\chi^2_{k,\alpha} \approx \frac{1}{2}\left(2.326 + \sqrt{2k-1}\right) = 656.05$, with confidence level of 99% [72].

Based on the information mentioned above, the state estimation is achieved in seven iterations with an optimality function's value of $J(x) = 8.0533\text{x}10^{-4}$. Table 2.2 shows a comparison between the calculated (load flows) [71] and the estimated FACTS state variables: one observes that approximately the same results were achieved.

Furthermore, the estimated values of the active and reactive powers at the UPFC series and shunt converters are reported in Table 2.3, which clearly shows that the UPFC's DC-link active power constraint has been fulfilled. In order to assess the impact of the number of synchronized measurements on the accuracy of the state estimation, four case studies have been analyzed where one estimation is carried out based only on measurements provided by a SCADA system, whereas the other estimations consider one, three and five PMUs, respectively. The SCADA measurements were contaminated by adding random noise, and the resulting measurements were used in all cases.

### 2.5.2 Case B

The decentralized MASE has been developed as discussed above and is applied to estimate the operating point of a power system containing WTGs, ALFCs and FACTS controllers. For this purpose, the IEEE 118-bus test system whose data are reported in [73] was used for this study. This system represents a portion of the American Electric Power System (in the Midwestern US) as of December 1962 and has been employed as a benchmark system to illustrate proposals associated with steady state analysis of power systems. This system has been decomposed into nine observable subareas, as shown in Fig. 2.3 [74], which are capable of regulating their corresponding generation, in response to a system frequency deviation, for contributing to the frequency regulation of the whole system and maintaining the balance between generation and consumption of electric power. Since the indication of overlapping in Fig. 2.3 could be unclear, Table 2.4 details how the overlapping between areas has been defined in the system under analysis. The system has also been modified to include five FACTS controllers, five WTGs, nine generators participating in the frequency regulation, one per area, and three loads whose power demand depends on the voltage magnitude and frequency values. In this case, FACTS controllers were embedded to perform the control of power flow and voltage magnitude at specified target values. Hence, the estimator is used to estimate the values of the FACTS controllers' state variables at which their corresponding control targets are achieved. The parameters and control settings of FACTS controllers are reported in Tables 2.5 and 2.6, respectively, where the acronyms SVC, TCSC, UPFC, LTC and PS stand for the static VARs compensator, thyristor-controlled series compensator, unified power flow controller, load tap changer and phase shifter transformers, respectively. Note that original values of the power flows and voltage magnitudes to be controlled before the FACTS devices were embedded in the network are also reported in Table 2.6. Furthermore, the phase shifter transformer was used to increase and divert the direction of the active power flow in branch 70-121. Detailed models of these controllers for SE are given in [43]. Note that additional nodes have been included in the network in order to connect the FACTS controllers TCSC, UPFC, LTC and PS in series with transmission elements connected between nodes 30-120, 119-81, 21-122 and 70-121, respectively, as indicated in Fig. 2.3. The parameters of WTGs are also reported in Table 2.5, while data related to regulated generators and dependent loads are given in Table 2.7.

The set of measurements used by the MASE are generated from a power flow (PF)

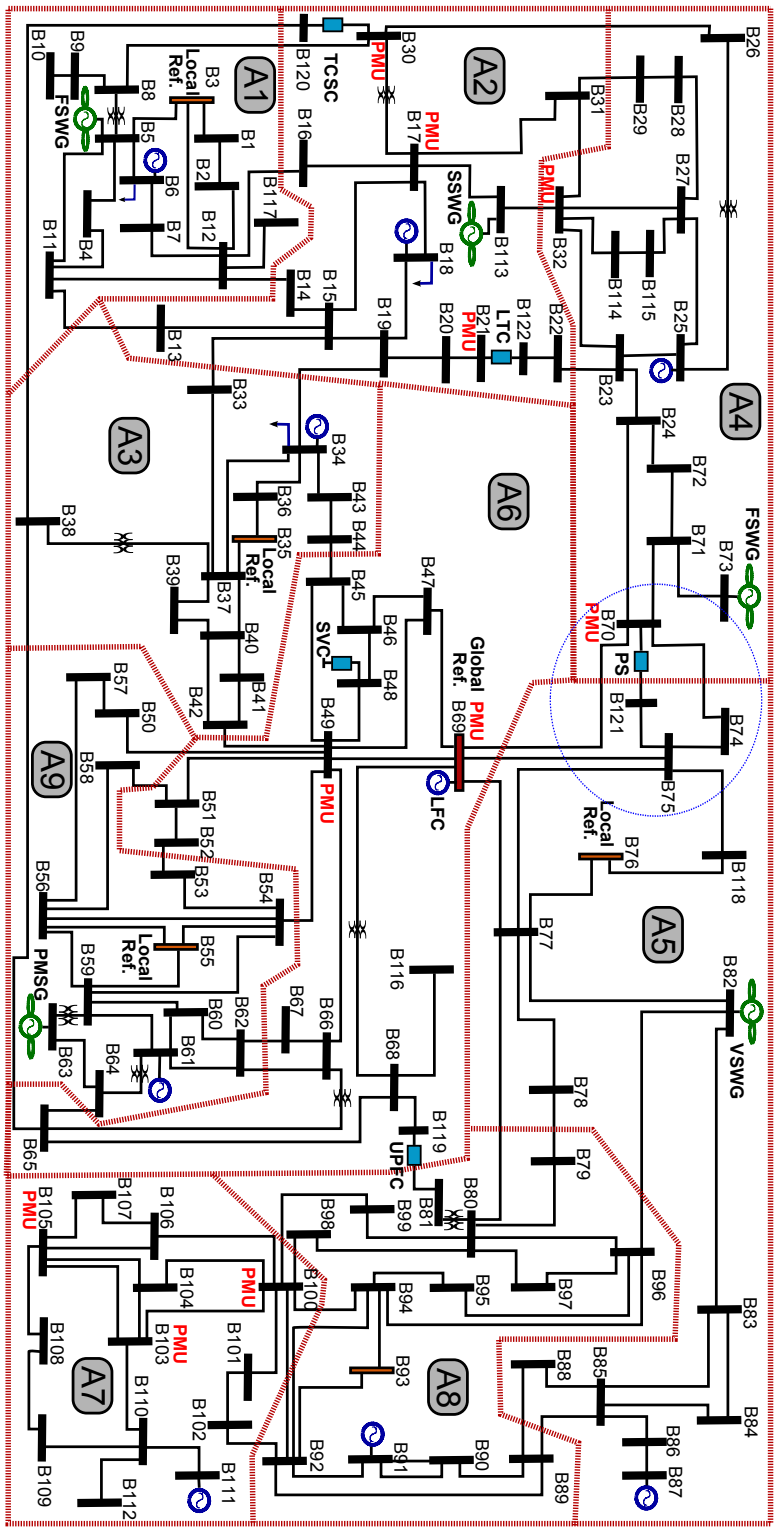


FIGURE 2.3: One-line diagram of modified IEEE-118 test system

TABLE 2.4: Overlapping between control areas.

| Area from | Area to | Tie-line overlapping | Extended overlapping |
|---|---|---|---|
| A1 | A2 | B8-B30, B12-B16, B12-B14, B11-B13 | |
| A2 | A3 | B15-B33, B19-B34, B120,B38 | |
| A2 | A4 | B31-B29, B31-B32, B113-B32, B22-B23 | B23-B32 |
| A3 | A6 | B44-B45, B42-B49, B38-B65 | |
| A4 | A5 | B70-B121, B70-B74 | B74-B75, B75-B121 |
| A4 | A6 | B70-B69 | |
| A5 | A6 | B75-B69, B77-B69 | |
| A5 | A8 | B77-B80, B78-B79, B82-B96, B85-B89, B88-B89 | |
| A6 | A8 | B119-B81 | B81-B80, B77-B80, B69-B80 |
| A6 | A9 | B49-B50, B51-B58, B52-B53, B49-B54, B67-B62, B66-B62, B65-B63 | |
| A8 | A7 | B99-B100, B98-B100, B94-B100, B92-B102 | |

TABLE 2.5: Devices included in the extended IEEE 118-bus test system

| Device | Parameters | Initial conditions |
|---|---|---|
| SVC | $X_C = 9.365e^{-3}$ $X_L = 1.60\text{x}10^{-3}$ | $\alpha_{SVC} = 140°$ |
| TCSC | $X_C = 9.375e^{-3}$ $X_L = 1.625\text{x}10^{-3}$ | $\alpha_{TCSC} = 145°$ |
| UPFC | $Z_{vR} = Z_{cR} = 0.05 + j0.1$ | $V_{cR} = 0.1\angle 81.86°$ $V_{vR} = 1.0\angle 0.0°$ |
| LTC | $R_p = R_s = 0$, $X_p = X_s = 0.1$, $G_{so} = B_{so} = 0$ | $T_v = U_v = 1$, $\phi_{Tv} = \phi_{Uv} = 0$ |
| PS | $R_p = R_s = 0$, $X_p = X_s = 0.05$,$G_{so} = B_{so} = 0$ | $T_v = U_v = 1$, $\phi_{Tv} = \phi_{Uv} = 0$ |
| FSWG1 | $R_1 = 0.0027$, $X_1 = 0.025$, $R_2 = 0.0022$, $X_2 = 0.046$, $X_m = 1.38$, $k_V = 0.69$ | $s_0 = -0.005$ |
| FSWG2 | $R_1 = 0$, $X_1 = 0.09985$, $R_2 = 0.00373$, $X_2 = 0.10906$, $X_m = 3.54708$, $k_V = 0.69$ | $s_0 = -0.005799$ |
| SSWG | $R_1 = 0.002699$, $X_1 = 0.072605$, $R_2 = 0.002199$, $X_2 = 0.045999$, $X_m = 1.3799$, $k_V = 0.69$, $V_w = 12$ | $R_x = -100.6981$ |
| VSWG | Appendix B [11] | Section III. D [11] |
| PMSG | $R_{st} = 0.0$, $X_{st} = 0.1$, $V_w = 12$ | $V_gsc = 1$, $\theta_{gsc} = 0°$ |

TABLE 2.6: Control targets of FACTS controllers

| FACTS | Controlled variable | Original value | Target value |
|---|---|---|---|
| SVC | $V_{48}$ | 1.02063 p.u. | 1.02 p.u. |
| TCSC | $P_{30-120}$ | 62.5329 MW | 80 MW |
| UPFC | $V_{81}$ | 0.996808 p.u. | 1.05 p.u. |
| | $P_{119-81}$ | -44.3034 MW | -70 MW |
| | $Q_{119-81}$ | -4.6052 MVAR | -10 MVAR |
| LTC | $V_{21}$ | 0.958623 p.u. | 0.955 p.u. |
| PS | $P_{70-121}$ | -0.14066 MW | 15 MW |

analysis of the modified IEEE 118-bus test system. In this case, the PF program permits the modeling of FACTS controllers, ALFC devices, and dependent loads, where only one reference node must be chosen to set the voltage angle profile in the solution [75]. After this study, a total set of 968 measurements is generated to perform the MASE study, where 146 synchronized phasor measurements are provided by 12 PMUs placed at control areas 2, 4, 6, and 7. The rest of the

TABLE 2.7: Regulated generators and load parameters.

| Area | Bus | Regulated generators and loads parameters | Settings of voltage and complex power |
|---|---|---|---|
| 1 | B6 | *Gen*: $R_k = 0.04$, $a_{Qk} = 1$, $b_{Qk} = 1$<br>*Load*: $R_k = 0.04$, $a_{Qk} = 1$, $b_{Qk} = 1$<br>$K_{pk} = 0.04$, $p_{pk} = 0.2$, $p_{ck} = 0.3$, $p_{zk} = 0.5$,<br>$K_{qk} = 0$, $q_{pk} = 0.2$, $q_{ck} = 0.3$, $q_{zk} = 0.5$,<br>$N1 = N2 = 1$ | $V_k = 0.99$<br>$S_{Gset} = 0 + j15.9260$<br>$S_{Lset} = 52 + j22$ |
| 2 | B18 | | $V_k = 0.973$<br>$S_{Gset} = 0 + j19.5028$<br>$S_{Lset} = 60 + j34$ |
| 3 | B34 | | $V_k = 0.984$<br>$S_{Gset} = 0 + j8$<br>$S_{Lset} = 59 + j26$ |
| 4 | B25 | *Gen*: $R_k = 0.04$, $a_{Qk} = 1$, $b_{Qk} = 1$ | $V_k = 1.05$<br>$S_{Gset} = 220 + j57.22$ |
| 5 | B87 | | $V_k = 1.015$<br>$S_{Gset} = 4 + j11.0216$ |
| 6 | B69 | | $V_k = 1.035$<br>$S_{Gset} = 548.51 - j101.38$ |
| 7 | B111 | | $V_k = 0.98$<br>$S_{Gset} = 36 - j1.8438$ |
| 8 | B91 | | $V_k = 0.98$<br>$S_{Gset} = -10 - j14.8017$ |
| 9 | B61 | | $V_k = 0.995$<br>$S_{Gset} = 160 - j40.3871$ |

measurements are three voltage magnitudes, five pairs of power injections, 393 pairs of power flows, one active power injection, 14 reactive power flows, and eight pseudo-measurements. Power flow measurement pairs were assigned in the tie-line linking boundary buses in order to achieve the observability of each overlapped subarea. The standard deviations used to represent the noise in these measurements are $\sigma_V^{SCADA} = 0.004$, $\sigma_{P,Q,Inj}^{SCADA} = 0.01$, $\sigma_{P,Q,flow}^{SCADA} = 0.008$, $\sigma_V^{PMU} = 0.002$, and $\sigma_{\theta_V}^{PMU} = 0.0017$. The standard deviations of the current phasor measurements represented in rectangular coordinates are calculated by (2.29) and (2.30) considering $\sigma_I^{PMU} = 0.002$ and $\sigma_{\theta_I}^{PMU} = 0.00172$ [21]:

$$\sigma_{Ibranch,r} = \sqrt{\left(\sigma_I^{PMU}\cos\theta_I^{PMU}\right)^2 + \left(\sigma_{\theta_I}^{PMU} I^{PMU}\sin\theta_I^{PMU}\right)^2} \tag{2.29}$$

$$\sigma_{Ibranch,i} = \sqrt{\left(\sigma_I^{PMU}\sin\theta_I^{PMU}\right)^2 + \left(\sigma_{\theta_I}^{PMU} I^{PMU}\cos\theta_I^{PMU}\right)^2} \tag{2.30}$$

#### 2.5.2.1 State Estimation without Bad Data

Based on the information mentioned above, the SE study is performed considering no errors in the measurements. Table 2.8 details the results of the local estimations considering tolerance of $1x10^{-6}$ in the estimated adjustments $x_k$. The local reference bus for each subarea is reported in the second column of this Table. Finally, the results reported in the fifth column of Table 2.8 show that the value of $\Delta f$ estimated by each local estimator is practically the same for all control areas, which agrees with the fact that at the steady state the system is operating at one single frequency. Figure 2.4 shows the reference phase angle difference used for adjusting the estimated values of the voltage phase angle to the global reference. In this case, the local reference of the subarea 6 is chosen as a global reference and corresponds to the time reference provided by the GPS. Note that the shift angle is practically zero between those control areas with a local reference angle that dictated the GPS, which is shown in Figure 2.4 and also reported in Table 2.9. Lastly, the adjustment must be applied not only to nodal voltage phase angles but also to those voltage sources representing FACTS devices and WTGs. Therefore, the phase angles of controlled voltage sources representing the UPFC located at subarea 8, the PMSG placed at subarea 9, and the DFIG at subarea 5 must be adjusted to the global reference. In Figure 2.5, a comparison of true (obtained by power flow program) voltage magnitude and phase and those obtained by centralized state estimator and MASE is carried out. The results obtained from the power flow and the state estimator analyses must be the same because a power flow solution is used to generate the set of measurements from which the estimation of the operating point is carried out. Note that this set of measurements would correspond to the measurements provided by the SCADA system and PMUs. Hence, the solution obtained by both approaches, which completely differ in their formulation and methodology of analysis, must correspond to the same operating point, as shown in Figure 2.5. Finally, Table 2.10 presents the estimated state variables of FACTS controllers and WTGs. These estimations are compared with those values obtained by the power flow program used to generate the measurements [75] and with the estimations provided by a centralized SE implemented for this purpose based on the theory reported above; note that the same results were arrived at. Similarly, this validation is also met for the estimated values of the network state variables.

TABLE 2.8: MASE Results

| Area | Ref. Bus | Iterations | $J(\hat{x})$ | $\Delta f$ |
|---|---|---|---|---|
| A1 | 3 | 5 | $2.30228\text{x}10^{-5}$ | 0.110228 |
| A2 | GPS | 6 | $5.12820\text{x}10^{-5}$ | 0.110228 |
| A3 | 35 | 8 | $4.26134\text{x}10^{-5}$ | 0.110225 |
| A4 | GPS | 5 | $9.08771\text{x}10^{-5}$ | 0.110229 |
| A5 | 76 | 6 | $6.27311\text{x}10^{-5}$ | 0.110225 |
| A6 | GPS, GR | 6 | $2.40369\text{x}10^{-5}$ | 0.110231 |
| A7 | GPS | 4 | $3.27661\text{x}10^{-5}$ | 0.110225 |
| A8 | 93 | 5 | $7.74924\text{x}10^{-5}$ | 0.110225 |
| A9 | 55 | 5 | $5.32572\text{x}10^{-5}$ | 0.110229 |

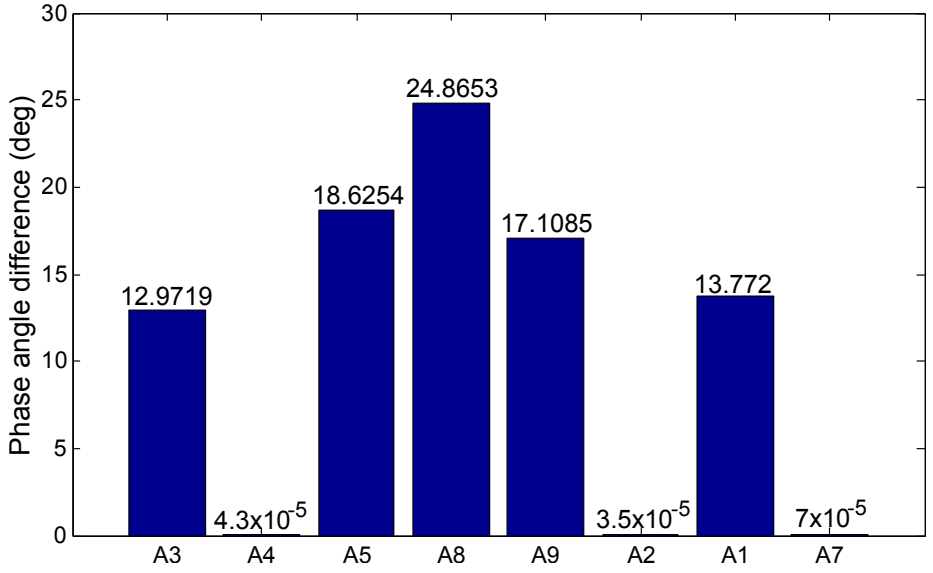


FIGURE 2.4: Reference phase angle difference between control areas.

TABLE 2.9: Reference phase angle difference between subareas

| Subareas | Angle Difference (degrees) |
|---|---|
| From A6 to A3 | 12.971975 |
| From A6 to A4(PMU) | 0.000043 |
| From A6 to A5 | 18.625408 |
| From A6 to A8 | 24.865330 |
| From A6 to A9 | 17.108555 |
| From A3 to A2(PMU) | 0.000035 |
| From A2 to A1 | 13.772086 |
| From A8 to A7 (PMU) | 0.000070 |

#### 2.5.2.2 State Estimation with Bad Data (Gross Measurement Errors)

The set of measurements previously used have been modified by including gross errors in order to test how the normalized residuals method performs for bad data identification in the independent local estimations, once bad data have been detected through the chi-square test. The normalized residuals are obtained by the

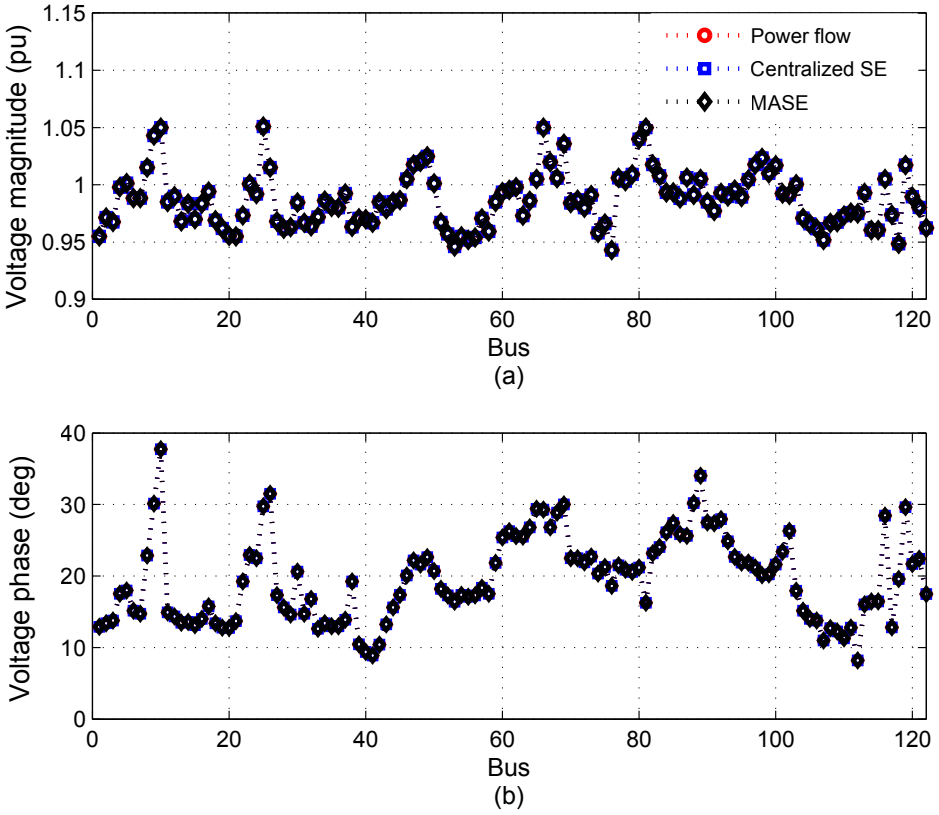


FIGURE 2.5: (a) Nodal voltage magnitudes and (b) nodal voltage phase angles.

TABLE 2.10: Calculated and estimated state variables of FACTS, WTGs and ALFC

| Device | Variable | Power Flow | One Area SE | MASE |
|---|---|---|---|---|
| SVC | $\alpha_{SVC}$ | 136.023 | 136.013 | 136.013 |
| TCSC | $\alpha_{TCSC}$ | 147.965 | 147.965 | 147.965 |
| UPFC | $V_{cr}$ | -0.309474 | -0.309474 | -0.309474 |
| | $\theta_{cr}$ | 112.204 | 112.204 | 112.204 |
| | $V_{vr}$ | 1.34133 | 1.34133 | 1.34133 |
| | $\theta_{vr}$ | 7.9798 | 7.9798 | 7.97983 |
| LTC | $T_k$ | 1.00117 | 1.00117 | 1.00117 |
| PS | $\phi_{TS}$ | -0.840466 | -0.840478 | -0.840468 |
| FSWG1 | $s$ | -0.004041 | -0.004041 | -0.004041 |
| FSWG2 | $s$ | -0.004608 | -0.00461 | -0.00461 |
| SSWG | $R_X$ | -95.8901 | -95.8922 | -95.8918 |
| | $s$ | -0.200883 | -0.200883 | -0.200884 |
| VSWG | $V_m$ | 1.02956 | 1.02956 | 1.02955 |
| | $\theta_m$ | 0.437362 | 0.437362 | 0.437362 |
| | $V_r$ | 0.229501 | 0.229501 | 0.229501 |
| | $\theta_r$ | 3.77123 | 3.77123 | 3.771235 |
| | $V_g$ | 1.025 | 1.025 | 1.02499 |
| | $\theta_g$ | 0.405511 | 0.405511 | 0.405511 |
| PMSG | $V_{gsc}$ | 0.973818 | 0.973818 | 0.973818 |
| | $\delta_{gsc}$ | 25.5995 | 25.5995 | 25.5995 |
| ALFC | $\Delta f$ | 0.110225 | 0.110227 | $Average = 0.110227$ |

TABLE 2.11: Results of the normalized residual method

| Measurement | Device | Area | Iterations | $J(\hat{x})$ |
|---|---|---|---|---|
| P5 | FSWG | A1 | 8 | $2.30268\text{x}10^{-5}$ |
| P113 | SSWG | A2 | 10 | $5.16752\text{x}10^{-5}$ |
| P82 | VSWG | A5 | 9 | $6.27826\text{x}10^{-5}$ |
| P63 | PMSG | A9 | 7 | $5.32504\text{x}10^{-5}$ |
| P25 | ALFC | A4 | 8 | $9.0958\text{x}10^{-5}$ |

division of the measurement residuals over their corresponding standard deviations:

$$\epsilon_i^N = \frac{|\epsilon_i|}{\sqrt{S_{ii}}}, \quad i = 1, ..., N \tag{2.31}$$

where $S_{ii}$ is the ith diagonal element of the residual covariance matrix given by

$$\boldsymbol{S} = \boldsymbol{R} - \boldsymbol{H}\left[\boldsymbol{H}^T\boldsymbol{R}^{-1}\boldsymbol{H}\right]^{-1}\boldsymbol{H}^T. \tag{2.32}$$

The measurement with the largest normalized residual corresponds to the bad data, and it is removed from the set of measurements. A new WLS estimation is carried out with a reduced measurement set, and a bad data analysis is newly performed. This process is repeated until bad data is not detected. Table 2.11 reports the measurements contaminated with gross errors, which are associated with non-conventional devices like WTGs and ALFC. The optimality function values of local estimations in control areas where bad data are located are also shown. Once the gross measurement errors have been locally eliminated, the local estimations give the same results as reported in Table 2.8.

## 2.6 Summary

This chapter proposes a generalized approach to incorporate in a WLS-based state estimator considering different models of FACTS, wind turbine generators, the primary frequency control of generators and a load model depending on voltage and frequency values, which have been neglected so far in the development of static state estimators. The simultaneous estimation of the state variables associated with wind turbine generators, together with the state variables of the rest of the electric network and FACTS controllers embedded in the system, is carried out using the centralized and decentralized state estimation concepts based on measurements provided by a SCADA system and PMUs. In this context, the final

effects of primary frequency regulation is established by estimating the value of frequency deviation in a post-dynamic quasi-stationary state. Lastly, numerical simulations demonstrate that the implementation of the proposed approach gives quite similar results in both types of estimators, however, the decentralized state estimator can be implemented using distributed computation, and also the parameters of the state estimator can be adjusted according to local conditions.

# Chapter 3

# Tracking State Estimation

## 3.1 Introduction

A novel tracking state estimator which simultaneously processes fast rate synchronized phasor and slow rate SCADA measurements is proposed in this chapter. The fact that SCADA measurements, in the most of real applications, are acquired at different rates is exploited by their processing as and when they arrive to the control center. In this case, the time skew effects are reduced by only processing the SCADA measurements received since the last execution of the estimator. In order to assure observability, after each execution of the tracking state estimator all SCADA measurements are forecasted and used as pseudo-measurements in the next estimation. An event detection analysis is also performed for assessing if the system is operating in its quasi-static state; if so, an innovation analysis is then performed for identifying and eliminating grossly inaccurate measurements. The system state is estimated by solving a constrained least-squares optimization problem by using Hachtel's augmented matrix method. In order to improve the tracking state estimation, the option of having time-tagged SCADA measurements is also considered in order to have a larger number of measurements associated with the real system's operation state at a given time. Case studies are presented to illustrate the applicability of the proposed method and to demonstrate its accuracy for tracking the system state even during non-quasi static operation conditions.

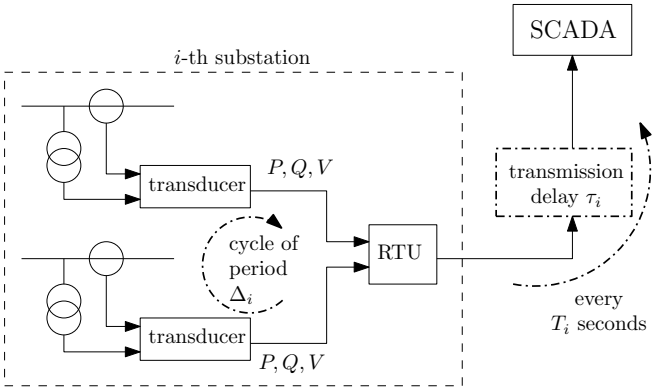


FIGURE 3.1: SCADA measurement gathering process

## 3.2 Principles of the TSE method

### 3.2.1 Time delays affecting SCADA measurements

Today's standard practice in industry for static state estimation assumes that all types of measurements are taken at one point in time [54]. However, the various SCADA measurement values are collected at different times and transmitted to the control center with different delays. Owing to this lack of synchronization, when the system is not in steady state, the solution provided by a static state estimator significantly differs from the true operating state of the monitored system. This is known as the time skew problem.

The SCADA measurement gathering process is shown in Fig. 3.1, which illustrates the communication latency associated with the measurements from two substations [61]. In a given substation, the various measurement devices (transducers) are "visited" cyclically with a time period of $\Delta_i$, which has an order of magnitude of one second, and the measured values are stored sequentially in the memory of the RTU. At a given time $t^*$, the RTU of the $i$-th substation sends the contents of its memory to the SCADA system of the control center, which is received with a transmission time delay $\tau_i$ that is generally below half a second. Note that the transmitted $j$-th measured value is the one stored at the previous time $t^* - \delta_{ji}$ where $\delta_{ji}$ is a value in the interval $[0, \Delta_i]$. While measurements are gathered continuously within the substation, the RTU only communicates with the SCADA system of the control center at regular time intervals $T_i$ that may lie in between two and five seconds, depending on the technology, the age of the equipment, etc.

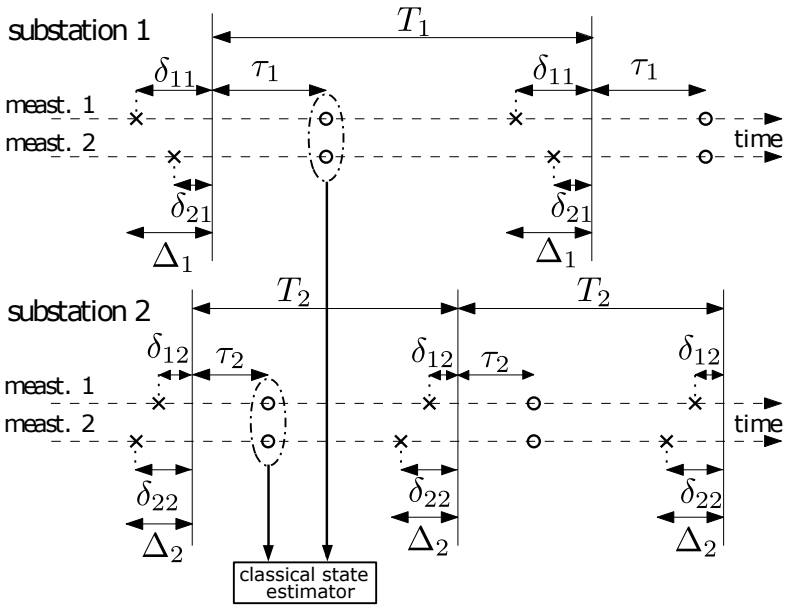


FIGURE 3.2: Delays on SCADA measurements. × indicates the time at which a measurement is taken, ∘ the time at which it is received by the control center.

The various delays are further illustrated in Fig. 3.2, for a hypothetical case of two substations each provided with two measurements. In that figure, a cross indicates the time at which a measurement is taken, and the following circle the time at which it is received by the SCADA system.

### 3.2.2 Principles of the proposed method

Unlike a static state estimator, the TSE processes measurements at short intervals of time in order to follow the changing state. Let $kT_r$ $(k = 0, 1, 2, \ldots)$ be the successive discrete times at which measurements are processed by the TSE.

A distinct procedure is applied to SCADA measurements which are time tagged [76], and to those which are not.

Classical SCADA measurements are not time tagged. Instead, they are processed as and when they are received, as sketched in Fig. 3.3. At a given time $kT_r$, the set of processed measurements is composed of the most recent synchronized (bus voltage and branch current) phasor measurements as well as the new SCADA (voltage magnitude, active or reactive power) measurements that have been received since the last TSE execution, i.e. in the time interval $[(k-1)T_r, kT_r]$. Note that SCADA measurements used at that time are affected by delays $\delta_{ji} + \tau_i + \epsilon_i$ where $\epsilon_i$ is the dead time between the arrival of a measurement and its processing. In order to minimize the effect of time skew, especially when the system is undergoing some

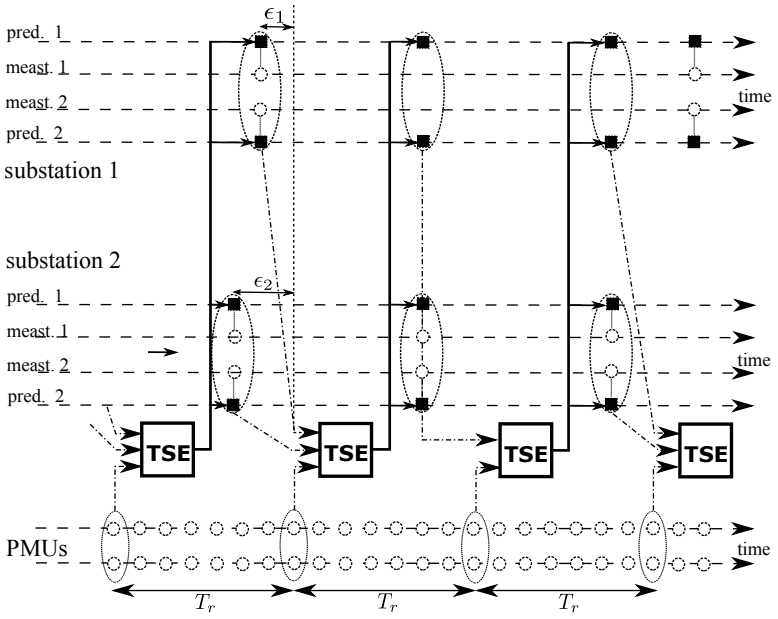


FIGURE 3.3: Use of SCADA, PMU and predicted SCADA measurements in the proposed TSE. ∘ indicates a SCADA measurement, ■ a predicted value.

dynamic changes, all SCADA measurements received before time $(k-1)T_r$ are no longer used.

If time-tagged SCADA measurements are available, the time skew problem can be mitigated. Indeed, when a measurement arrives with the indication that it was taken at time $t'$, it can be assigned to the time interval $[(k-1)T_r\ ,\ kT_r]$ such that $(k-1)T_r \leq t' < kT_r$. Then, the measurements assigned to that interval are processed with a delay in order to ascertain that no further measurement will be assigned to that interval. This is illustrated in Fig. 3.4, where it is shown that the TSE performed at time $t$ processes the SCADA measurements collected in the interval $[t-4T_r\ ,\ t-3T_r]$ and the PMUs relative to time $t-3T_r$. The system state is thus estimated with a delay, denoted $pT_r$ in the sequel. $p=3$ in the example of Fig. 3.4. With $T_r$ in the order of one second, this delay appears reasonable, considering that TSE is used for monitoring, not immediate control purposes. On the other hand, higher accuracy is to be expected since the SCADA measurements used are less dispersed over time.

Even though all PMU measurements are exploited, the use of only a fraction of the whole set of SCADA measurements in each TSE generally results in unobservability. Pseudo-measurements must be added to restore observability. The latter, referred to as *predicted SCADA measurements*, are obtained from the most recent TSEs by predicting the values of the SCADA measurements through a time series analysis.

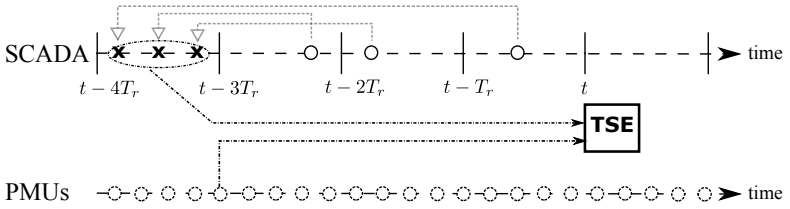


FIGURE 3.4: Processing of time-tagged SCADA measurements. ∘ indicates the time at which a measurement is received, × the time at which it was taken.

Based on the above mentioned information, the TSE processes at time $t$ the subset of SCADA measurements collected in the time interval $[t - T_r\ ,\ t]$ ($[t - (p + 1)T_r\ ,\ t - pT_r]$ if time-tagged SCADA mesurements are exploited), the synchrophasor measurements relative to time $t$ (resp. $t - pT_r$), and the predicted SCADA measurements, to obtain a new estimate of the state vector at time $t$ (resp. $t - pT_r$). These new values of state variables are then used to calculate the estimated values of all quantities measured by the SCADA system, which in turn are employed to predict the values of all SCADA measurements at time $t + T_r$ (resp. $t - (p - 1)T_r$).

Lastly, zero bus injections are included in the formulation as constraints to improve the accuracy of the proposed method.

## 3.3 TSE mathematical formulation

### 3.3.1 Measurement model

Let $m$ be the total number of SCADA measurements. The measurement model is made up of the following equations:

$$\boldsymbol{z}_s(k) = \boldsymbol{D}_k \boldsymbol{h}_s(\boldsymbol{x}(k)) + \boldsymbol{e}_s \tag{3.1}$$

$$\boldsymbol{z}_p(k) = \boldsymbol{h}_p(\boldsymbol{x}(k)) + \boldsymbol{e}_p \tag{3.2}$$

$$\bar{\boldsymbol{z}}_s(k/k-1) = \boldsymbol{\phi}\left[\boldsymbol{h}_s(\hat{\boldsymbol{x}}(k/k)), \bar{\boldsymbol{z}}_s(k/k-1)\right] + \bar{\boldsymbol{e}}_s \tag{3.3}$$

where $\boldsymbol{x}(k)$ is the state vector to be estimated at time $k$, $\boldsymbol{z}_s(k)$ (resp. $\boldsymbol{z}_p(k)$) is the vector of SCADA (resp. PMU) measurements available at time $k$, $\boldsymbol{h}_s(\cdot)$ (resp. $\boldsymbol{h}_p(\cdot)$) are functions relating SCADA (resp. PMU) measurements with the state vector, $\boldsymbol{D}_k$ is built from an $m \times m$ unit matrix by removing the rows corresponding to the SCADA measurements not present at time $k$, $\bar{\boldsymbol{z}}_s(k/k-1)$ is the vector of predicted SCADA measurements available at time $k$, which uses previous TSEs

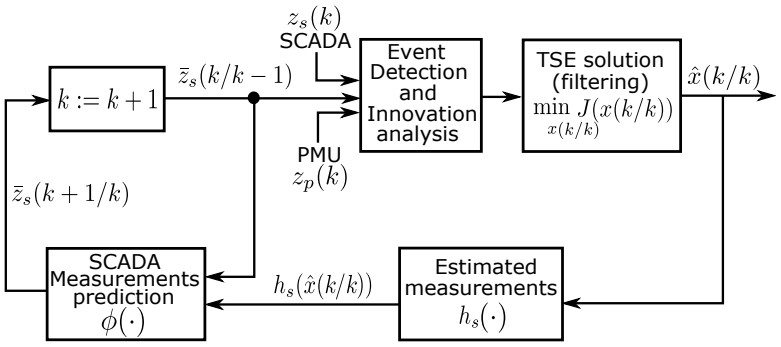


FIGURE 3.5: Main stages of the proposed tracking state estimation.

obtained at $k-1$, $\boldsymbol{\phi}(\cdot)$ is a prediction function, and $\boldsymbol{e}_s$, $\boldsymbol{e}_p$ and $\bar{\boldsymbol{e}}_s$ are unknown vectors of the measurement and prediction errors.

The proposed TSE procedure consists of three steps, shown in Fig. 3.5: SCADA measurement prediction, event detection and innovation analysis, and estimation of the system state.

### 3.3.2 SCADA measurement prediction

In this stage the values of all SCADA measurements are predicted for time $k+1$. Among the various time series analysis methods, see appendix D, Holt's Linear (HL) approach has been selected for its simplicity [51, 77]. It relies on the estimates at the current time $k$ and at the previous time $k-1$ according to:

$$\bar{\boldsymbol{z}}_s(k+1/k) = \boldsymbol{F}_k \; \boldsymbol{h}_s(\hat{\boldsymbol{x}}(k/k)) + \boldsymbol{g}_k \tag{3.4}$$

where:

$$\boldsymbol{F}_k = \alpha(1+\beta)\boldsymbol{I} \tag{3.5}$$

$$\boldsymbol{g}_k = (1+\beta)(1-\alpha)\bar{\boldsymbol{z}}_s(k/k-1) - \beta\boldsymbol{a}_{k-1} + (1-\beta)\boldsymbol{b}_{k-1} \tag{3.6}$$

$$\boldsymbol{a}_k = \alpha\left(\boldsymbol{h}_s(\hat{\boldsymbol{x}}(k/k))\right) + (1-\alpha)\bar{\boldsymbol{z}}_s(k/k-1) \tag{3.7}$$

$$\boldsymbol{b}_k = \beta\left(\boldsymbol{a}_k - \boldsymbol{a}_{k-1}\right) + (1-\beta)\boldsymbol{b}_{k-1}. \tag{3.8}$$

$\boldsymbol{F}_k$ is an estimate of the series "level" and $\boldsymbol{g}_k$ of its slope, both at time $k$, while $\bar{\boldsymbol{z}}_s(k/k-1)$ is the previous vector of predicted SCADA measurements.

### 3.3.3 Innovation analysis and event detection

In static state estimation, anomalous data are most often detected and identified through the (normalized) residuals, which involve the difference between the measured and the estimated values of a SCADA measurement. Dynamic, as well as tracking, state estimation offers an additional data validation, through the innovation vector, i.e. the difference between the predicted and the measured values of a measurement. This test, referred to as innovation analysis, can be performed before the state vector is estimated; it is thus possible to avoid the estimated state to be "contaminated" by the bad data. This is important in so far as the contamination effect of a bad measurement persists in the subsequent dynamic, or tracking state estimations (through the pseudo-measurements $\bar{z}_s$).

On the other hand, it may happen that the components of the innovation vector are abnormally large due to a significant change in the system operating state, which is not reflected by the prediction (3.4). Tracking such changes is precisely the objective of TSE. In this case, larger components of the innovation (and residual) vectors must not be attributed to bad measurements; they have to be accepted as the result of changes taking place in the system, whose effects will hopefully die out in the subsequent TSE runs.

There is thus a need to detect the occurrence of a change in system operation. In the present approach a simple method for event detection is considered. It basically relies on the assumption that synchrophasor measurements are exempt from large errors, other than those resulting from the system dynamics. To detect changes in operating state, incremental changes between successive PMU samples can be checked against a proper threshold. However, keeping in mind the way phasors are calculated [54], or more precisely, the fact that phase angles can change as the data window advances in time owing to the phasor rotation, the test is performed on equivalent power flow measurements. Denoting by $V_i\angle\theta_i$ the voltage phasor at bus $i$ and $I_{ij}\angle\delta_{ij}$ the current phasor in a line connected to that bus, the corresponding active and reactive power flows are:

$$P_{ij}^{eq} = V_i I_{ij} cos(\theta_i - \delta_{ij}) \tag{3.9}$$

$$Q_{ij}^{eq} = V_i I_{ij} sin(\theta_i - \delta_{ij}). \tag{3.10}$$

The variance of the equivalent $P_{ij}^{eq}$ measurement is given by:

$$\sigma_{P_{ij}}^2 = \left[\frac{\partial P_{ij}}{\partial V_i}\right]^2 \sigma_{V_i}^2 + \left[\frac{\partial P_{ij}}{\partial \theta_i}\right]^2 \sigma_{\theta_i}^2 + \left[\frac{\partial P_{ij}}{\partial I_{ij}}\right]^2 \sigma_{I_{ij}}^2 + \left[\frac{\partial P_{ij}}{\partial \delta_{ij}}\right]^2 \sigma_{\delta_{ij}}^2 \tag{3.11}$$

where $\sigma_{V_i}$ is the standard deviation of the noise affecting $V_i$, $\sigma_{\theta_i}$ the one of $\theta_i$, $\sigma_{I_{ij}}$ the one of $I_{ij}$ and $\sigma_{\delta_{ij}}$ the one of $\delta_{ij}$. A similar formula applies to $Q_{ij}^{eq}$.

Accordingly, the event detection test at time $k$ is:

$$v_{P_{ij}} = \left| \frac{P_{ij}^{eq}(k) - P_{ij}^{eq}(k-1)}{\sigma_{P_{ij}}} \right| \overset{?}{>} \gamma \tag{3.12}$$

where $k-1$ and $k$ denote two successive PMU sampling times, and $\gamma$ is a properly chosen threshold. A similar test applies to $Q_{ij}^{eq}$, while changes in voltage magnitude can be merely checked on the measurements directly:

$$v_{V_i} = \left| \frac{V_i(k) - V_i(k-1)}{\sigma_{V_i}} \right| \overset{?}{>} \gamma \tag{3.13}$$

After a change in operating state has been detected, the states obtained by TSE at a few subsequent times (typically a few seconds) are marked as being insufficiently accurate, due to inaccuracy in the forecasting method during the transient response and time skew in SCADA measurements.

On the other hand, if no significant change has been detected, the incoming SCADA measurements can be checked for gross errors using the above mentioned innovation vector. The test applied to the $i$-th measurement is:

$$v_{si}(k) = \left| \frac{[\boldsymbol{z}_s(k)]_i - [\boldsymbol{D}_k \bar{\boldsymbol{z}}_s(k/k-1)]_i}{\sigma_{si}} \right| \overset{?}{<} \psi \tag{3.14}$$

where $\sigma_{si}$ is the standard deviation of the noise affecting that measurement, and $\psi$ is a properly chosen threshold. The measurements for which the test fails are removed from $\boldsymbol{z}_s$. There is no resulting unobservability issue owing to the presence of the pseudo-measurements $\bar{\boldsymbol{z}}_s$.

### 3.3.4 TSE solution (filtering step) method

The correction step yields the estimate of the state vector $\hat{\boldsymbol{x}}(k/k)$ at time $k$, by processing all predicted SCADA measurements $\bar{\boldsymbol{z}}_s(k/k-1)$, the remaining SCADA measurements $\boldsymbol{z}_s(k)$ after the innovation analysis and the latest synchronized phasor measurements $\boldsymbol{z}_p(k)$ in the interval $[k-1,\ k]$.

Assuming Gaussian error distributions, the maximum likelihood estimation of state vector $\boldsymbol{x}(k/k)$ is found by minimizing (3.15), where the objective function is detailed in (3.16), subject to the set of equality constraints corresponding to zero

power injections in transit buses (3.21) and the measurement residuals (3.22), (3.23) and (3.24). In this set of equations, $\boldsymbol{R}$, $\boldsymbol{U}$ and $\boldsymbol{M}$ are diagonal covariance matrices with entries being the variance associated to the various noises in Eqs. (3.1, 3.2, 3.3).

$$\min_{\boldsymbol{x}(k/k)} J(\boldsymbol{x}(k/k)) \tag{3.15}$$

where

$$\begin{aligned} J(\boldsymbol{x}(k/k)) &= \frac{1}{2}\underbrace{[\boldsymbol{z}_s(k) - \boldsymbol{D}_k\boldsymbol{h}_s(\boldsymbol{x}(k/k))]^T\boldsymbol{D}_k\boldsymbol{R}^{-1}\boldsymbol{D}_k^T[\boldsymbol{z}_s(k) - \boldsymbol{D}_k\boldsymbol{h}_s(\boldsymbol{x}(k/k))]}_{\text{SCADA measurements}} \\ &+ \frac{1}{2}\underbrace{[\boldsymbol{z}_p(k) - \boldsymbol{h}_p(\boldsymbol{x}(k/k))]^T\boldsymbol{U}^{-1}[\boldsymbol{z}_p(k) - \boldsymbol{h}_p(\boldsymbol{x}(k/k))]}_{\text{PMU measurements}} \\ &+ \frac{1}{2}\underbrace{[\bar{\boldsymbol{z}}_s(k/k-1) - \boldsymbol{h}_s(\boldsymbol{x}(k/k))]^T\boldsymbol{M}^{-1}[\bar{\boldsymbol{z}}_s(k/k-1) - \boldsymbol{h}_s(\boldsymbol{x}(k/k))]}_{\text{predicted SCADA measurements}} \end{aligned} \tag{3.16}$$

Defining the measurement residual vectors as:

$$\boldsymbol{r}_s = \boldsymbol{z}_s(k) - \boldsymbol{D}_k\boldsymbol{h}_s(\boldsymbol{x}(k/k)) \tag{3.17}$$

$$\boldsymbol{r}_p = \boldsymbol{z}_p(k) - \boldsymbol{h}_p(\boldsymbol{x}(k/k)) \tag{3.18}$$

$$\bar{\boldsymbol{r}}_s = \bar{\boldsymbol{z}}_s(k/k-1) - \boldsymbol{h}_s(\boldsymbol{x}(k/k)) \tag{3.19}$$

the objective function of (3.16) can be rewritten as the weighted sum of squares of residuals:

$$J = \frac{1}{2}\boldsymbol{r}_s^T\boldsymbol{D}_k\boldsymbol{R}^{-1}\boldsymbol{D}_k^T\boldsymbol{r}_s + \frac{1}{2}\boldsymbol{r}_p^T\boldsymbol{U}^{-1}\boldsymbol{r}_p + \frac{1}{2}\bar{\boldsymbol{r}}_s^T\boldsymbol{M}^{-1}\bar{\boldsymbol{r}}_s \tag{3.20}$$

subject to equality constraints corresponding to zero power injections in transit buses:

$$\boldsymbol{f}(\boldsymbol{x}(k/k)) = 0 \tag{3.21}$$

and the residuals of respectively $\boldsymbol{z}_s$, $\boldsymbol{z}_p$ and $\bar{\boldsymbol{z}}_s$:

$$\boldsymbol{r}_s - \boldsymbol{z}_s(k) + \boldsymbol{D}_k\boldsymbol{h}_s(\boldsymbol{x}(k/k)) = 0 \tag{3.22}$$

$$\boldsymbol{r}_p - \boldsymbol{z}_p(k) + \boldsymbol{h}_p(\boldsymbol{x}(k/k)) = 0 \tag{3.23}$$

$$\bar{\boldsymbol{r}}_s - \bar{\boldsymbol{z}}_s(k/k-1) + \boldsymbol{h}_s(\boldsymbol{x}(k/k)) = 0 \tag{3.24}$$

The resulting optimization problem is converted to an unconstrained optimization problem through the Lagrangian function (3.25), whose minimization is achieved through the Hachtel's augmented matrix method by iteratively solving the sparse, symmetric linear system [53]. In this formulation, the following variables are defined: $\boldsymbol{r}' = [\boldsymbol{r}_s \quad \boldsymbol{r}_p \quad \bar{\boldsymbol{r}}_s]^T$; $\boldsymbol{z}' = [\boldsymbol{z}_s(k) \quad \boldsymbol{z}_p(k) \quad \bar{\boldsymbol{z}}_s(k/k-1)]^T$; $\boldsymbol{h}'(\boldsymbol{x}(k/k)) = [\boldsymbol{D}_k\boldsymbol{h}_s(x(k/k)) \quad \boldsymbol{h}_p(x(k/k)) \quad \boldsymbol{h}_s(x(k/k))]^T$; $\boldsymbol{\mu}' = [\boldsymbol{\mu}_s \quad \boldsymbol{\mu}_p \quad \bar{\boldsymbol{\mu}}_s]^T$;

$$\begin{aligned} \mathscr{L} = J(\boldsymbol{x}(k/k)) \quad &- \quad \boldsymbol{\lambda}^T \boldsymbol{f}(\boldsymbol{x}(k/k)) \\ &- \quad (\boldsymbol{\mu}')^T(\boldsymbol{r}' - \boldsymbol{z}' + \boldsymbol{h}'(\boldsymbol{x}(k/k)) \end{aligned} \tag{3.25}$$

Expressing the first-order optimality conditions yields:

$$\partial\mathscr{L}(\boldsymbol{x})/\partial\boldsymbol{r}' = 0 \quad \Rightarrow \quad \boldsymbol{W}\boldsymbol{r}' - \boldsymbol{\mu}' = 0 \tag{3.26a}$$

$$\partial\mathscr{L}(\boldsymbol{x})/\partial\boldsymbol{\mu}' = 0 \quad \Rightarrow \quad \boldsymbol{r}' - \boldsymbol{z}' + \boldsymbol{h}'(\boldsymbol{x}(k/k)) = 0 \tag{3.26b}$$

$$\partial\mathscr{L}(\boldsymbol{x})/\partial\boldsymbol{x} = 0 \quad \Rightarrow \quad \boldsymbol{H}'^T\mu - \boldsymbol{F}^T\lambda = 0 \tag{3.26c}$$

$$\partial\mathscr{L}(\boldsymbol{x})/\partial\boldsymbol{\lambda} = 0 \quad \Rightarrow \quad \boldsymbol{f}(\boldsymbol{x}) = 0 \tag{3.26d}$$

where $\boldsymbol{H}' = \begin{bmatrix} \boldsymbol{H}_s \\ \boldsymbol{H}_p \\ \boldsymbol{H}_s \end{bmatrix} = \begin{bmatrix} \frac{\partial \boldsymbol{h}_s(\cdot)}{\partial \boldsymbol{x}} \\ \frac{\partial \boldsymbol{h}_p(\cdot)}{\partial \boldsymbol{x}} \\ \frac{\partial \boldsymbol{h}_s(\cdot)}{\partial \boldsymbol{x}} \end{bmatrix}$, $\boldsymbol{F} = \frac{\partial \boldsymbol{f}(\cdot)}{\partial \boldsymbol{x}}$ and $\boldsymbol{W}^{-1} = \begin{bmatrix} \boldsymbol{D}_k\boldsymbol{R}\boldsymbol{D}_k^T & 0 & 0 \\ 0 & \boldsymbol{U} & 0 \\ 0 & 0 & \boldsymbol{M} \end{bmatrix}$.

Then the first equation can be eliminated by defining $\boldsymbol{r} = \boldsymbol{W}^{-1}\boldsymbol{\mu}'$, in order to obtain a reduced set of equations:

$$\boldsymbol{W}^{-1}\boldsymbol{\mu}' - \boldsymbol{z}' + \boldsymbol{h}'(\boldsymbol{x}(k/k)) = 0 \tag{3.27a}$$

$$\boldsymbol{H}'^T\boldsymbol{\mu}' - \boldsymbol{F}^T\lambda = 0 \tag{3.27b}$$

$$\boldsymbol{f}(\boldsymbol{x}) = 0 \tag{3.27c}$$

This leads to solving, at the $i$-th iteration ($i = 1, 2, ...$), the sparse, symmetric linear system:

$$\begin{bmatrix} \boldsymbol{W}^{-1} & \boldsymbol{H}' & 0 \\ \boldsymbol{H}'^T & 0 & \boldsymbol{F}^T \\ 0 & \boldsymbol{F} & 0 \end{bmatrix} \begin{bmatrix} \boldsymbol{\mu}'^i \\ \Delta\boldsymbol{x} \\ \boldsymbol{\lambda}^i \end{bmatrix} = \begin{bmatrix} \boldsymbol{z}' - \boldsymbol{h}'(\boldsymbol{x}(k/k)^{i-1}) \\ 0 \\ -\boldsymbol{f}(\boldsymbol{x}(k/k)^{i-1}) \end{bmatrix} \tag{3.28}$$

Using the definitions of $\boldsymbol{r}'$, $\boldsymbol{z}'$, $\boldsymbol{h}'$, $\boldsymbol{\mu}'$, $\boldsymbol{H}'$ and $\boldsymbol{R}'$, equation (3.28) can be expanded in the following form:

$$\begin{bmatrix} \boldsymbol{D}_k\boldsymbol{R}\boldsymbol{D}_k^T & 0 & 0 & \boldsymbol{D}_k\boldsymbol{H}_s & 0 \\ 0 & \boldsymbol{U} & 0 & \boldsymbol{H}_p & 0 \\ 0 & 0 & \boldsymbol{M} & \boldsymbol{H}_s & 0 \\ \boldsymbol{H}_s^T\boldsymbol{D}_k^T & \boldsymbol{H}_p^T & \boldsymbol{H}_s^T & 0 & \boldsymbol{F}^T \\ 0 & 0 & 0 & \boldsymbol{F} & 0 \end{bmatrix} \begin{bmatrix} \boldsymbol{\mu}_s^i \\ \boldsymbol{\mu}_p^i \\ \boldsymbol{\mu}_f^i \\ \Delta\boldsymbol{x} \\ \boldsymbol{\lambda}^i \end{bmatrix} = \begin{bmatrix} \boldsymbol{z}_s(k) - \boldsymbol{D}_k\boldsymbol{h}_s(\boldsymbol{x}(k/k)^{i-1}) \\ \boldsymbol{z}_p(k) - \boldsymbol{h}_p(\boldsymbol{x}(k/k)^{i-1}) \\ \bar{\boldsymbol{z}}_s(k/k-1) - \boldsymbol{h}_s(\boldsymbol{x}(k/k)^{i-1}) \\ 0 \\ -\boldsymbol{f}(\boldsymbol{x}(k/k)^{i-1}) \end{bmatrix} \tag{3.29}$$

and incrementing the state vector according to:

$$\boldsymbol{x}^i(k/k) \;=\; \boldsymbol{x}^{i-1}(k/k) + \Delta\boldsymbol{x} \tag{3.30}$$

Lastly, the first state reconstruction is carried out by using a flat start initialization of state variables, and the last solution $\hat{x}(k-1/k-1)$ is then used as initial condition for subsequent estimations:

$$\boldsymbol{x}^0(k/k) \;=\; \hat{\boldsymbol{x}}(k-1/k-1) \tag{3.31}$$

## 3.4 Simulation Results

### 3.4.1 Test system

The Nordic test system shown in Fig. 3.6 and documented in [78] was chosen to assess the performance of the proposed TSE in significantly disturbed operating conditions.

Its model includes 74 buses, 20 generators, 102 branches, among which 20 step-up and 22 distribution transformers. The study focuses on tracking the system evolution after the outage of line 4032-4044, due to a three-phase solid fault at bus 4032, cleared after five cycles. Two scenarios were considered for the mentioned test system. In the first one, the system experiences long-term voltage

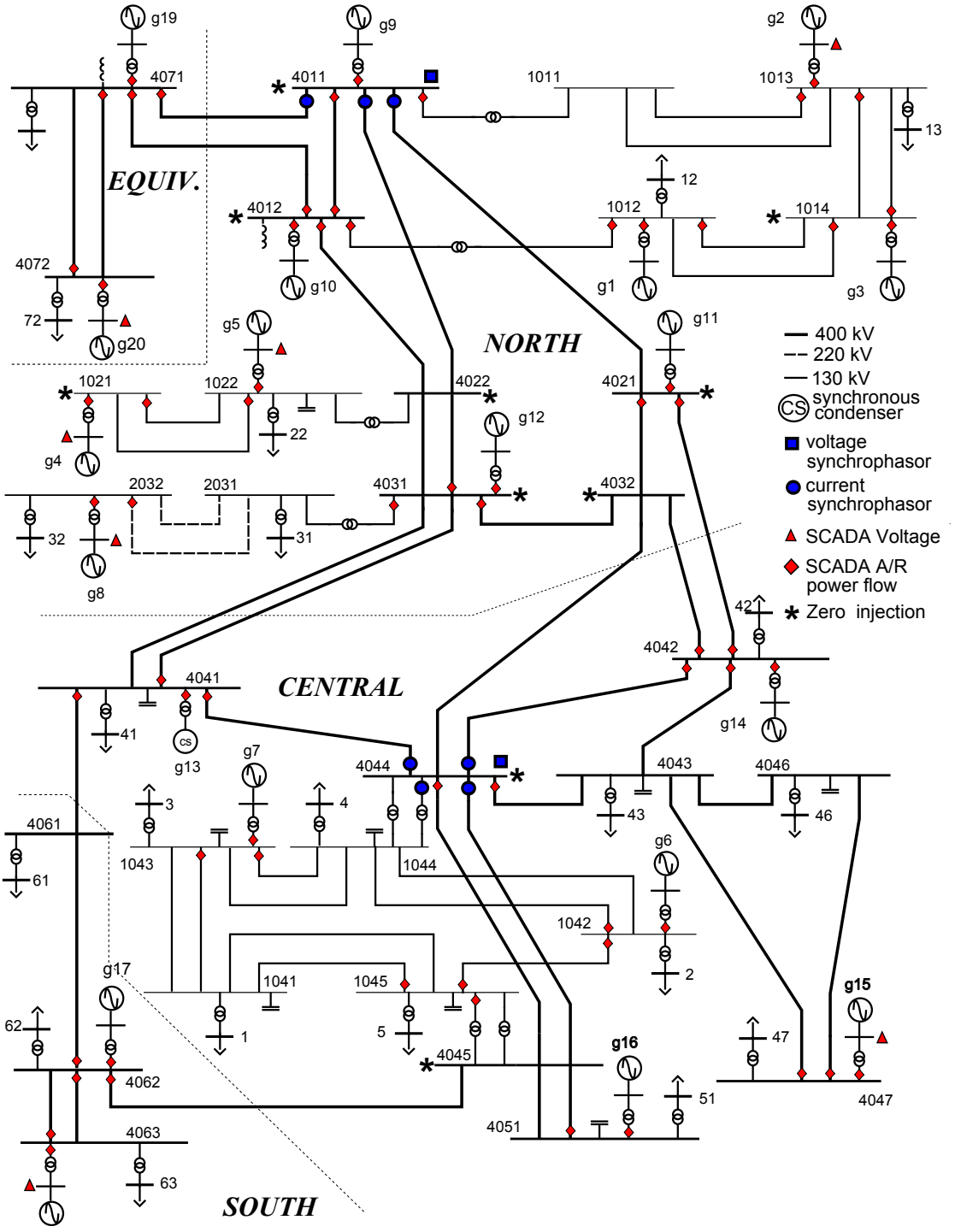


FIGURE 3.6: Nordic system with SCADA and PMU measurement configuration.

instability under the effect of transformer Load Tap Changers (LTCs) and generator Over-Excitation Limiters (OELs). In the second one, stability is restored with an undervoltage load shedding of 100 MW at bus 1041 and 200 MW at bus 1044, performed in several steps [78].

The set of measurements considered in both scenarios is composed of two multi-channel PMUs and 139 SCADA measurements, located in the system as shown in Fig. 3.6. The PMU at bus 4044 provides one voltage and four current synchrophasors, while the one at bus 4011 provides one voltage and three current synchrophasors. On the other hand, SCADA measurements involve seven voltage magnitudes at generator buses and 66 pairs of active/reactive power flows.

The "exact" values of all these measurements were obtained from dynamic simulations of the system response (one for each scenario), considering detailed models of the generators and their controllers, including OELs and LTCs [78].

Next, these values were processed to add time delays in accordance with the gathering of SCADA measurements shown in Fig. 3.2. Namely, it was considered that the $i$-th RTU transmits its set of measurements to the control center every $T_i$ seconds, with $2 \leq T_i \leq 5$. A random communication delay of $\tau_i$ seconds was added, with $0.1 \leq \tau_i \leq 0.5$. It was also considered that measurements in the $i$-th substation are collected at different time instants, leading to a delay of $\delta_{ji}$ seconds for the $j$-th measurement, with $0.1 \leq \delta_{ji} \leq 0.9$.

The TSE also processes ten pairs of zero injections at buses 4011, 4012, 1014, 1021, 4022, 4021, 4031, 4032, 4044 and 4045 through the constraints (3.21).

The 22 distribution buses and the corresponding transformers were not included in the model handled by the TSE, although they were present in the dynamic simulation, experiencing numerous tap changes. This led to a TSE involving 32 transmission and 20 generator buses, and 80 branches. The measurement redundancy is $(139 + 20)/103 = 1.54$ with SCADA data only, and 1.72 with the synchrophasor measurements. These values are deemed moderate, if not low [53].

Network topology was assumed to be updated in the TSE execution that follows the line tripping. On the other hand, the network state was tracked without knowing about the OEL activations, the LTC tap changes and the load curtailments.

In all tests, the period of TSE execution $T_r$ was set to 0.5 second.

### 3.4.2 Measurement and Pseudo-measurement standard deviation

The standard deviation of SCADA power flow measurements is computed as 0.5% of full scale power ($1.5xSnom$) while PMU current measurements were considered

5 times more accurate than SCADA power flow measurements.

$$\sigma_{scada} = \frac{0.005x1.5xS_{nom}}{3xS_{base}} \tag{3.32}$$

$$\sigma_{pmu} = \frac{\sigma_{scada}}{5} \tag{3.33}$$

On the other hand, the predicted SCADA measurements were assumed to be $K$ times less accurate than SCADA measurements.

$$\sigma_f = K\sigma_{scada} \tag{3.34}$$

Table 3.1 and 3.2 show the standard deviation assigned to SCADA and PMU measurements, respectively, which are used in the sequel to compute variance matrices ($R$, $U$ and $M$) and to generate the Gaussian noise added to "exact" values of measurements.

TABLE 3.1: Standard deviation assigned to SCADA power flows and PMU currents. $S_{base} = 100MVA$.

| | | SCADA | PMU |
|---|---|---|---|
| kV | $S_{nom}$ (MVA) | $\sigma_{scada}$ | $\sigma_{pmu}$ |
| 400 | 1400 | 0.03500 | 0.03500/5 |
| 220 | 500 | 0.01250 | 0.01250/5 |
| 130 | 350 | 0.00875 | 0.00875/5 |

TABLE 3.2: Standard deviation assigned to SCADA and PMU voltages.

| | Mag. | Phase |
|---|---|---|
| | $\sigma_{p.u}$ | $\sigma_{p.u}$ |
| SCADA | 0.005/3 | - |
| PMU | 0.001/3 | 0.001/3 |

### 3.4.3 Accuracy Indices

In order to assess the accuracy at time $k$ and over the whole simulation, the following indices have been considered.

The Mean Absolute Percentage Errors (MAPE) evaluate the voltage magnitude mean absolute error (in percent):

$$MAPE(k) = \frac{1}{N}\sum_{i=1}^{N}\frac{|V_i^{ex} - V_i^{est}|}{V_i^{real}}100\% \tag{3.35}$$

$$MAPE = \frac{1}{T}\sum_{k=1}^{T}\frac{1}{N}\sum_{i=1}^{N}\frac{|V_{ik}^{ex} - V_{ik}^{est}|}{V_{ik}^{real}}100\% \tag{3.36}$$

where $N$ is the number of buses, $T$ is the total number of successive TSE executions, the superscript $^{ex}$ denotes exact values, and $^{est}$ estimates.

The Mean Absolute Errors (MAE) assess the accuracy of voltage phase angles (in degrees).

$$MAE(k) = \frac{1}{N}\sum_{i=1}^{N}|\theta_i^{ex} - \theta_i^{est}| \tag{3.37}$$

$$MAE = \frac{1}{T}\sum_{k=1}^{T}\frac{1}{N}\sum_{i=1}^{N}|\theta_{ik}^{ex} - \theta_{ik}^{est}| \tag{3.38}$$

### 3.4.4 Predicted SCADA measurements

For the sake of simplicity and computational efficiency, the $\boldsymbol{M}$ covariance matrix relative to predicted SCADA measurements was approximated by a diagonal matrix whose entries were chosen heuristically as follows.

The standard deviation associated with each predicted measurement was assumed to be $K$ times the corresponding SCADA standard deviation ($\sigma_{s,V}$ or $\sigma_{s,F}$). $K$ was chosen by provisionally taking as prediction of a SCADA measurement the value estimated at the previous TSE execution, as in [61]. $K$ was varied over a wide range, and the value leading to the smallest MAPE index was identified as $K = 3.5$, which has been used in the subsequent simulations.

Using this value of $K$, the $\alpha$ and $\beta$ parameters of the HL prediction (3.5-3.8) were also varied and the combination leading again to the smallest MAPE value was identified as $\alpha = 0.6$ and $\beta = 0.5$, also used in the subsequent simulations.

The results obtained with these settings are already very satisfactory. The fact remains that higher accuracy could be achieved with a more rigorous covariance analysis.

### 3.4.5 Accuracy of TSE

The accuracy of proposed TSE is analyzed through two above mentioned scenarios: *Voltage Collapse* and *Load Shedding*. Initially, the TSE is tested in both scenarios without considering innovation analysis and event detection, however the chi-square test is used to analyze the quality of obtained estimations. Then, the convergence of Hachtel's method is analyzed. Subsequently, an analysis of estimation results is made for both scenarios using time-tagged measurements. After, the proposed bad data and event detection is tested. Finally, an assessment of TSE through Monte-Carlo simulations is performed.

#### 3.4.5.1 Voltage collapse with classical SCADA measurements without considering innovation analysis and event detection

The performance of our proposed TSE is evaluated through the Mean Absolute Percentage of Error (MAPE) for voltage magnitude and Mean Absolute Error (MAE) for phase, Figs. 3.7 and 3.8, respectively. However, the proposed TSE is not designed to carry out accurate estimations during fault transients so first 10s are no taken into account to compute both indexes. Also, in the above mentioned Figures can be observed that the value of $MAPE(k)$ and $MAE(k)$ are relative low except at $t \approx 65s$ which correspond to machine switching under field current limit and $t > 132s$ where the system undergoes on progressive degradation of operating conditions due to long term voltage instability caused by OELs.

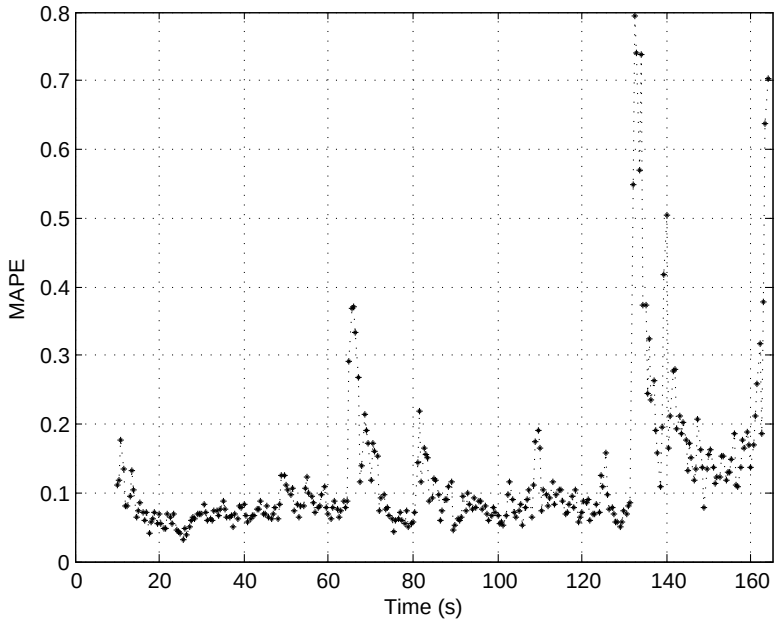


FIGURE 3.7: $MAPE(k)$ index considering classical SCADA measurements; voltage collapse scenario.

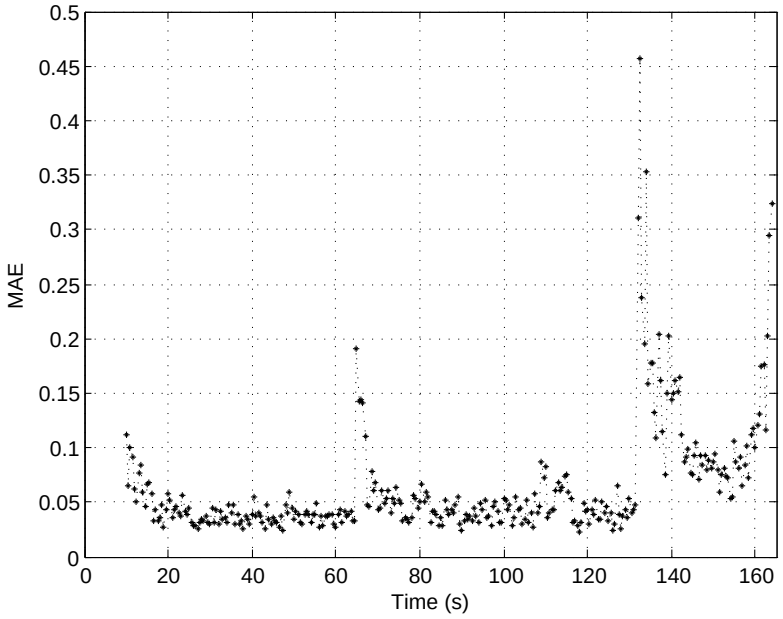


FIGURE 3.8: $MAE(k)$ index considering classical SCADA measurements; voltage collapse scenario.

Figure 3.9 shows the exact evolution (solid line) of voltage magnitude at bus 1042 provided by RAMSES [79], a dynamic simulation tool developed at ULg university, and also the estimation (black asterisk) obtained by proposed TSE. Note that voltage magnitude at bus 1042 is not measured by SCADA or PMU

systems. Additionally, Figs. 3.10 and 3.11 show the exact and estimated voltage magnitude at bus 2032 and 4047, respectively.

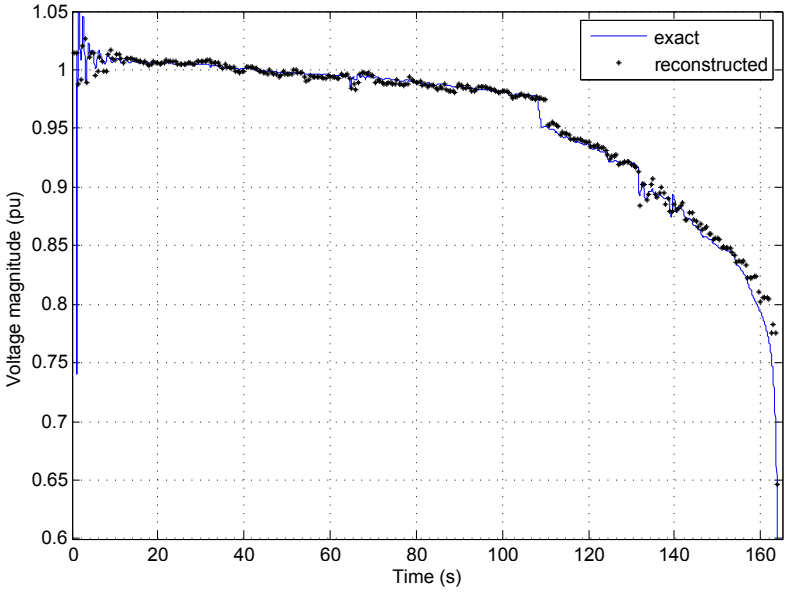


FIGURE 3.9: Exact and estimated voltage magnitude at bus 1042; voltage collapse scenario.

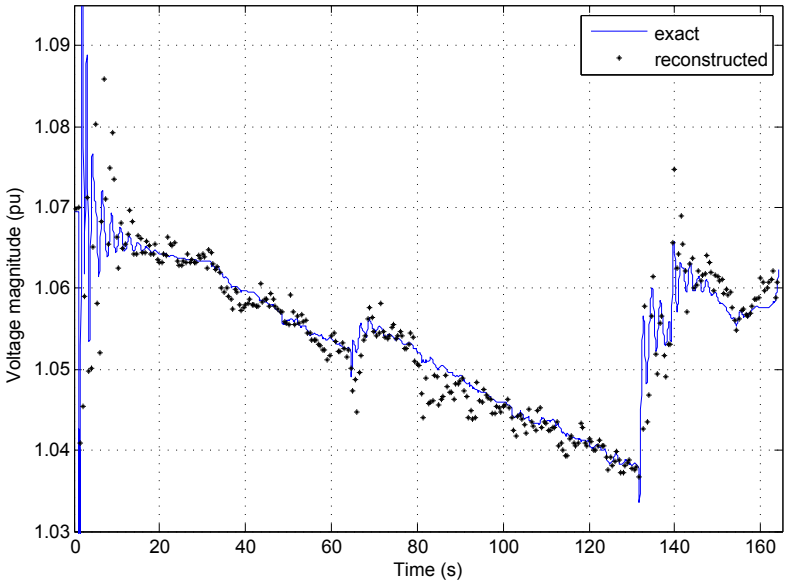


FIGURE 3.10: Exact and estimated voltage magnitude at bus 2032; voltage collapse scenario.

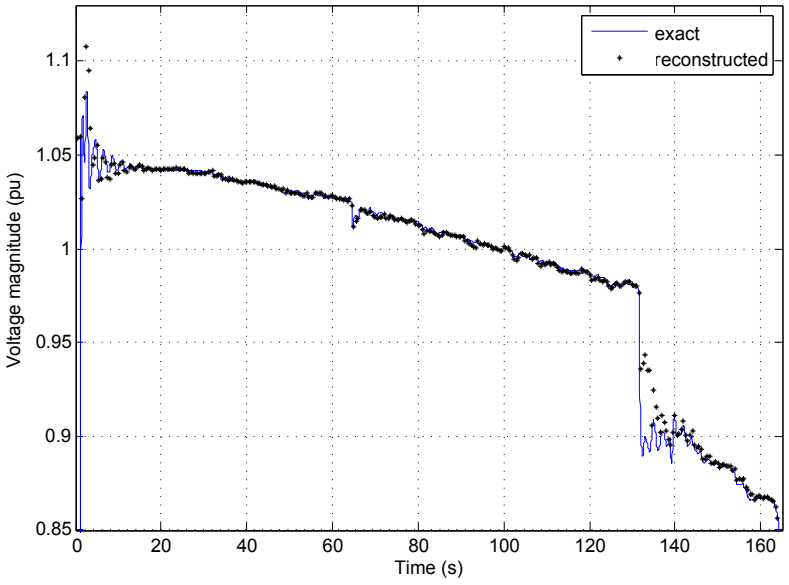


FIGURE 3.11: Exact and estimated voltage magnitude at bus 4047; voltage collapse scenario.

On the other hand, Fig. 3.12 shows the exact evolution (solid line) and tracking estimations (black asterisk) of the active power flow in line 1043-1041.

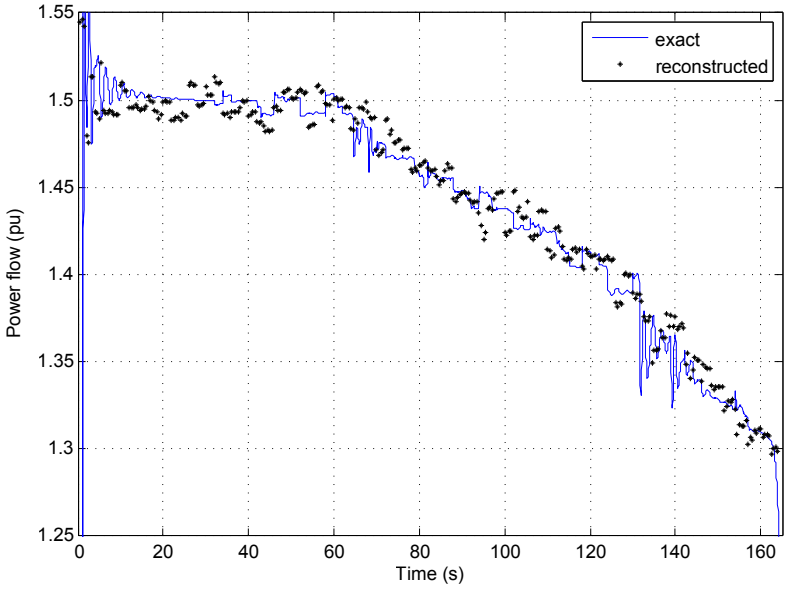


FIGURE 3.12: Exact and estimated active power flow 1043-1041; voltage collapse scenario.

Note that despite the number of SCADA measurements available per estimation is relatively low (*average* = 30 corresponding to 21.43% of total SCADA measurements), as shown in Fig. 3.13, the proposed method is able to solve the optimization problem quite efficiently in terms of the number of iterations required

for tracking dynamic changes in the system state.

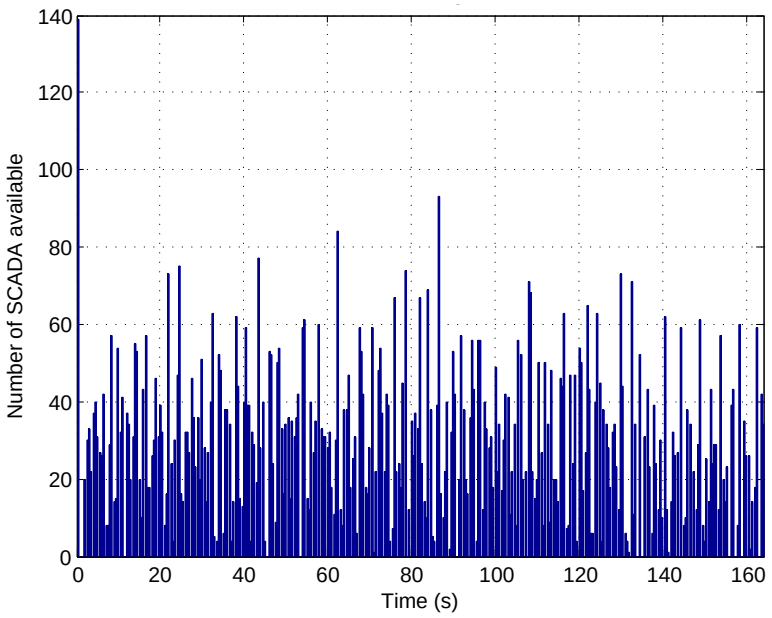


FIGURE 3.13: Number of SCADA measurements available per TSE; voltage collapse scenario.

The number of iterations at each successive tracking estimation is low and remains at the same number over those periods of time where the system does not experience important dynamic changes. When this type of important transients occurs in the system, the estimation requires one additional iteration, as shown in Fig. 3.14.

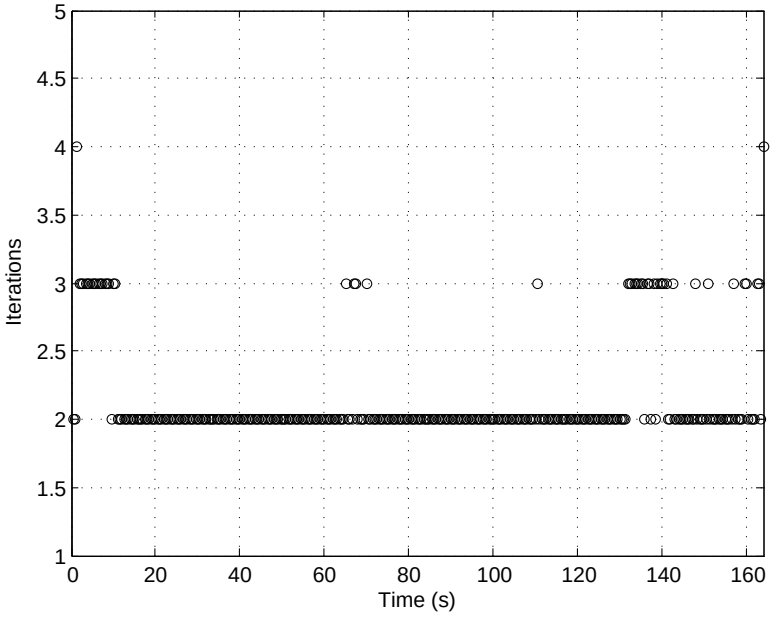


FIGURE 3.14: Number of iterations at each state estimation; voltage collapse scenario.

Finally, the estimations are analyzed by using the Chi-square test, which compare the minimized value of the objective function $J(\hat{x}(k/k))$ with a statistical threshold computed from the Chi-square distribution in order to check whether the state estimates are compatible in accuracy to their corresponding standard deviations. This value corresponds to a detection confidence with probability of 99% and $m - n$ degrees of freedom, where $m$ is the number of measurements plus pseudo-measurements and $n$ is the number state variables $x$. In this case, $m = 2x139 + 18 + 20 = 316$, $n = 2x2 = 104$ and $m - n = 212$. Thus the statistical threshold is 262.82, assuming that all measurements are available.

The values of $J(\hat{x}(k/k))$ of the successive estimations are shown in Fig. 3.15, where the states estimated immediately after any initial disturbance must be considered unreliable [61]; however, $J(\hat{x}(k/k))$ recovers normal values after 10 seconds. Note that $J(\hat{x}(k/k))$ also crosses the threshold rather often (29 times) mainly at those instants corresponding to the initial transient caused by the fault (0-10s), machines switching (65s and 132s) and lost of synchronism of g6 at time 164s.

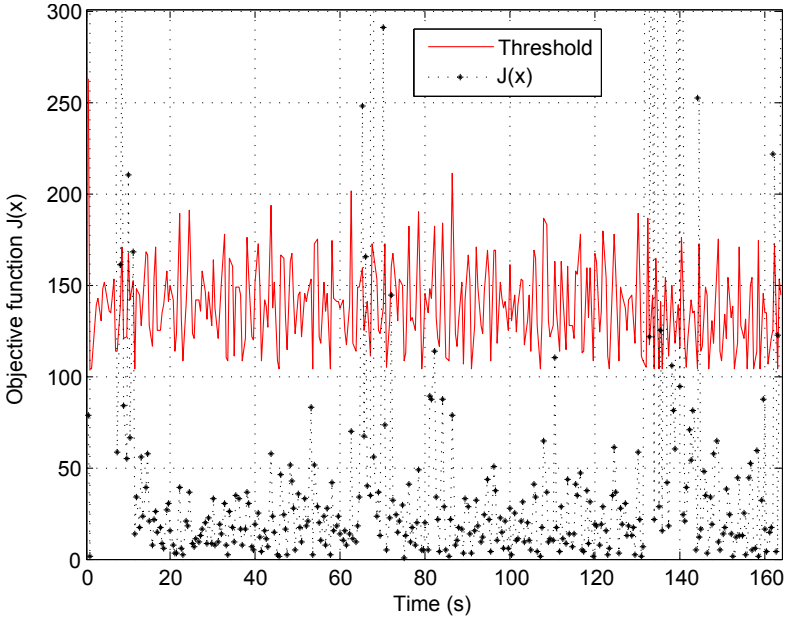


FIGURE 3.15: Objective function values $J(\hat{x}(k/k))$ in successive TSE; voltage collapse scenario.

#### 3.4.5.2 Load shedding using classical SCADA measurements without considering innovation analysis and event detection

This case includes emergency control actions associated with the under-voltage load shedding, which permits to keep a feasible voltage magnitude profile along

the network during the long-term time scale. The load shedding algorithm devised in this research assumes that distributed controllers are delegated a transmission voltage and a group of loads to be controlled. Each controller acts in closed loop, shedding an appropriate amount of load from the nearest distribution bus based on monitoring the voltage magnitude of the closest transmission bus in that area. The adopted scheme acts, according to the following simple logic: shed 50 MW of load when the monitored voltage $V$ goes below a threshold 0.9pu for more than 3 seconds. In the study case described in the past Section, the excitation control system associated with the underexcitation limiter prevents an excessive reduction in the machine excitation at $t \approx 65s$ , which causes voltages drops and a long-term voltage instability. In order to avoid this, six blocks of load are shed, two at the MV bus connected to bus 1041 (at $t \approx 100s$ and $143s$) and four at the MV bus connected to bus 1044 (at $t \approx 112s$, 123s, $180s$ and $292s$), for a total load shedding of 300 MW.

Figures 3.16 and 3.17 show the results of $MAPE(k)$ and $MAE(k)$ indexes, respectively. A comparison of the values of these indexes with respect to those obtained for the voltage collapse scenario shows that the performance of the proposed TSE improves when emergency control actions are taken, which is an expected result because the system is less stressed.

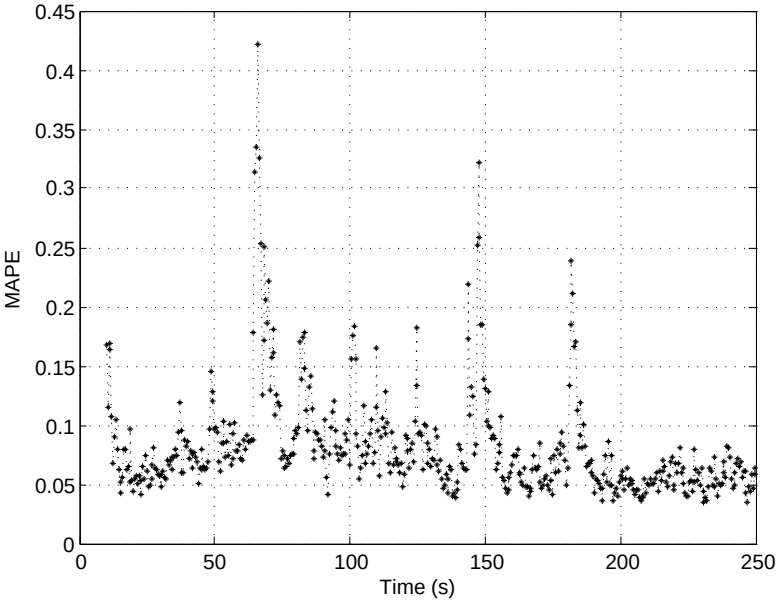


FIGURE 3.16: $MAPE(k)$ index considering classical SCADA measurements; load shedding scenario.

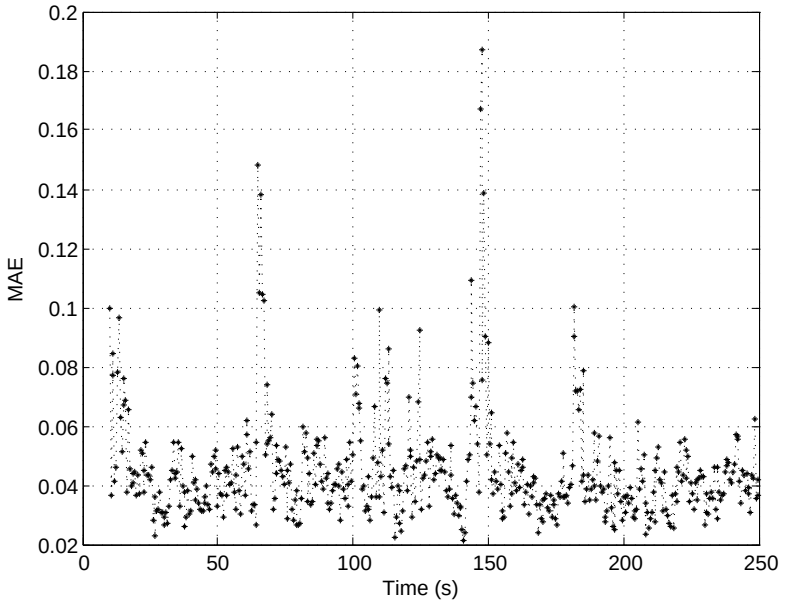


FIGURE 3.17: $MAE(k)$ index considering classical SCADA measurements; load shedding scenario.

From Fig. 3.18 can be noticed that the estimation of voltage magnitude is quite satisfactory even during load shedding events.

The estimated voltages magnitude at buses 2032 and 4047 are also shown in Figs. 3.19 and 3.20, respectively, with respect the "exact" values of these variables obtained from a dynamic simulation. This comparison demonstrates that the tracking of these voltage evolutions is satisfactory despite that buses at which these estimations are performed are relatively far from installed PMUs.

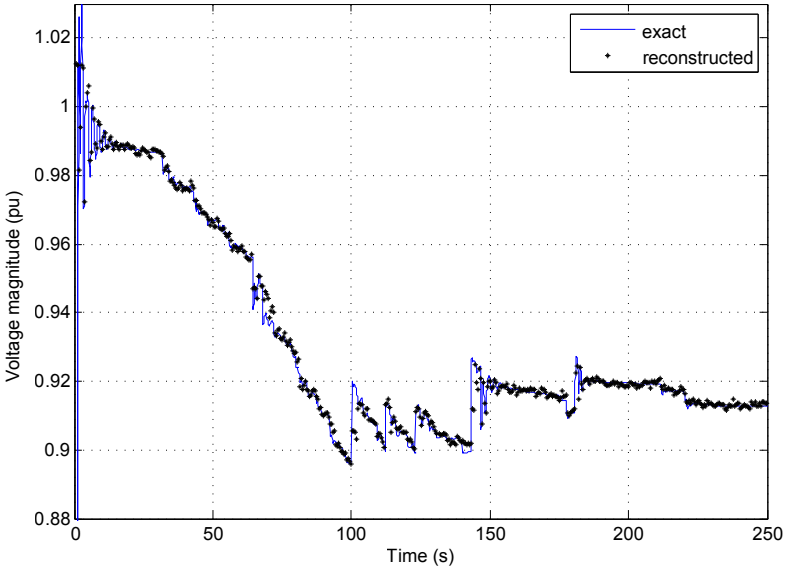


FIGURE 3.18: Exact and estimated voltage magnitude at bus 1041; load shedding scenario.

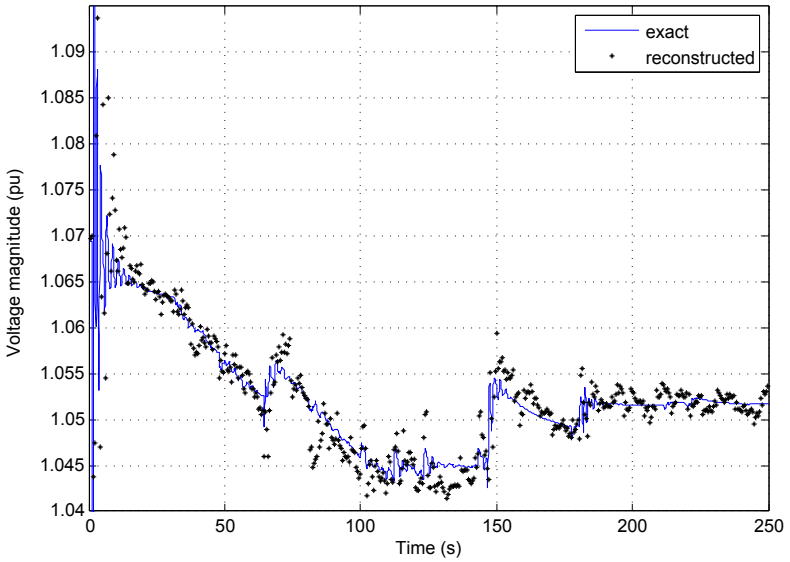


FIGURE 3.19: Exact and estimated voltage magnitude at bus 2032; load shedding scenario.

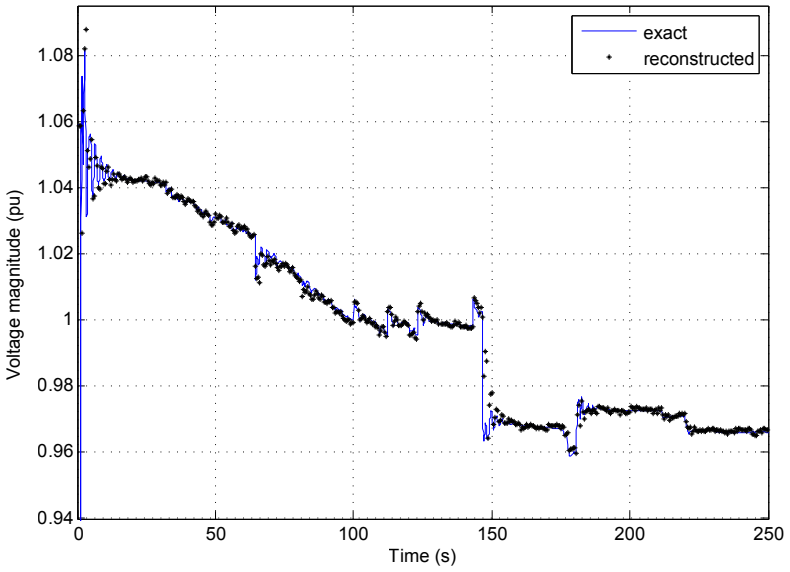


FIGURE 3.20: Exact and estimated voltage magnitude at bus 4047; load shedding scenario.

Figure 3.21 also shows the "exact" and estimated evolutions of the active power flow in line 1043-1041.

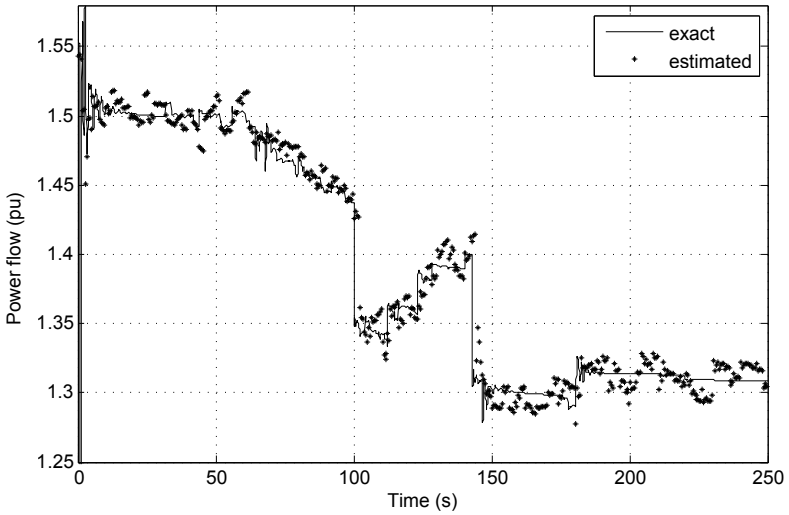


FIGURE 3.21: Exact and estimated active power flow in line 1043-1041; load shedding scenario.

The average number of SCADA measurements available per reconstruction is 25, as shown in Fig. 3.22, corresponding to 17.72% of total SCADA measurements while the number of iterations at each successive state estimation is shown in Fig. 3.23.

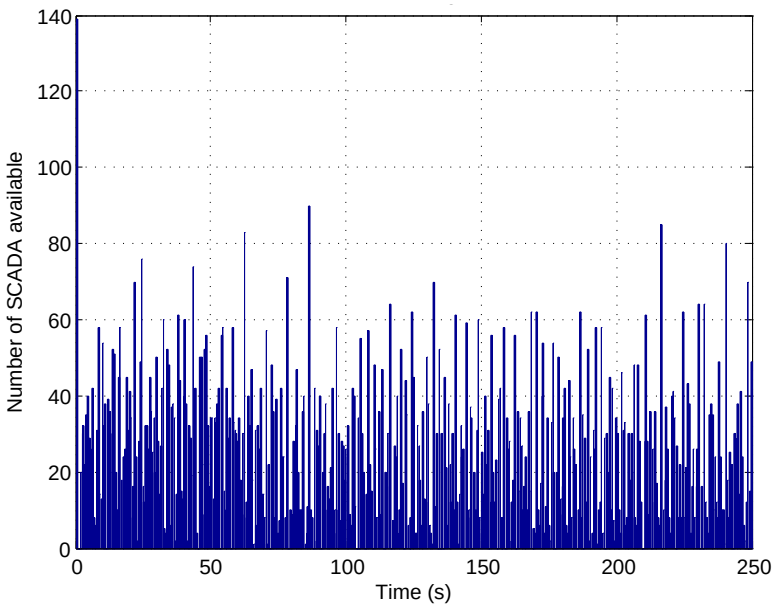


FIGURE 3.22: Number of SCADA measurements available per TSE; load shedding scenario.

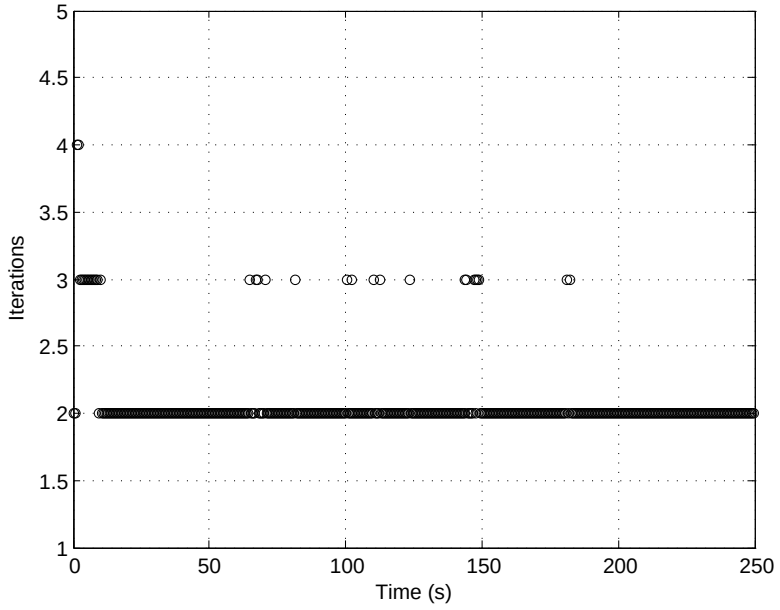


FIGURE 3.23: Number of iterations at each TSE; load shedding scenario.

Finally, the values of $J(\hat{x}(k/k))$ of the successive estimations are shown in Fig. 3.24, where some values are higher than the statistical threshold, mainly due to the fault transient ($0 \leq t \leq 10$s ), change in the operation of generators ($t \approx 65$) and load shedding ($t \approx 147$ and $t \approx 182$). Despite there is no bad data introduced to measurements, anomalies are expected to be detected after system transients because of the time skew problem of SCADA measurements and also because all predicted measurements assume a trend behavior based in pre-disturbance information.

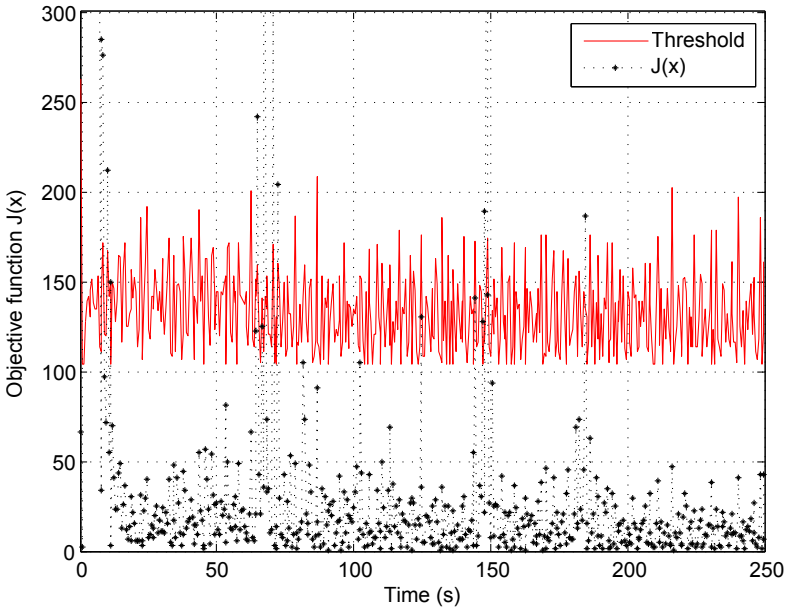


FIGURE 3.24: Objective function values $J(\hat{x}(k/k))$ in successive TSE; load shedding scenario.

#### 3.4.5.3 Convergence of Hachtel's method

Table 3.3 gives an account of the number of estimations during the whole time period of study that required two, three or four iterations of the Hachtel's method outlined in Section 3.3.4. The iterations are stopped when $\max_j |[\Delta \boldsymbol{x}^i]_j| < 10^{-4}$ and the highest values correspond to states estimated during large transients. This, and the availability of efficient solvers for symmetric sparse matrices allows running TSE very frequently.

TABLE 3.3: Number of iterations of Hachtel's method

| | Number of estimations with | | | |
|---|---|---|---|---|
| Scenario | 2 iter. | 3 iter. | 4 iter. | 5 iter. or more |
| Voltage collapse | 280 | 46 | 2 | 0 |
| Load shedding | 465 | 33 | 2 | 0 |

#### 3.4.5.4 Comparison of TSE results with time-tagged and classical SCADA measurements for voltage stability and load shedding cases

The exact and tracked long-term evolutions of the most affected voltage magnitude in the voltage collapse scenario are shown in Fig. 3.25 for the case where classical SCADA measurements are processed, and in Fig. 3.26 when their time-tagged counterparts are used. Small boxes inside figures show zoomed views of

the estimated voltages at the time where sudden changes take place in the system. The final voltage collapse (corresponding to a loss of synchronism of g6) is not

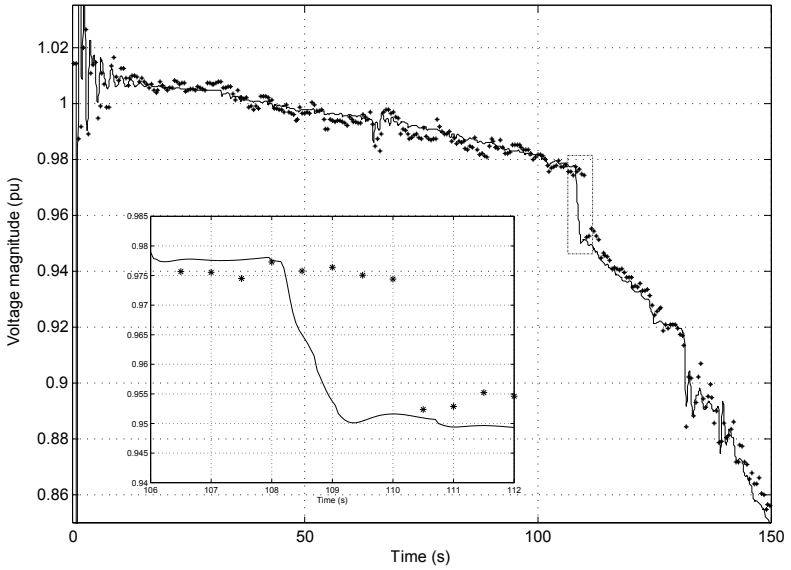


FIGURE 3.25: Exact and tracked voltage magnitude at bus 1042 using classical SCADA and synchrophasor measurements; voltage collapse scenario.

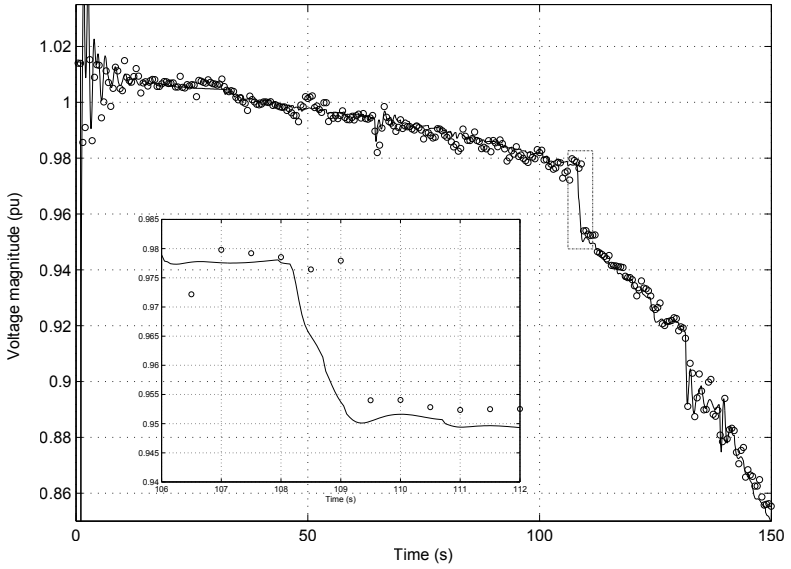


FIGURE 3.26: Exact and tracked voltage magnitude at bus 1042 using time-tagged SCADA and synchrophasor measurements; voltage collapse scenario.

shown, to preserve legibility. In both figures, the exact evolution is shown with solid line, while the estimated values are shown with asterisks (resp. circles) when the SCADA measurements do not come (resp. come) with time stamps. The corresponding results in the case with stabilization by load shedding are given in Figs. 3.27 and 3.28, respectively.

The plots provide evidence that the proposed TSE is able to track the network state evolution, in particular when changes take place in the system, for instance

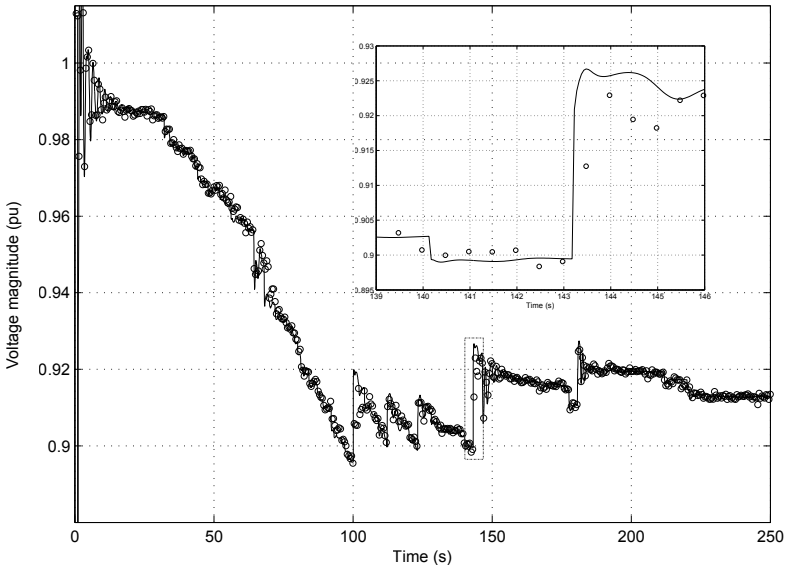


FIGURE 3.27: Exact and tracked voltage magnitude at bus 1041 using classical SCADA and synchrophasor measurements; load shedding scenario.

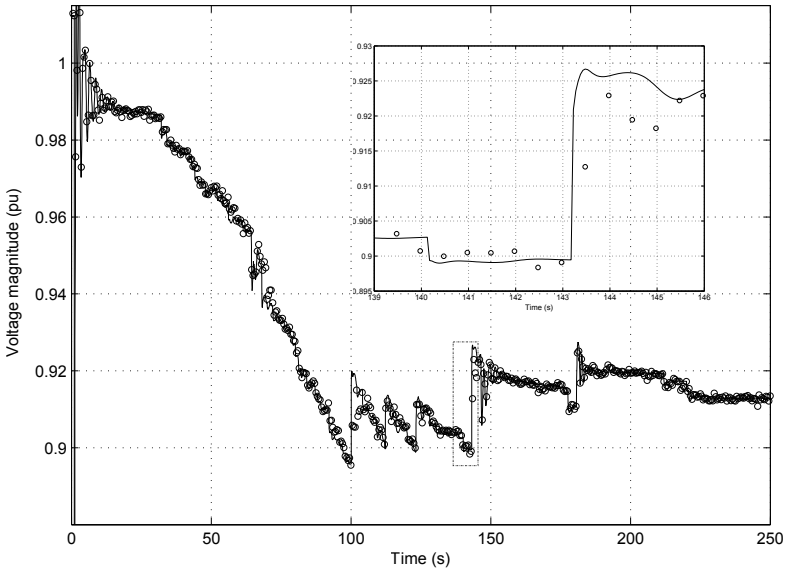


FIGURE 3.28: Exact and tracked voltage magnitude at bus 1041 using time-tagged SCADA and synchrophasor measurements; load shedding scenario.

due to remedial actions. Expectedly, the state estimation is not satisfactory during the large transients that follow the fault itself, but after 10 to 15 seconds, TSE realigns on the system evolution.The zoomed views in Figs. 3.25 to 3.28 confirm that after a sudden change in the system (in the shown case, an OEL activation), the tracked evolution follows the exact one with a delay, caused by the non-synchronized SCADA measurements and the absence of PMUs near the bus of concern. This delay, however, is rather short when classical SCADA measurements are used, and slightly reduced when time-tagged SCADA measurements are processed.

The values of MAPE and MAE indexes are given in Table 3.4 in the aforementioned

TABLE 3.4: MAPE and MAE indices

| | $MAPE$ (%) | $MAE$ (deg) |
|---|---|---|
| No disturbance | 0.057854 | 0.036848 |
| Voltage Collapse scenario | 0.121980 | 0.063582 |
| Same with time-tagged SCADA | 0.107020 | 0.056033 |
| Load Shedding scenario | 0.082208 | 0.044838 |
| Same with time-tagged SCADA | 0.076298 | 0.043544 |

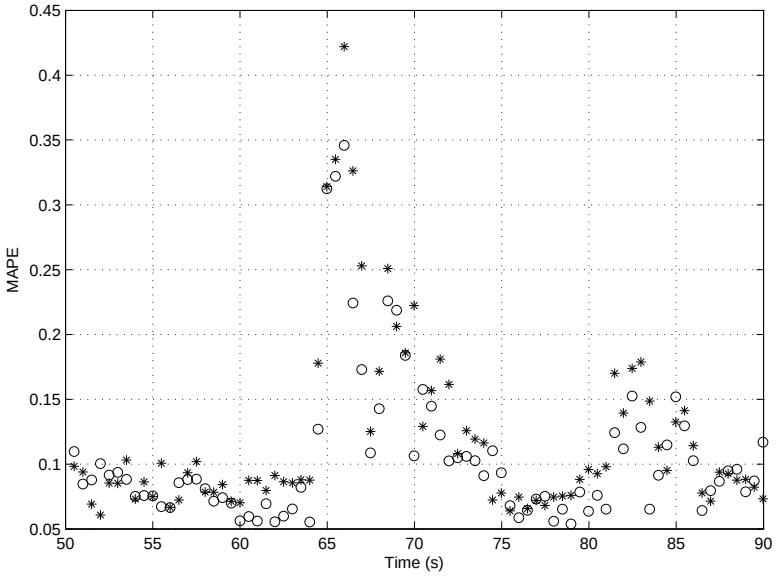


FIGURE 3.29: $MAPE(k)$ index considering classical SCADA (asterisks) and time-tagged SCADA (circles) measurements; load shedding scenario.

two scenarios as well as when the system is in steady state. The later case is for reference, since the TSE errors result from measurement noise only (no transient, no time skew). For the above mentioned reason, the first ten seconds after fault clearing were not included in the calculation of the indexes. These results confirm that using time-tagged SCADA measurements improves the overall accuracy of TSE.Moreover, a comparison of the $MAPE(k)$ indices with and without time-tagged SCADA measurements is shown in Fig. 3.29 for the load shedding scenario. The higher index values occur at times in which sudden changes take place. This justifies to label inaccurate the estimates provided by a number of TSE executions after an event has been detected.

### 3.4.6 Bad data and event detection

The innovation analysis and event detection is illustrated by considering the case of a gross error of 10 $\sigma_{s,F}$ affecting the active power flow $P_{4041-4031}$ at $t = 35.1$ s, in the load shedding scenario. The successive innovation values for this measurement,

involved in the test (3.14), are shown in Fig. 3.30, from which a gross error is easily observed at $t = 35.5$ s. At the same time instant, the tests (3.12) and (3.13) do not reveal any significant change in the operating state: the largest $v_{P_{ij}}$ value for all PMUs is 0.9604. Hence, the large innovation value is attributed to a bad measurement.

On the contrary the large innovation values observed at $t = 3.0$, 5.5, and 8.5 s, respectively, are due to the transients triggered by the fault. At these times, the tests (3.12) and (3.13) are positive, indicating that the system undergoes significant changes instead of a gross measurement error (and, hence, the estimates are flagged as inaccurate during a few TSE executions after each of these times).

In the tests reported here, the values $\psi = 4.5$ in (3.14) and $\gamma = 6.5$ in (3.12, 3.13) were found to provide a good compromise between false alarms and non detections.

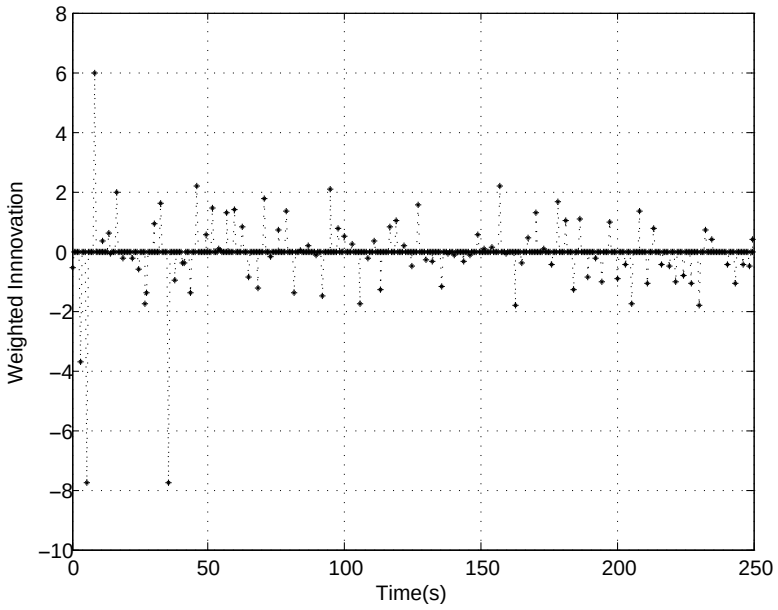


FIGURE 3.30: Innovation values for active power flow $P_{4041-4031}$ measurement.

### 3.4.7 TSE assessment through Monte-Carlo simulations

A more systematic assessment of the TSE accuracy was performed through Monte-Carlo simulations. A set of $s = 500$ simulations was built, differing by the random noise applied to the measurements, as well as by random transmission delays $\tau_i$ in the interval [0.1, 0.5] s. For each voltage magnitude and power flow provided with a SCADA measurement, the mean and standard deviations of the corresponding

$s$ estimates was computed, for each of the $T$ TSE executions, as follows:

$$\mu_j(k) = \frac{1}{s}\sum_{i=1}^{s} e_{j,i}(k) \tag{3.39}$$

$$\sigma_j(k) = \sqrt{\frac{1}{s}\sum_{i=1}^{s}\left(e_{j,i}(k) - \mu_j(k)\right)^2} \tag{3.40}$$

$$\text{where :} \quad e_{j,i}(k) = h_j(\hat{\boldsymbol{x}}_i(k/k)) - h_j(\boldsymbol{x}(k)) \tag{3.41}$$

is the estimation error of the $j$-th measured quantity, at the $k$-th discrete time ($k = 1, \ldots, T$), provided by the $i$-th simulation ($i = 1, \ldots, s$). Then, for each measured quantity, a global mean and standard deviation were computed over all $T$ discrete times according to:

$$\bar{\mu}_j = \frac{1}{T}\sum_{k=1}^{T} \mu_j(k) \tag{3.42}$$

$$\bar{\sigma}_j = \sqrt{\frac{1}{T}\sum_{k=1}^{T} \sigma_j(k)^2}. \tag{3.43}$$

This analysis was performed in the two aforementioned scenarios as well as in the case with no disturbance.

TABLE 3.5: Standard deviations of measurement noise and estimation errors for three measured active power flows (in pu)

| Line | Meas. noise | No disturb. | Load Shedding scenario | | Voltage Collapse | |
|---|---|---|---|---|---|---|
| | $\sigma_{s,F\,j}$ | $\bar{\sigma}_j$ | $\bar{\mu}_j$ | $\bar{\sigma}_j$ | $\bar{\mu}_j$ | $\bar{\sigma}_j$ |
| 4047-4043 | 0.0350 | 0.031725 | 0.002575 | 0.028968 | -0.003132 | 0.032219 |
| 2032-2031 | 0.01250 | 0.009531 | 0.002153 | 0.012002 | 0.004168 | 0.010977 |
| 1043-1041 | 0.00875 | 0.007760 | 0.001860 | 0.006883 | 0.001730 | 0.007706 |

For a sample of three active power flows, Table 3.5 shows the standard deviation of the measurement noise $\sigma_{s,Fj}$ and the $\bar{\mu}_j$ and $\bar{\sigma}_j$ statistics. It can be seen that the bias $\bar{\mu}_j$ is very small. The values of $\bar{\sigma}_j$ being smaller than those of $\sigma_{s,Fj}$ reveal the filtering capability of the proposed TSE in spite of the significant system transients and the small number of PMUs. Fig. 3.31 shows the mean ($\mu_j(k)$, $\bar{\mu}_j$) and standard deviation ($\sigma_j(k)$, $\bar{\sigma}_j$) for line 1043-1041 in normal operation case.

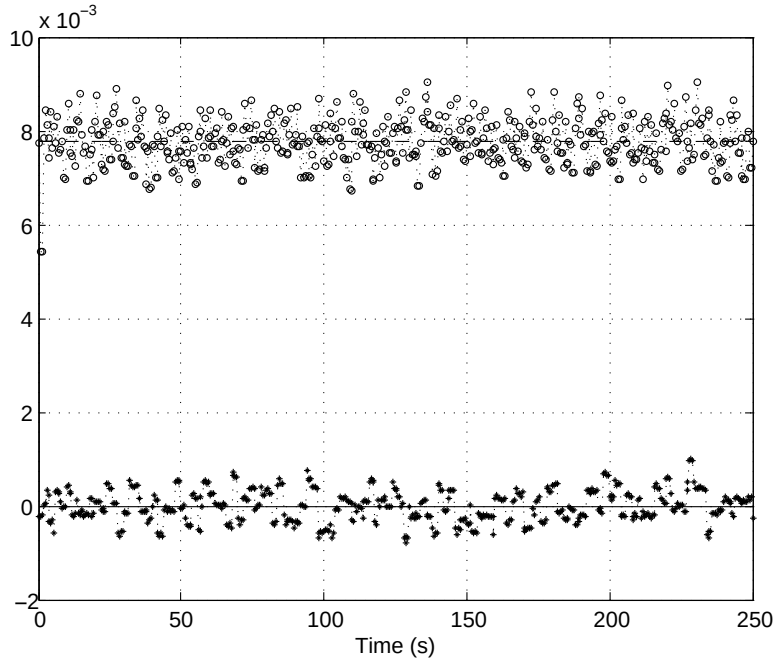


FIGURE 3.31: Mean and standard deviations of active power flow in line 1043-1041 (normal operation).

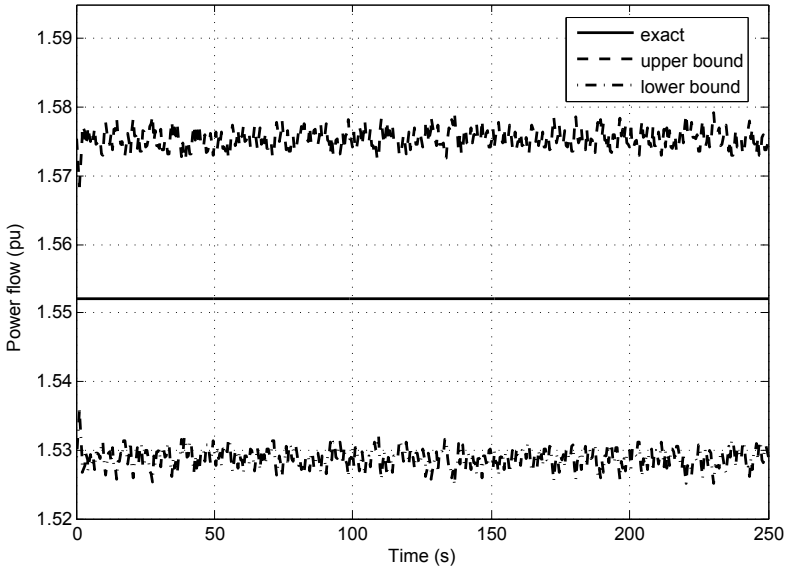


FIGURE 3.32: Exact and bounds of active power flow in line 1043-1041; normal operation scenario.

Finally, Figs. 3.32 to 3.38 show the exact and upper and lower bounds of active power flow (computed as: $P_j^{exact} \pm 3\sigma_j(k)$) in lines 1043-1041, 2032-2031, 4047-4043 for three different scenarios: normal operation (no transient, no time skew), voltage collapse and load shedding.

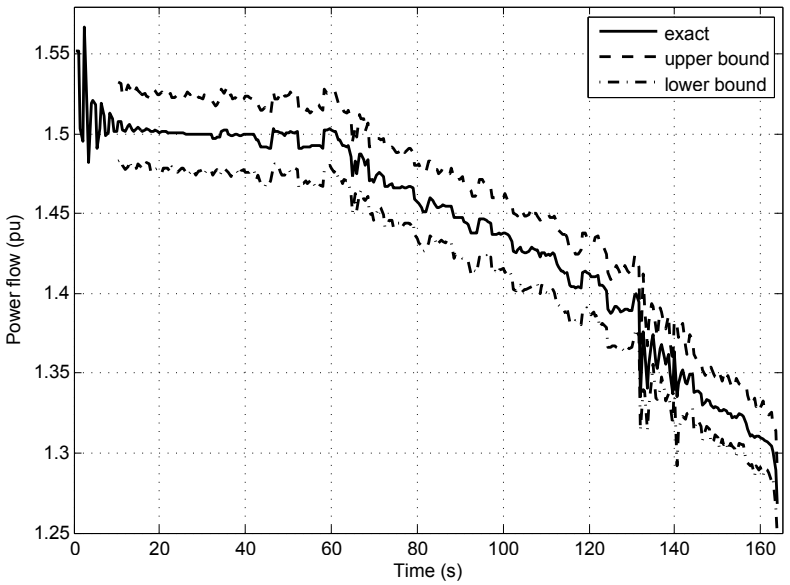


FIGURE 3.33: Exact and bounds of active power flow in line 1043-1041; voltage collapse scenario.

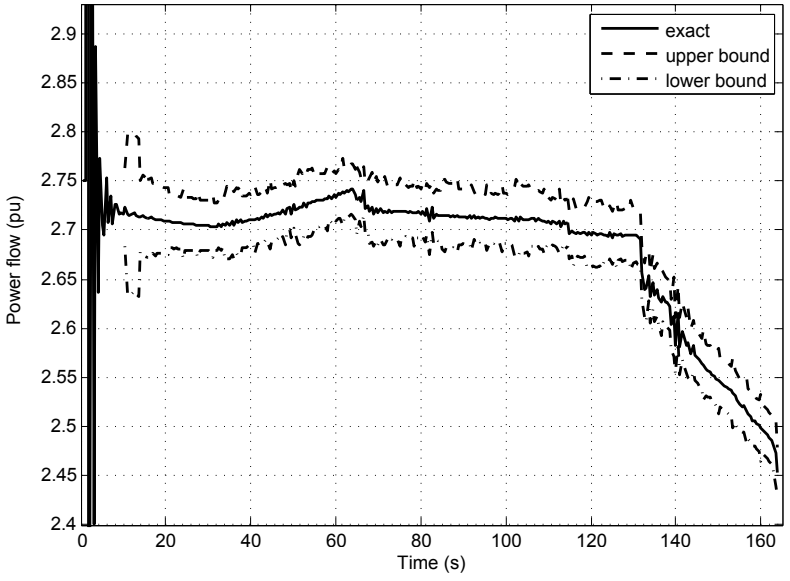


FIGURE 3.34: Exact and bounds of active power flow in line 2032-2031; voltage collapse scenario.

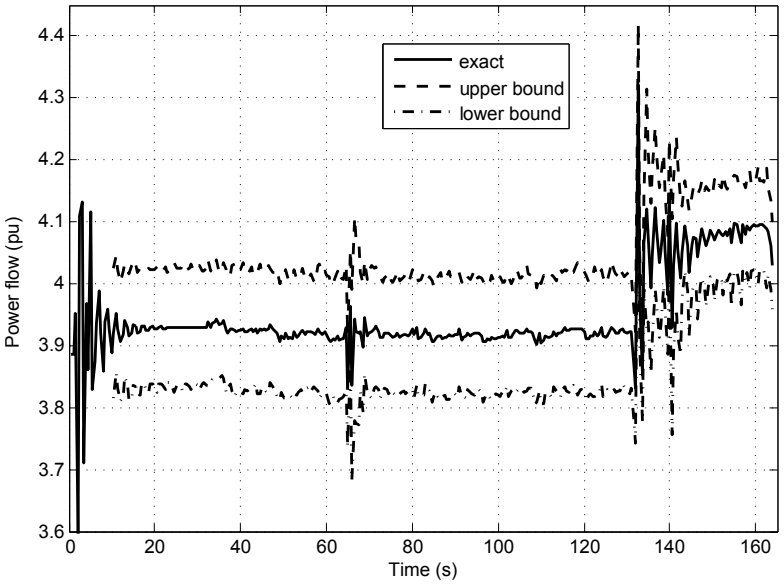


FIGURE 3.35: Exact and bounds of active power flow in line 4047-4043; voltage collapse scenario.

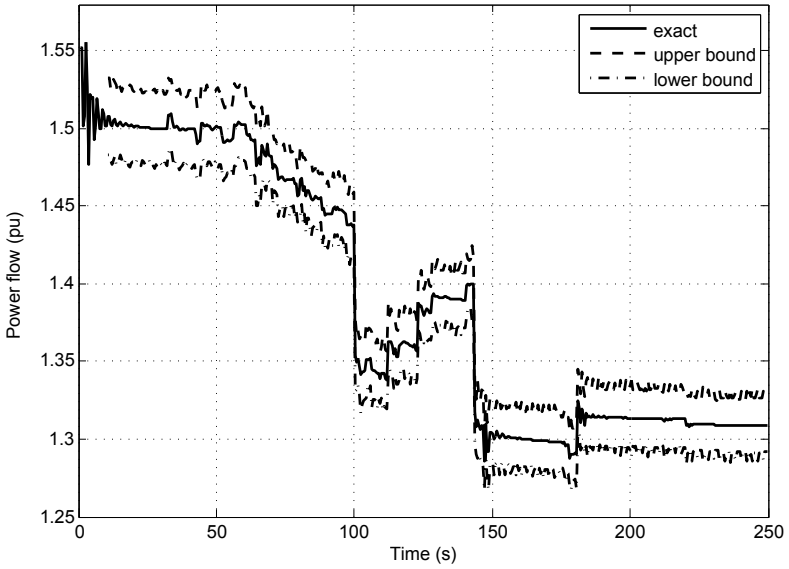


FIGURE 3.36: Exact and bounds of active power flow in line 1043-1041; load shedding scenario.

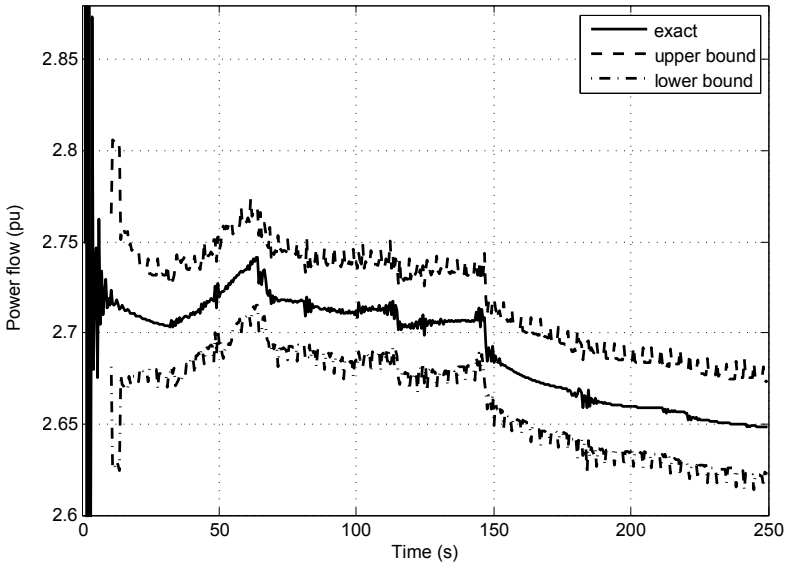


FIGURE 3.37: Exact and bounds of active power flow in line 2032-2031; load shedding scenario.

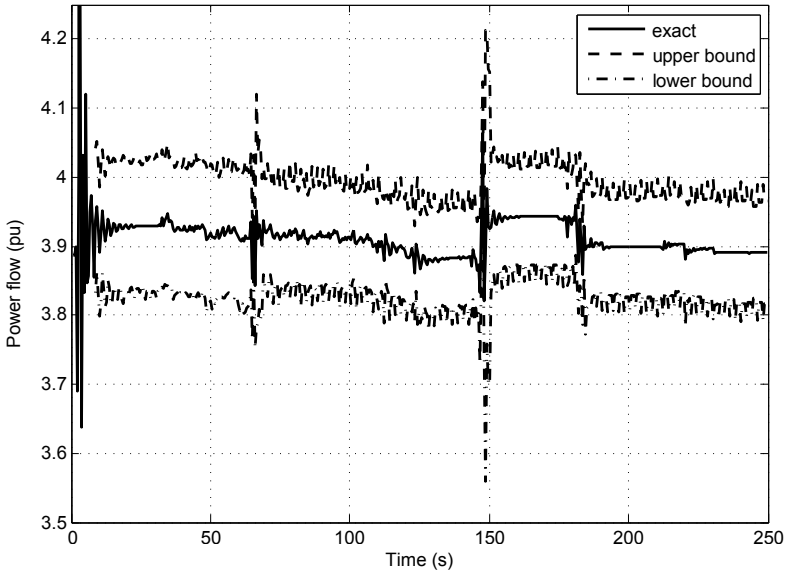


FIGURE 3.38: Exact and bounds of active power flow in line P4047-4043; load shedding scenario.

## 3.5 Summary

A novel state estimation has been presented, aimed at tracking the changes of network state. The main advantage of the proposed method is the simultaneous processing of measurements gathered at different rates: SCADA measurements processed as and when they arrive, together with a limited number of synchrophasor measurements. Predicted SCADA measurements are used to ensure observability. A combined analysis of synchronized measurement variations and innovation vectors has been proposed to distinguish between sudden changes in system state and gross errors affecting the SCADA measurements.

In the tests, heuristic weights have been assigned to the predicted SCADA measurements. It is certainly worth investigating how a more accurate covariance matrix could be used instead, although Monte-Carlo simulations confirm noise filtering capabilities even when the aforementioned sub-optimal weights are used.

Regarding innovation analysis, the approach relies on the assumption that there is no bad data affecting synchrophasor measurements, so that their change with time can be used to detect sudden changes in system operating point. This assumption is worth being assessed in greater detail.

Nevertheless, the results already show the ability of the proposed method to track the network state evolution even under severe conditions.

Furthermore, time-tagged SCADA measurements can be exploited. This mitigates the time skew effect but requires running the TSE with a delay.

# Chapter 4

# Final remarks and suggestions for future research work

## 4.1 General conclusions

The state estimator constitutes the backbone of energy management systems because its application permits the estimation of the complete operation state of the system (voltage and phase angle at each node) based on the measurements taken from the field, and at the same time also provides the network topological model and initial conditions for the values of the system's state variables to perform other types of power system studies such as: power flow, optimal power flow, contingency analysis, economic dispatch, among others. Hence, the proper performance of the state estimator is of paramount importance for the operation and control of electric power systems in "real time". In this context, and in order to assist power system engineers to estimate the operating point of a power system, both established and emerging power components must be modeled alongside each other in a unified frame of reference in order to include them in a state estimator algorithm.

This research work describes the implementation of a decentralized Multi-area State Estimation using a weighted least square algorithm, which is capable to estimate the system state variables as well as state variables of FACTS controllers, wind generators and the system frequency deviation in a unified frame. The formulation for implementing FACTS controllers (PST, LTC and SVC), Wind Generators (FSWG and SSWG) and Automatic Load Frequency devices into the hybrid state estimator has been described in detail. Simulations have been carried out on

a modified IEEE 118 bus test system where FACTS, WG and ALFC devices are added in order to illustrate the prowess of the proposed approach.

This thesis also describes a novel method for tracking state estimation based on combining SCADA (Supervisory Control And Data Acquisition) and synchronized phasor measurements provided by Phasor Measurements Units (PMUs) along with pseudo-measurements, which are included to make the system observable. Pseudomeasurements have been obtained by using exponential smoothing methods, in such a way that for each SCADA measurement a pseudo-measurement is computed with its proper weight, which allows to carry out an innovation analysis over SCADA measurements. Accordingly, batch of measurements are processed as soon as they are available. Since pseudo-measurements can be inaccurate, however, two set of constraints are added to improve the performance of the proposed TSE: zero power injections in transit buses and measurements residuals. The proposed objective function is then solved by using Hachtel's augmented matrix method which has a good computational performance. A detailed simulations on the Nordic system have been carried out in RAMSES, a dynamic simulation tool, to obtain the system evolution under long-term disturbance conditions and to provide the SCADA and PMU "measurements" to the TSE. The time skew problem and Gaussian random noise affecting SCADA measurements are also included to make the scenario more realistic. A sensibility study through Monte Carlo simulations has been been carried out in order to quantify the noise effect on the accuracy of the proposed tracking estimator. In this context, two indexes have been implemented to measure the accuracy of the proposed tracking estimator. Finally, simulation results shows that the TSE produces quite accurate estimations even in scarce PMU configurations and severe disturbances. Furthermore, Monte-Carlo simulations have confirmed that the method is able to filter measurement noise. On the other hand, despite an execution time of 0.5 s is used for all simulations with satisfactory results, smaller estimation times can be used to improve the tracking capability of the proposed method but at the expense of an increase in computation time.

## 4.2 Future work

Departing from the static and tracking state estimator proposed in this work, new proposals for future research work are proposed below:

1. **Static State Estimation**:

   - To develop or implement direct methods in the generalized static state estimation as continued fraction power flow.
   - To develop a rectangular formulation with tensor methods in order to enhance the solution of SSE problem.

2. **Tracking State estimation**:

   - To develop a methodology to adjust standard deviation of SCADA measurements to take into account time skew in the state estimation problem.
   - Despite the optimal location of PMU was not addressed in this thesis, note the need for the optimal placement of PMUs because they are assumed to be in limited number.
   - Diagnostics of unreliable TSE caused by excessive transients.
   - To apply a TSE at higher rates, with the objective of tracking faster dynamics.

3. **Dynamic State Estimation**:

   - To develop a methodology to carry out a dynamic state estimation plus trajectory sensitivity analysis in order to determine the angular stability of a power system.

4. To develop a **software** for rapid testing of state estimator tasks, with the following characteristics:

   - User defined models.
   - Measurement pre-filtering.
   - Topology processor.
   - Parameter estimation.
   - Observability analysis.
   - Static, forecasting, tracking, dynamic, transient and power quality state estimation.
   - Bad data detection, identification and elimination.
   - Solution methods (WLS, Hachtel, given rotations, decoupled, WLAV, etc.).

- Filtering techniques (Kalman filter, extended Kalman filter, etc.).
- Multi-area state estimation.
- PMU placement.
- Parallelization techniques (multi-treading, multi-processing, GPU architetures, FPGA, etc.), to test algorithms in large power system.

# Appendix A

# Energy Management Systems

Maintaining integrity and economy of an inter-connected power system requires significant coordinated decision-making. So one of the primary functions of the energy control centers is to monitor and regulate the physical operation of the interconnected grid. This task is generally performed through three main integrated subsystems: the energy management system (EMS), the supervisory control data acquisition (SCADA), and the communications interconnecting the EMS and the SCADA.

## A.1 Energy Management System

An energy management system (EMS) is composed of a set of computer-aided tools used by operators of electric utility grids for the purpose of monitoring, controlling and optimizing the operation of geographically dispersed transmission and generation assets in real-time.

A modern energy management system is characterized with the following subsystems:

1. **The production planning subsystem** which provides information relative to the economic scheduling of generation and dispatchable transactions for the near term future.

    - Load Forecasting
    - Resource Scheduling (Unit Commitment)

2. **The generation control subsystem** that manages the power generation, controls the system frequency and the control area net interchange at their scheduled values, and optimizes the operation of the system. An example of functions within this subsystem is:

   - Economic Dispatch (ED)
   - Automatic Generation Control (AGC)

3. **The network applications software** that comprises all computer programs which are utilized in the control and operation of a power system, such as:

   - State Estimation (SE)
   - Dispatcher's Load Flow (DLF)
   - Optimal Power Flow (OPF)
   - Contingency Analysis (CA)
   - Voltage Security Assessment
   - Dynamic Security Assessment
   - Total Transfer Capability Calculation

4. **The dispatcher training simulator** which provides a realistic method for training power system operators, such as:

   - DTS Similar Day Load Data
   - DTS Power System Simulator

Figure A.1 shows the functional diagram of a modern energy management system [80] where for clarity, the production planning and generation control systems are grouped as energy/economy system and the network applications software are divided in data acquisition and security monitoring subsystems. The hardware sketch comprising the SCADA system is not in the scope of this research work and then is not presented in this appendix.

Despite the state estimator and its functions (measurement prefiltering, topology processor, observability analysis, state estimation and bad data processor) was explained in Chapter 1, the data acquisition subsystem is briefly describe in this appendix the present research work focus on state estimation of electric power systems by simultaneously processing all asynchronously available real-time measurements provided by a SCADA system and synchrophasor measurements.

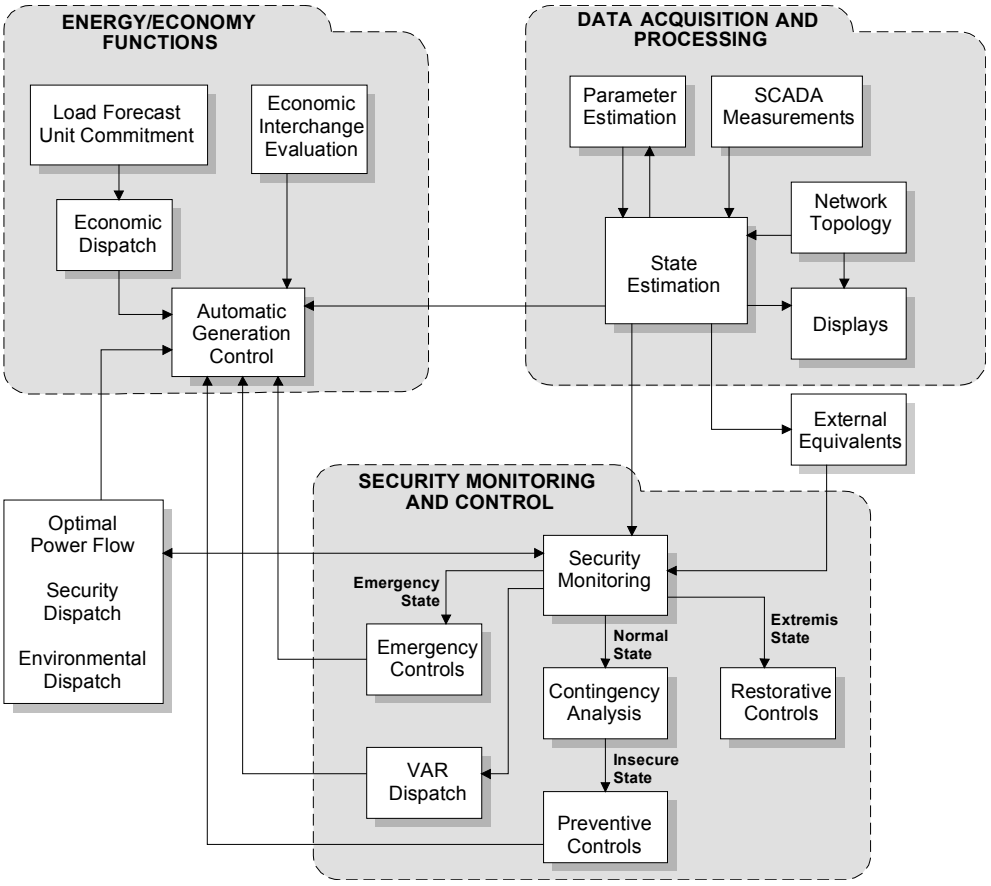


FIGURE A.1: Functional diagram of a modern energy management system.

## A.2 Supervisory Control And Data Acquisition

The Supervisory Control And Data Acquisition(SCADA) obtains measurements from RTUs that collects analog measurements (i.e. voltage magnitude, power flows, etc.) and the topological status of the network (i.e. status of breakers, switches, etc.), which in turn are transmitted to the control center via the communication channels [80]. At the control center, the topology of the network is build and the state of the system is obtained by the state estimation. The results are then displayed in a man machine interface. The EMS also allows the remote control of RTU internal and external devices (tripping of breakers, changes of transformer taps, etc.).

The RTUs have a set of values that are updated every 0.1 s to 10.0 s. and they are usually described as "real time" even though the values may be seconds old [81]. Table A.1 shows typical performance requirements for measurements.

TABLE A.1: Typical measurement services performance requirements.

| **Enterprise/function** | **Example** | **Update periodicity** (s) | **Accuracy** (%) | **Time Skew SCADA** (s) |
|---|---|---|---|---|
| **Tier 1** | | | | |
| Substation operator indications | Voltage, Bus | 5 | 0.3 | 1 |
| Switching and tagging | Voltage, Line | 5 | 0.3 | 1 |
| End element control | Real and Reactive Power, Line | 10 | 1.0 | 1 |
| Low-priority alarm | Real and Reactive Power, Equip | 10 | 1.0 | 1 |
| High-priority alarm | Current, Line | 5 | 0.3 | 1 |
| System restoration | Current, Equip | 5 | 0.3 | 1 |
| | Frequency/Phase Angle | 1-5 | 0.3 | 1 |
| | Position, Regulator/valve | 10 | 1.0 | 1 |
| | Ancillary value | 10 | 1.0 | 1 |
| **Tier 3** | | | | |
| Auto Gen Control | Voltage, Bus | 2 | 0.3 | 1 |
| Auto restoration | Voltage, Line | 2 | 0.3 | 1 |
| Sectionalizing | Real and Reactive Power, Line | 2 | 1.0 | 1 |
| | Real and Reactive Power, Equip | 2 | 1.0 | 1 |
| | Current, Line | 2 | 0.3 | 1 |
| | Current, Equip | 2 | 0.3 | 1 |
| | Frequency/Phase Angle | 2 | 1.0 | 1 |
| | Position, Regulator/valve | 10 | 1.0 | 1 |
| | Ancillary value | 10 | 1.0 | 1 |
| **Tier 4** | | | | |
| State Estimation | Voltage, Bus | 15 | 0.3 | 1 |
| Operator Load Flow | Voltage, Line | 15 | 0.3 | 1 |
| Optimal Power Flow | Real and Reactive Power, Line | 15 | 3.0 | 1 |
| Contingency Analysis | Real and Reactive Power, Equip | 15 | 3.0 | 1 |
| Security Surveillance | Current, Line | 15 | 3.0 | 1 |
| | Current, Equip | 15 | 3.0 | 1 |
| | Frequency/Phase Angle | 30 | 3.0 | 1 |
| | Position, Regulator/valve | 30 | 1.0 | 1 |
| | Ancillary value | 30 | 1.0 | 1 |

## A.3 Phasor Measurement Unit

A Phasor Measurement Unit (PMU) or synchrophasor is a device that measures the magnitude and phase angle of voltages and currents across the power grid by making use of the synchronized time signal provided by the global positioning system. This time synchronization allows to collect synchronized real-time measurements of multiple remote measurement points on the grid. In this context, data are stored in a Phasor Data Concentrator (PDC) and transmitted via communication channels to the control center.

One of the most important features of the PMU technology is that the measurements are time-stamped with high precision using the Global Positioning System (GPS), such that all PMU measurements with the same time-stamp can be used to infer the state of the power system [54]. In [54] theoretical aspects of PMUs are addressed as well as practical implementation aspects of the PMUs and phasor data concentrators (PDCs), communication systems, etc.

Based on the mentioned above, phasor measurement units are much more faster and accurate than SCADA measurements. Table A.2 shows data reporting rates required for 50 Hz and 60 Hz systems. Other reporting rates are permissible, and including higher rates like 100/s or 120/s or rates lower than 10/s such as 1/s is encouraged [82].

TABLE A.2: PMU reporting rates

| **System frequency** | **50 Hz** | | | **60 Hz** | | | | | |
|---|---|---|---|---|---|---|---|---|---|
| Reporting rates (frames per second) | 10 | 25 | 50 | 10 | 12 | 15 | 20 | 30 | 60 |

# Appendix B

# Power System Component Modeling

## B.1 Steady state models

This appendix describes the mathematical models $h(\cdot)$ of all devices used for simulations in this thesis.

### B.1.1 Transmission line

Transmission lines are represented by a two-port $\pi$-model whose parameters correspond to the positive sequence equivalent circuit of transmission lines [53]. A transmission line with a positive sequence series impedance of $r + jx$ and total line charging susceptances of $j2b$ (the conductances are neglected) will be modeled by the equivalent circuit shown in Figure B.1.

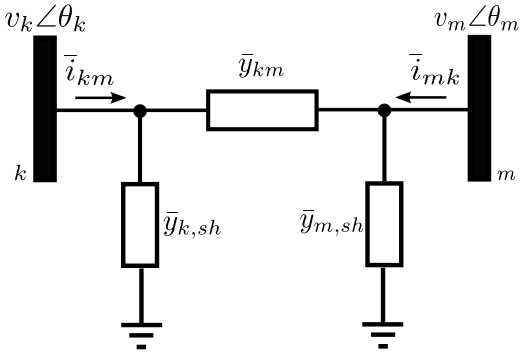


FIGURE B.1: Transmission line two-port $\pi$ model

The complex power injected in nodes $k$ and $m$ are:

$$\bar{s}_k = \bar{v}_k \bar{i}_k^* \tag{B.1}$$
$$\bar{s}_m = \bar{v}_m \bar{i}_m^*. \tag{B.2}$$

According to the model of transmission line shown in Figure B.1, the complex injected currents can be written as:

$$\begin{bmatrix} \bar{i}_k \\ \bar{i}_m \end{bmatrix} = \begin{bmatrix} \bar{y}_{km} + \bar{y}_{k,sh} & -\bar{y}_{km} \\ -\bar{y}_{km} & \bar{y}_{km} + \bar{y}_{m,sh} \end{bmatrix} \begin{bmatrix} \bar{v}_k \\ \bar{v}_k \end{bmatrix} \tag{B.3}$$

where

$$\bar{y}_{km} = g_{km} + jb_{km} = (r + jx)^{-1} \tag{B.4}$$
$$\bar{y}_{k,sh} = g_{k,sh} + jb_{k,sh} \tag{B.5}$$
$$\bar{y}_{m,sh} = g_{m,sh} + jb_{m,sh}. \tag{B.6}$$

The complex current flow from $k$ to $m$ is given by:

$$\bar{i}_{km} = v_k \bar{y}_{k,sh} + (\bar{v}_k - \bar{v}_m)\bar{y}_{km} = \bar{v}_k(\bar{y}_{km} + \bar{y}_{k,sh}) - \bar{v}_m \bar{y}_{km}. \tag{B.7}$$

Then the rectangular components of the phasor associated with the branch current flowing from node $k$ to node $m$ can be derived as:

$$\begin{aligned} i_{km,\Re} &= v_k((g_{km} + g_{k,sh})\cos(\theta_k) - (b_{km} + b_{k,sh})\sin(\theta_k)) \\ &- v_m(g_{km}\cos(\theta_m) - b_{km}\sin(\theta_m)) \end{aligned} \tag{B.8}$$
$$\begin{aligned} i_{km,\Im} &= v_k((g_{km} + g_{k,sh})\sin(\theta_k) + (b_{km} + b_{k,sh})\cos(\theta_k)) \\ &- v_m(g_{km}\sin(\theta_m) + b_{km}\cos(\theta_m)). \end{aligned} \tag{B.9}$$

Power flow equations:

$$p_{km} = v_k^2(g_{km} + g_{k,sh}) - v_k v_m(g_{km}\cos(\theta_k - \theta_m) + b_{km}\sin(\theta_k - \theta_m)) \tag{B.10}$$
$$q_{km} = -v_m^2(b_{km} + g_{b,sh}) - v_k v_m(g_{km}\sin(\theta_k - \theta_m) - b_{km}\cos(\theta_k - \theta_m)). \tag{B.11}$$

Lastly, the Jacobian elements of the estimated current and power flows to be included in the Jacobian matrix $\boldsymbol{H}$ are obtained:

Partial derivatives of current flows:

$$\frac{\partial I_{km,r}}{\partial \theta_k} = -V_k(G_{kk}\sin(\theta_k) - B_{kk}\cos(\theta_k)) \quad \text{(B.12)}$$

$$\frac{\partial I_{km,r}}{\partial \theta_m} = -V_m(G_{km}\sin(\theta_m) + B_{km}\cos(\theta_m)) \quad \text{(B.13)}$$

$$V_k\frac{\partial I_{km,r}}{\partial V_k} = V_k(G_{kk}\cos(\theta_k) - B_{kk}\sin(\theta_k)) \quad \text{(B.14)}$$

$$V_m\frac{\partial I_{km,r}}{\partial V_m} = V_m(G_{km}\cos(\theta_m) - B_{km}\sin(\theta_m)) \quad \text{(B.15)}$$

$$\frac{\partial I_{km,i}}{\partial \theta_k} = V_k(G_{kk}\cos(\theta_k) - B_{kk}\sin(\theta_k)) \quad \text{(B.16)}$$

$$\frac{\partial I_{km,i}}{\partial \theta_m} = V_m(G_{km}\cos(\theta_m) - B_{km}\sin(\theta_m)) \quad \text{(B.17)}$$

$$V_k\frac{\partial I_{km,i}}{\partial V_k} = V_k(G_{kk}\sin(\theta_k) + B_{kk}\cos(\theta_k)) \quad \text{(B.18)}$$

$$V_m\frac{\partial I_{km,i}}{\partial V_m} = V_m(G_{km}\sin(\theta_m) + B_{km}\cos(\theta_m)). \quad \text{(B.19)}$$

Partial derivatives of power flows:

$$\frac{\partial P_{km}}{\partial \theta_k} = V_kV_m[-G_{km}\sin(\theta_k - \theta_m) + B_{km}\cos(\theta_k - \theta_m)] \quad \text{(B.20)}$$

$$\frac{\partial P_{km}}{\partial \theta_m} = V_kV_m[G_{km}\sin(\theta_k - \theta_m) - B_{km}\cos(\theta_k - \theta_m)] \quad \text{(B.21)}$$

$$V_k\frac{\partial P_{km}}{\partial V_k} = 2V_k^2G_{kk} + V_kV_m[G_{km}\cos(\theta_k - \theta_m) + B_{km}\sin(\theta_k - \theta_m)] \quad \text{(B.22)}$$

$$V_m\frac{\partial P_{km}}{\partial V_m} = V_kV_m[G_{km}\cos(\theta_k - \theta_m) + B_{km}\sin(\theta_k - \theta_m)] \quad \text{(B.23)}$$

$$\frac{\partial Q_{km}}{\partial \theta_k} = V_kV_m[G_{km}\cos(\theta_k - \theta_m) + B_{km}\sin(\theta_k - \theta_m)] \quad \text{(B.24)}$$

$$\frac{\partial Q_{km}}{\partial \theta_m} = V_kV_m[-G_{km}\cos(\theta_k - \theta_m) - B_{km}\sin(\theta_k - \theta_m)] \quad \text{(B.25)}$$

$$V_k\frac{\partial Q_{km}}{\partial V_k} = -2V_k^2B_{kk} + V_kV_m[G_{km}\sin(\theta_k - \theta_m) - B_{km}\cos(\theta_k - \theta_m)] \quad \text{(B.26)}$$

$$V_m\frac{\partial Q_{km}}{\partial V_m} = V_kV_m[G_{km}\sin(\theta_k - \theta_m) - B_{km}\cos(\theta_k - \theta_m)]. \quad \text{(B.27)}$$

### B.1.2 Two winding transformer

The two winding transformer model is based on the physical representation of the transformer shown in Figure B.2(a) while the schematic equivalent circuit of the transformer is shown in Fig. B.2(b). It is a single phase transformer model with complex taps on both primary and secondary windings. The magnetizing branch of the transformer, which under saturated conditions becomes non-linear, is included to account for the core losses [71].

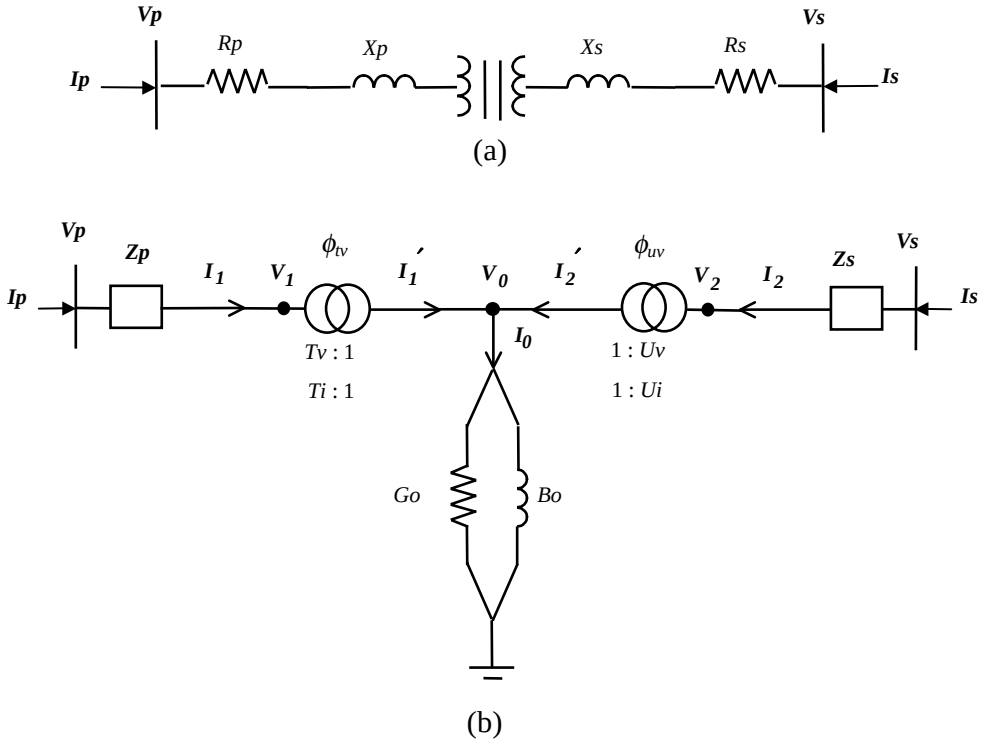


FIGURE B.2: Two winding transformer

The complex injected currents can be written as:

$$\begin{bmatrix} I_p \\ I_s \end{bmatrix} = \left[ \begin{bmatrix} G_{pp} & G_{ps} \\ G_{sp} & G_{ss} \end{bmatrix} + j \begin{bmatrix} B_{pp} & B_{ps} \\ B_{sp} & B_{ss} \end{bmatrix} \right] \begin{bmatrix} V_p \\ V_s \end{bmatrix} \tag{B.28}$$

where

$$G_{pp} = \frac{F_1(U_v^2 + R_1) + F_2 R_2}{A_2} \tag{B.29}$$

$$B_{pp} = \frac{F_1 R_2 - F_2(U_v^2 + R_1)}{A_2} \tag{B.30}$$

$$G_{ss} = \frac{F_1(T_v^2 + R_3) + F_2 R_4}{A_2} \tag{B.31}$$

$$B_{ss} = \frac{F_1 R_4 - F_2(T_v^2 + R_3)}{A_2} \tag{B.32}$$

$$G_{ps} = \frac{-T_v U_v(F_1 \cos(\phi_1) + F_2 \sin(\phi_1))}{A_2} \tag{B.33}$$

$$B_{ps} = \frac{T_v U_v(F_2 \cos(\phi_1) - F_1 \sin(\phi_1))}{A_2} \tag{B.34}$$

$$G_{sp} = \frac{-T_v U_v(F_1 \cos(\phi_2) + F_2 \sin(\phi_2))}{A_2} \tag{B.35}$$

$$B_{sp} = \frac{T_v U_v(F_2 \cos(\phi_2) - F_1 \sin(\phi_2))}{A_2} \tag{B.36}$$

$$F_1 = T_v^2 R_s + U_v^2 R_p + R_{eq} \tag{B.37}$$

$$F_2 = T_v^2 X_s + U_v^2 X_p + X_{eq} \tag{B.38}$$

$$A_2 = F_1^2 + F_2^2 \tag{B.39}$$

$$R_{eq} = (R_p R_s - X_p X_s) G_0 - (R_p X_s - R_s X_p) B_0 \tag{B.40}$$

$$X_{eq} = (R_p R_s - X_p X_s) B_0 + (R_p X_s - R_s X_p) G_0 \tag{B.41}$$

$$R_1 = R_s G_0 - X_s B_0 \tag{B.42}$$

$$R_2 = R_s B_0 + X_s G_0 \tag{B.43}$$

$$R_3 = R_p G_0 - X_p B_0 \tag{B.44}$$

$$R_4 = R_p B_0 + X_p G_0 \tag{B.45}$$

$$\phi_1 = \phi_{tv} - \phi_{uv} \tag{B.46}$$

$$\phi_2 = \phi_{uv} - \phi_{tv}. \tag{B.47}$$

Then the rectangular components of current flows can be derived as:

$$\begin{aligned} I_{ps,\Re} &= V_p(G_{pp} \cos(\theta_p) - B_{pp} \sin(\theta_p)) \\ &+ V_s(G_{ps} \cos(\theta_s) - B_{ps} \sin(\theta_s)) \end{aligned} \tag{B.48}$$

$$\begin{aligned} I_{ps,\Im} &= V_p(G_{pp} \sin(\theta_p) + B_{pp} \cos(\theta_p)) \\ &+ V_s(G_{ps} \sin(\theta_s) + B_{ps} \cos(\theta_s)) \end{aligned} \tag{B.49}$$

$$
\begin{aligned}
I_{sp,\Re} &= V_s(G_{ss}\cos(\theta_s) - B_{ss}\sin(\theta_s)) \\
&+ V_p(G_{sp}\cos(\theta_p) - B_{sp}\sin(\theta_p)) \qquad \text{(B.50)} \\
I_{sp,\Im} &= V_s(G_{ss}\sin(\theta_s) + B_{ss}\cos(\theta_s)) \\
&+ V_p(G_{sp}\sin(\theta_p) + B_{sp}\cos(\theta_p)). \qquad \text{(B.51)}
\end{aligned}
$$

The partial derivatives of rectangular components of current flows equations from $p$ to $s$ with respect to voltage phase and magnitude are:

$$
\begin{aligned}
\frac{\partial I_{ps,\Re}}{\partial \theta_p} &= -V_p[G_{pp}sin(\theta_p) + B_{pp}cos(\theta_p)] \qquad \text{(B.52)} \\
\frac{\partial I_{ps,\Re}}{\partial \theta_s} &= -V_s[G_{ps}sin(\theta_s) + B_{ps}cos(\theta_s)] \qquad \text{(B.53)} \\
\frac{\partial I_{ps,\Re}}{\partial V_p} &= G_p cos(\theta_p) - B_p sin(\theta_p) \qquad \text{(B.54)} \\
\frac{\partial I_{ps,\Re}}{\partial V_s} &= G_{ps}cos(\theta_s) - B_{ps}sin(\theta_s) \qquad \text{(B.55)}
\end{aligned}
$$

$$
\begin{aligned}
\frac{\partial I_{ps,\Im}}{\partial \theta_p} &= V_p[G_{pp}cos(\theta_p) - B_{pp}sin(\theta_p)] \qquad \text{(B.56)} \\
\frac{\partial I_{ps,\Im}}{\partial \theta_s} &= V_s[G_{ps}cos(\theta_s) - B_{ps}sin(\theta_s)] \qquad \text{(B.57)} \\
\frac{\partial I_{ps,\Im}}{\partial V_p} &= G_{pp}sin(\theta_p) + B_{pp}cos(\theta_p) \qquad \text{(B.58)} \\
\frac{\partial I_{ps,\Im}}{\partial V_s} &= G_{ps}sin(\theta_s) + B_{ps}cos(\theta_s). \qquad \text{(B.59)}
\end{aligned}
$$

The partial derivatives rectangular components of current flows equations from $s$ to $p$ with respect to voltage phase and magnitude are:

$$
\begin{aligned}
\frac{\partial I_{sp,\Re}}{\partial \theta_p} &= V_p[-G_{sp}sin(\theta_p) - B_{sp}cos(\theta_p)] \qquad \text{(B.60)} \\
\frac{\partial I_{sp,\Re}}{\partial \theta_s} &= V_s[G_{ss}sin(\theta_s) - B_{ss}cos(\theta_s)] \qquad \text{(B.61)} \\
\frac{\partial I_{sp,\Re}}{\partial V_p} &= G_{sp}cos(\theta_p) - B_{sp}sin(\theta_p) \qquad \text{(B.62)} \\
\frac{\partial I_{sp,\Re}}{\partial V_s} &= G_{ss}cos(\theta_s) - B_{ss}sin(\theta_s) \qquad \text{(B.63)}
\end{aligned}
$$

$$\frac{\partial I_{sp,\Im}}{\partial \theta_p} = V_p[G_{sp}cos(\theta_p) - B_{sp}sin(\theta_p)] \quad \text{(B.64)}$$

$$\frac{\partial I_{sp,\Im}}{\partial \theta_s} = V_s[G_{ss}cos(\theta_s) - B_{ss}sin(\theta_s)] \quad \text{(B.65)}$$

$$\frac{\partial I_{sp,\Im}}{\partial V_p} = G_{sp}sin(\theta_p) + B_{sp}cos(\theta_p) \quad \text{(B.66)}$$

$$\frac{\partial I_{sp,\Im}}{\partial V_s} = G_{ss}sin(\theta_s) + B_{ss}cos(\theta_s). \quad \text{(B.67)}$$

On the other hand, the power flow equations are computed as:

$$P_{ps} = V_p^2 G_{pp} + V_p V_s[G_{ps}cos(\theta_p - \theta_s) + B_{ps}sin(\theta_p - \theta_s)] \quad \text{(B.68)}$$

$$Q_{ps} = -V_p^2 B_{pp} + V_p V_s[G_{ps}sin(\theta_p - \theta_s) - B_{ps}cos(\theta_p - \theta_s)] \quad \text{(B.69)}$$

$$P_{sp} = V_s^2 G_{ss} + V_s V_p[G_{sp}cos(\theta_s - \theta_p) + B_{sp}sin(\theta_s - \theta_p)] \quad \text{(B.70)}$$

$$Q_{sp} = -V_s^2 B_{ss} + V_s V_p[G_{sp}sin(\theta_s - \theta_p) - B_{sp}cos(\theta_s - \theta_p)]. \quad \text{(B.71)}$$

The partial derivatives of power equations from $p$ to $s$ with respect to voltage phase and magnitude are:

$$\frac{\partial P_{ps}}{\partial \theta_p} = V_p V_s[-G_{ps}sin(\theta_p - \theta_s) + B_{ps}cos(\theta_p - \theta_s)] \quad \text{(B.72)}$$

$$\frac{\partial P_{ps}}{\partial \theta_s} = V_p V_s[G_{ps}sin(\theta_p - \theta_s) - B_{ps}cos(\theta_p - \theta_s)] \quad \text{(B.73)}$$

$$\frac{\partial P_{ps}}{\partial V_p} = 2V_p G_{pp} + V_s[G_{ps}cos(\theta_p - \theta_s) + B_{ps}sin(\theta_p - \theta_s)] \quad \text{(B.74)}$$

$$\frac{\partial P_{ps}}{\partial V_s} = V_p[G_{ps}cos(\theta_p - \theta_s) + B_{ps}sin(\theta_p - \theta_s)] \quad \text{(B.75)}$$

$$\frac{\partial Q_{ps}}{\partial \theta_p} = V_p V_s[G_{ps}cos(\theta_p - \theta_s) + B_{ps}sin(\theta_p - \theta_s)] \quad \text{(B.76)}$$

$$\frac{\partial Q_{ps}}{\partial \theta_s} = V_p V_s[-G_{ps}cos(\theta_p - \theta_s) - B_{ps}sin(\theta_p - \theta_s)] \quad \text{(B.77)}$$

$$\frac{\partial Q_{ps}}{\partial V_p} = -2V_p B_{pp} + V_s[G_{ps}sin(\theta_p - \theta_s) - B_{ps}cos(\theta_p - \theta_s)] \quad \text{(B.78)}$$

$$\frac{\partial Q_{ps}}{\partial V_s} = V_p[G_{ps}sin(\theta_p - \theta_s) - B_{ps}cos(\theta_p - \theta_s)]. \quad \text{(B.79)}$$

The partial derivatives power equations from $s$ to $p$ with respect to voltage phase and magnitude are:

$$\frac{\partial P_{sp}}{\partial \theta_p} = -V_s V_p[G_{sp} sin(\theta_s - \theta_p) - B_{sp} cos(\theta_s - \theta_p)] \quad \text{(B.80)}$$

$$\frac{\partial P_{sp}}{\partial \theta_s} = V_s V_p[-G_{sp} sin(\theta_s - \theta_p) + B_{sp} cos(\theta_s - \theta_p)] \quad \text{(B.81)}$$

$$\frac{\partial P_{sp}}{\partial V_p} = V_s[G_{sp} cos(\theta_s - \theta_p) + B_{sp} sin(\theta_s - \theta_p)] \quad \text{(B.82)}$$

$$\frac{\partial P_{sp}}{\partial V_p} = 2V_s G_{ss} + V_p[G_{sp} cos(\theta_s - \theta_p) + B_{sp} sin(\theta_s - \theta_p)] \quad \text{(B.83)}$$

$$\frac{\partial P_{sp}}{\partial \theta_p} = V_s V_p[-G_{sp} cos(\theta_s - \theta_p) - B_{sp} sin(\theta_s - \theta_p)] \quad \text{(B.84)}$$

$$\frac{\partial P_{sp}}{\partial \theta_s} = V_s V_p[G_{sp} cos(\theta_s - \theta_p) + B_{sp} sin(\theta_s - \theta_p)] \quad \text{(B.85)}$$

$$\frac{\partial P_{sp}}{\partial V_p} = V_s[G_{sp} sin(\theta_s - \theta_p) - B_{sp} cos(\theta_s - \theta_p)] \quad \text{(B.86)}$$

$$\frac{\partial P_{sp}}{\partial V_s} = -2V_s B_{ss} + V_p[G_{sp} sin(\theta_s - \theta_p) - B_{sp} cos(\theta_s - \theta_p)]. \quad \text{(B.87)}$$

### B.1.3 Phase shifting transformer

It is derived as a special case of a two-winding, shown in Figure B.2.

The partial derivatives of power and current equations with respect to the phase shifter angle in primary winding of the transformer are:

$$\frac{\partial P_{ps}}{\partial \phi_{tv}} = V_p V_s[G_{ps} sin(\theta_p - \theta_s) - B_{ps} cos(\theta_p - \theta_s)] \quad \text{(B.88)}$$

$$\frac{\partial P_{sp}}{\partial \phi_{tv}} = -V_s V_p[G_{sp} sin(\theta_s - \theta_p) - B_{sp} cos(\theta_s - \theta_p)] \quad \text{(B.89)}$$

$$\frac{\partial Q_{ps}}{\partial \phi_{tv}} = -V_p V_s[G_{ps} cos(\theta_p - \theta_s) + B_{ps} sin(\theta_p - \theta_s)] \quad \text{(B.90)}$$

$$\frac{\partial Q_{sp}}{\partial \phi_{tv}} = V_s V_p[G_{sp} cos(\theta_s - \theta_p) + B_{sp} sin(\theta_s - \theta_p)] \quad \text{(B.91)}$$

$$\frac{\partial I_{ps,\Re}}{\partial \phi_{tv}} = V_s[-G_{ps}sin(\theta_s) - B_{ps}cos(\theta_s)] \quad \text{(B.92)}$$
$$\frac{\partial I_{sp,\Re}}{\partial \phi_{tv}} = V_p[G_{sp}sin(\theta_p) + B_{sp}cos(\theta_p)] \quad \text{(B.93)}$$
$$\frac{\partial I_{ps,\Im}}{\partial \phi_{tv}} = V_s[G_{ps}cos(\theta_s) - B_{ps}sin(\theta_s)] \quad \text{(B.94)}$$
$$\frac{\partial I_{sp,\Im}}{\partial \phi_{tv}} = V_p[-G_{sp}cos(\theta_p) + B_{sp}sin(\theta_p)]. \quad \text{(B.95)}$$

The partial derivatives power and current equations with respect to the phase shifter angle in secondary winding of the transformer are:

$$\frac{\partial P_{ps}}{\partial \phi_{uv}} = -V_pV_s[G_{ps}sin(\theta_p - \theta_s) + B_{ps}cos(\theta_p - \theta_s)] \quad \text{(B.96)}$$
$$\frac{\partial P_{sp}}{\partial \phi_{uv}} = V_sV_p[G_{sp}sin(\theta_s - \theta_p) + B_{sp}cos(\theta_s - \theta_p)] \quad \text{(B.97)}$$
$$\frac{\partial Q_{ps}}{\partial \phi_{uv}} = V_pV_s[G_{ps}cos(\theta_p - \theta_s) - B_{ps}sin(\theta_p - \theta_s)] \quad \text{(B.98)}$$
$$\frac{\partial Q_{sp}}{\partial \phi_{uv}} = -V_sV_p[G_{sp}cos(\theta_s - \theta_p) - B_{sp}sin(\theta_s - \theta_p)] \quad \text{(B.99)}$$

$$\frac{\partial I_{ps,\Re}}{\partial \phi_{uv}} = V_s[G_{ps}sin(\theta_s) + B_{ps}cos(\theta_s)] \quad \text{(B.100)}$$
$$\frac{\partial I_{sp,\Re}}{\partial \phi_{uv}} = V_p[-G_{sp}sin(\theta_p) - B_{sp}cos(\theta_p)] \quad \text{(B.101)}$$
$$\frac{\partial I_{ps,\Im}}{\partial \phi_{uv}} = V_s[-G_{ps}cos(\theta_s) + B_{ps}sin(\theta_s)] \quad \text{(B.102)}$$
$$\frac{\partial I_{sp,\Im}}{\partial \phi_{uv}} = V_p[G_{sp}cos(\theta_p) - B_{sp}sin(\theta_p)]. \quad \text{(B.103)}$$

The vector of incremental changes in phase angle is given by,

$$\Delta\phi = \phi^{i+1} - \phi^i \quad \text{(B.104)}$$

after each iteration $i$ the phase shifter controller must be updated according to

$$\phi^{i+1} = \phi^i + \Delta\phi^i. \quad \text{(B.105)}$$

### B.1.4 Load tap changer

It is derived as a special case of a two-winding, shown in Figure B.2.

The partial derivatives of the power and current equations with respect to the primary tap of the two winding transformer are:

$$\begin{aligned}
\frac{\partial P_{ps}}{\partial T_v}T_v &= \frac{2V_p^2T_v^2}{A_2}(R_s(U_v^2+R_1)+X_sR_2-2G_{pp}(R_sF_1+X_sF_2)) \\
&+ V_pV_s(G_{ps}\cos(\delta_1)+B_{ps}\sin(\delta_1))(1-\frac{4T_v^2}{A_2}(R_sF_1+X_sF_2)) \\
&+ \frac{2V_pV_sT_v^3U_v}{A_2}(X_s\sin(\delta_1-\phi_1)-R_s\cos(\delta_1-\phi_1)) \qquad \text{(B.106)} \\
\frac{\partial Q_{ps}}{\partial T_v}T_v &= \frac{2V_p^2T_v^2}{A_2}(2B_{pp}(R_sF_1+X_sF_2)-R_sR_2+X_s(U_v^2+R_1)) \\
&+ V_pV_s(G_{ps}\sin(\delta_1)-B_{ps}\cos(\delta_1))(1-\frac{4T_v^2}{A_2}(R_sF_1+X_sF_2)) \\
&- \frac{2V_pV_sT_v^3U_v}{A_2}(R_s\sin(\delta_1-\phi_1)+X_s\cos(\delta_1-\phi_1)) \qquad \text{(B.107)} \\
\frac{\partial P_{sp}}{\partial T_v}T_v &= \frac{2V_s^2T_v^2}{A_2}(R_s(T_v^2+R_3)+X_sR_4+F_1-2G_{ss}(R_sF_1+X_sF_2)) \\
&+ V_pV_s(G_{sp}\cos(\delta_2)+B_{sp}\sin(\delta_2))(1-\frac{4T_v^2}{A_2}(R_sF_1+X_sF_2)) \\
&+ \frac{2V_pV_sT_v^3U_v}{A_2}(X_s\sin(\delta_2-\phi_2)-R_s\cos(\delta_2-\phi_2)) \qquad \text{(B.108)} \\
\frac{\partial Q_{sp}}{\partial T_v}T_v &= \frac{2V_s^2T_v^2}{A_2}(2B_{ss}(R_sF_1+X_sF_2)-R_sR_4+X_s(T_v^2+R_3)+F_2) \\
&+ V_pV_s(G_{sp}\sin(\delta_2)-B_{sp}\cos(\delta_2))(1-\frac{4T_v^2}{A_2}(R_sF_1+X_sF_2)) \\
&- \frac{2V_pV_sT_v^3U_v}{A_2}(R_s\sin(\delta_2-\phi_2)+X_s\cos(\delta_2-\phi_2)) \qquad \text{(B.109)}
\end{aligned}$$

$$\begin{aligned}
\frac{\partial I_{ps,\Re}}{\partial T_v} &= V_p[(dG_{pp}cos(\theta_p)-dB_{pp}sin(\theta_p)) \\
&+ V_s(dG_{ps}cos(\theta_s)-dB_{ps}sin(\theta_s))] \qquad \text{(B.110)} \\
\frac{\partial I_{sp,\Re}}{\partial T_v} &= V_s[(dG_{ss}cos(\theta_s)-dB_{ss}sin(\theta_s)) \\
&+ V_p(dG_{sp}cos(\theta_p)-dB_{sp}sin(\theta_p))] \qquad \text{(B.111)}
\end{aligned}$$

$$\begin{aligned}
\frac{\partial I_{ps,\Im}}{\partial T_v} &= V_p[(dG_{pp}sin(\theta_p)+dB_{pp}cos(\theta_p)) \\
&+ V_s(dG_{ps}sin(\theta_s)+dB_{ps}cos(\theta_s))] \qquad \text{(B.112)} \\
\frac{\partial I_{ss,\Im}}{\partial T_v} &= V_s[(dG_{ss}sin(\theta_s)+dB_{ss}cos(\theta_s)) \\
&+ V_p(dG_{sp}sin(\theta_p)+dB_{sp}cos(\theta_p))] \qquad \text{(B.113)}
\end{aligned}$$

where

$$\begin{aligned}
dG_{pp} &= ((2T_v^2)/A2)(R_s(U_v^2 + R1) \\
&+ X_sR2 - 2G_{pp}(R_sF1 + X_sF2)) && \text{(B.114)} \\
dB_{pp} &= ((2T_v^2)/A2)((R_sR2 - X_s(U_v^2 + R1)) \\
&- 2B_{pp}(R_sF1 + X_sF2)) && \text{(B.115)} \\
dG_{ss} &= ((2T_v^2)/A2)((R_s(T_v^2 + R3) + X_sR4 + F1) \\
&- (2G_{ss})(R_sF1 + X_sF2)) && \text{(B.116)} \\
dB_{ss} &= ((2T_v^2)/A2)(R_sR4 - X_s(T_v^2 + R3) - F2 \\
&- 2B_{ss}(R_sF1 + X_sF2)) && \text{(B.117)} \\
dG_{ps} &= G_{ps} - ((2T_v^3U_v)/A2)(R_scos(\theta_{ps}) + X_ssin(\theta_{ps})) \\
&- ((4T_v^2G_{ps})/A2)(R_sF1 + X_sF2) && \text{(B.118)} \\
dB_{ps} &= B_{ps} + ((2T_v^3U_v)/A2)(X_scos(\theta_{ps}) - R_ssin(\theta_{ps})) \\
&- ((4T_v^2B_{ps})/A2)(R_sF1 + X_sF2) && \text{(B.119)} \\
dG_{sp} &= G_{sp} - ((2T_v^3U_v)/A2)(R_scos(\theta_{sp}) + X_ssin(\theta_{sp})) \\
&- ((4T_v^2G_{sp})/A2)(R_sF1 + X_sF2) && \text{(B.120)} \\
dB_{sp} &= B_{sp} + ((2T_v^3U_v)/A2)(X_scos(\theta_{sp}) - R_ssin(\theta_{sp})) \\
&- ((4T_v^2B_{sp})/A2)(R_sF1 + X_sF2). && \text{(B.121)}
\end{aligned}$$

The partial derivatives of the power equations with respect to the secondary tap of the two winding transformer are:

$$\begin{aligned}
\frac{\partial P_{ps}}{\partial U_v}U_v &= \frac{2V_p^2U_v^2}{A_2}(R_s(U_v^2 + R_1) + X_pR_2 + F_1 - 2G_{pp}(R_pF_1 + X_pF_2)) \\
&+ V_pV_s(G_{ps}\cos(\delta_1) + B_{ps}\sin(\delta_1))(1 - \frac{4U_v^2}{A_2}(R_pF_1 + X_pF_2)) \\
&+ \frac{2V_pV_sU_v^3T_v}{A_2}(X_p\sin(\delta_1 - \phi_1) - R_p\cos(\delta_1 - \phi_1)) && \text{(B.122)} \\
\frac{\partial Q_{ps}}{\partial U_v}U_v &= \frac{2V_p^2U_v^2}{A_2}(2B_{pp}(R_pF_1 + X_pF_2) - R_pR_2 + X_p(U_v^2 + R_1) + F_2) \\
&+ V_pV_s(G_{ps}\sin(\delta_1) - B_{ps}\cos(\delta_1))(1 - \frac{4U_v^2}{A_2}(R_pF_1 + X_pF_2)) \\
&- \frac{2V_pV_sU_v^3T_v}{A_2}(R_p\sin(\delta_1 - \phi_1) + X_p\cos(\delta_1 - \phi_1)) && \text{(B.123)}
\end{aligned}$$

$$\begin{aligned}
\frac{\partial P_{sp}}{\partial U_v}U_v &= \frac{2V_s^2U_v^2}{A_2}(R_p(T_v^2+R_3)+X_pR_4-2G_{ss}(R_pF_1+X_pF_2)) \\
&+ V_sV_p(G_{sp}\cos(\delta_2)+B_{sp}\sin(\delta_2))(1-\frac{4U_v^2}{A_2}(R_pF_1+X_pF_2)) \\
&+ \frac{2V_sV_pU_v^3T_v}{A_2}(X_p\sin(\delta_2-\phi_2)-R_p\cos(\delta_2-\phi_2)) \qquad \text{(B.124)} \\
\frac{\partial Q_{sp}}{\partial U_v}U_v &= \frac{2V_s^2U_v^2}{A_2}(2B_{ss}(R_pF_1+X_pF_2)-R_pR_4+X_p(T_v^2+R_3)) \\
&+ V_pV_s(G_{ps}\sin(\delta_1)-B_{ps}\cos(\delta_1))(1-\frac{4U_v^2}{A_2}(R_pF_1+X_pF_2)) \\
&- \frac{2V_pV_sU_v^3T_v}{A_2}(R_p\sin(\delta_1-\phi_1)+X_p\cos(\delta_1-\phi_1)) \qquad \text{(B.125)}
\end{aligned}$$

where

$$\delta_1 = \theta_p - \theta_s \qquad \text{(B.126)}$$

$$\delta_2 = \theta_s - \theta_p \qquad \text{(B.127)}$$

after each iteration $i$ the tap must be updated according to,

$$T_k^{i+1} = T_k^i + \left(\frac{\Delta T_k}{T_k}\right)^i T_k^i. \qquad \text{(B.128)}$$

## B.1.5 Flexible AC Transmission Systems

### B.1.5.1 Static var compensator

The SVC model including the explicit representation of the stepdown transformer is shown in Fig. B.3 [83], both components are combined to form a single model, which is a more accurate representation without affecting the convergence characteristics of the proposed approach. The SVC variable susceptance is a function of the thyristor's firing angle $\alpha_{SVC}$ whose value is adjusted in order to satisfy the measurements provided by SCADA and PMU systems: active and reactive power flows, real and imaginary current flows and voltage magnitude.

The total admittance $\bar{Y}_{T-SVC}$ of the combined SVC-transformer set is given by:

$$Y_{T-SVC} = G_{T-SVC} + jB_{T-SVC} \qquad \text{(B.129)}$$

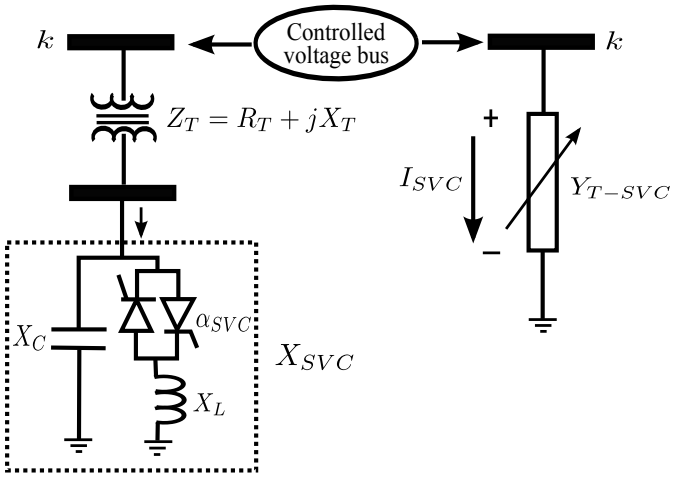


FIGURE B.3: Static Var Compensator

where

$$G_{T-SVC} = \frac{R_T}{R_T^2 + X_{Eq}^2} \tag{B.130}$$

$$B_{T-SVC} = -\frac{X_{Eq}}{R_T^2 + X_{Eq}^2} \tag{B.131}$$

$$X_{Eq} = X_T + X_{SVC} \tag{B.132}$$

$$X_{SVC} = \frac{X_C X_{TCR}}{X_C - X_{TCR}} \tag{B.133}$$

$$X_{TCR} = \frac{\pi X_L}{2(\pi - \alpha_{SVC}) + \sin(2\alpha_{SVC})}. \tag{B.134}$$

The real and imaginary terms of complex current flowing through the SVC controller are given by

$$I_{k,\Re} = V_k G_{T-SVC} \tag{B.135}$$

$$I_{k,\Im} = V_k B_{T-SVC}. \tag{B.136}$$

While the active and reactive power flow equations injected at node $k$ by the single model are

$$P_{T-SVC} = V_k^2 G_{T-SVC} \tag{B.137}$$

$$Q_{T-SVC} = -V_k^2 B_{T-SVC}. \tag{B.138}$$

where the Jacobian elements of estimated current and power measurements with respect to $\alpha_{SVC}$ are given by:

$$\frac{\partial I_{k,\Re}}{\partial \alpha_{SVC}} = V_k \left( \frac{R_T}{D^2} \frac{\partial D}{\partial \alpha_{SVC}} \right) \tag{B.139}$$

$$\frac{\partial I_{k,\Im}}{\partial \alpha_{SVC}} = V_k \left( \frac{1}{D^2} \right) \left( -D \frac{\partial X_{SVC}}{\partial \alpha_{SVC}} + X_{Eq} \frac{\partial D}{\partial \alpha_{SVC}} \right) \tag{B.140}$$

$$\frac{\partial P_{T-SVC}}{\partial \alpha_{SVC}} = V_k^2 \frac{\partial G_{T-SVC}}{\partial \alpha_{SVC}} \tag{B.141}$$

$$\frac{\partial Q_{T-SVC}}{\partial \alpha_{SVC}} = -V_k^2 \frac{\partial B_{T-SVC}}{\partial \alpha_{SVC}} \tag{B.142}$$

where

$$\frac{\partial G_{T-SVC}}{\partial \alpha_{SVC}} = -\frac{R_T}{D^2} \frac{\partial D}{\partial \alpha_{SVC}} \tag{B.143}$$

$$\frac{\partial B_{T-SVC}}{\partial \alpha_{SVC}} = \frac{1}{D^2} \left( -D \frac{\partial X_{SVC}}{\partial \alpha_{SVC}} + X_{Eq} \frac{\partial D}{\partial \alpha_{SVC}} \right) \tag{B.144}$$

$$\frac{\partial D}{\partial \alpha_{SVC}} = 2 X_{Eq} \frac{\partial X_{SVC}}{\partial \alpha_{SVC}} \tag{B.145}$$

$$\frac{\partial X_{SVC}}{\partial \alpha_{SVC}} = \frac{2 X_{SVC}^2}{\pi X_L} \left( 1 - \cos(2\alpha_{SVC}) \right) \tag{B.146}$$

$$D = R_T^2 + X_{Eq}^2. \tag{B.147}$$

At the $i$-th iteration, the SVC's firing angle is updated by

$$\alpha_{SVC}^{i+1} = \alpha_{SVC}^{i} + \Delta \alpha_{SVC}^{i}. \tag{B.148}$$

#### B.1.5.2 Thyristor controlled series compensator

Figure B.4 shows the general configuration of a TCSC module with a fundamental frequency TCSC equivalent reactance given by B.152, as a function of the TCSC firing angle $\alpha_{TCSC}$ [83].

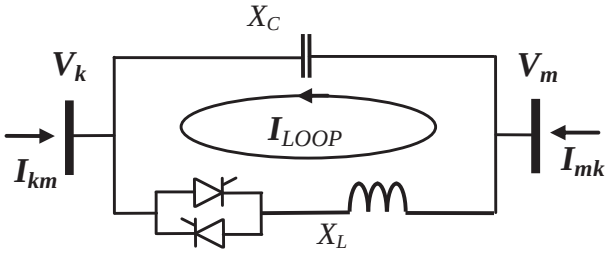


FIGURE B.4: Thyristor Controlled Series Compensator

$$\begin{bmatrix} I_k \\ I_m \end{bmatrix} = j \begin{bmatrix} B_{kk} & B_{km} \\ B_{mk} & B_{mm} \end{bmatrix} \begin{bmatrix} V_k \\ V_m \end{bmatrix} \tag{B.149}$$

where

$$B_{kk} = B_{mm} = B_{TCSC} = -\frac{1}{X_{TCSC}} \tag{B.150}$$

$$B_{km} = B_{mk} = -B_{TCSC} = \frac{1}{X_{TCSC}} \tag{B.151}$$

and

$$\begin{aligned} X_{TCSC} &= -X_c + (X_c + X_{LC}) \left( \frac{2(\pi - \alpha) + \sin(2(\pi - \alpha))}{\pi} \right) \\ &- \frac{4X_{LC}^2 \cos^2(\pi - \alpha)}{X_L} \left( \frac{k \, \tan(k(\pi - \alpha)) - \tan(\pi - \alpha)}{\pi} \right). \end{aligned} \tag{B.152}$$

The equation representing the branch current measurement in polar coordinates at the TCSC controller is derived from the equivalent circuit shown in Figure B.4 and is given by

$$I_{km,\Re} = -V_k B_{TCSC} \sin(\theta_k) + V_m B_{TCSC} \sin(\theta_m) \tag{B.153}$$

$$I_{km,\Im} = V_k B_{TCSC} \cos(\theta_k) - V_m B_{TCSC} \cos(\theta_m). \tag{B.154}$$

The active and reactive power flowing through the controller from its terminal $k$ to $m$ are given by

$$P_{km} = V_k V_m B_{TCSC} \sin(\theta_k - \theta_m) \tag{B.155}$$

$$Q_{km} = -V_k^2 B_{TCSC} - V_k V_m B_{TCSC} \cos(\theta_k - \theta_m). \tag{B.156}$$

The TCSC linearized current and power equations are given by

$$\frac{\partial I_{km,\Re}}{\partial \alpha_{TCSC}} = I_{km,\Re} B_{TCSC} \tag{B.157}$$

$$\frac{\partial I_{km,\Im}}{\partial \alpha_{TCSC}} = I_{km,\Im} B_{TCSC} \tag{B.158}$$

$$\frac{\partial P_{km}}{\partial \alpha_{TCSC}} = P_{km} B_{TCSC} \frac{\partial X_{TCSC}}{\partial \alpha_{TCSC}} \tag{B.159}$$

$$\frac{\partial Q_{km}}{\partial \alpha_{TCSC}} = Q_{km} B_{TCSC} \frac{\partial X_{TCSC}}{\partial \alpha_{TCSC}} \tag{B.160}$$

where

$$\begin{aligned} \frac{\partial X_{TCSC}}{\partial \alpha_{TCSC}} &= -2C_1(1+\cos(2\alpha_{TCSC})) \\ &+ C_2 \sin(2\alpha_{TCSC})(\varpi \tan(\varpi(\pi-\alpha_{TCSC})) - \tan\alpha_{TCSC}) \\ &+ C_2 \left( \varpi^2 \frac{\cos^2(\pi-\alpha_{TCSC})}{\cos^2(\varpi(\pi-\alpha_{TCSC}))} - 1 \right) \end{aligned} \tag{B.161}$$

$$C_1 = \frac{X_C + X_{LC}}{\pi} \tag{B.162}$$

$$C_2 = -\frac{4X_{LC}^2}{X_L \pi} \tag{B.163}$$

$$\varpi = \sqrt{\frac{X_C}{X_L}}. \tag{B.164}$$

At the $i$-th iteration, the incremental change of the estimated TCSC's firing angle is

$$\Delta \alpha_{TCSC}^i = \alpha_{TCSC}^{i+1} - \alpha_{TCSC}^i. \tag{B.165}$$

### B.1.5.3 Unified power flow compensator

The UPFC is a combination of a static synchronous shunt and series compensators, which are coupled together via a DC link to allow a bidirectional active power flow between the converters output terminals. The DC voltage on the common DC bus capacitor is converted into AC voltages at the converters terminals, so that the UPFC can be represented by two controllable AC voltage sources $V_{cR}$ and $V_{vR}$, as shown in Fig. B.5, whose magnitudes and phase angles can be adjusted to control, simultaneously or selectively, the active and reactive power flow in the compensated transmission line as well as the voltage magnitude at the network's node at which the shunt converter is connected. On the other hand, the source impedances $Z_{cR}$ and $Z_{vR}$ represent coupling transformers, whereas $V_k$ and $V_m$ are the complex voltages at nodes $k$ and $m$, respectively.

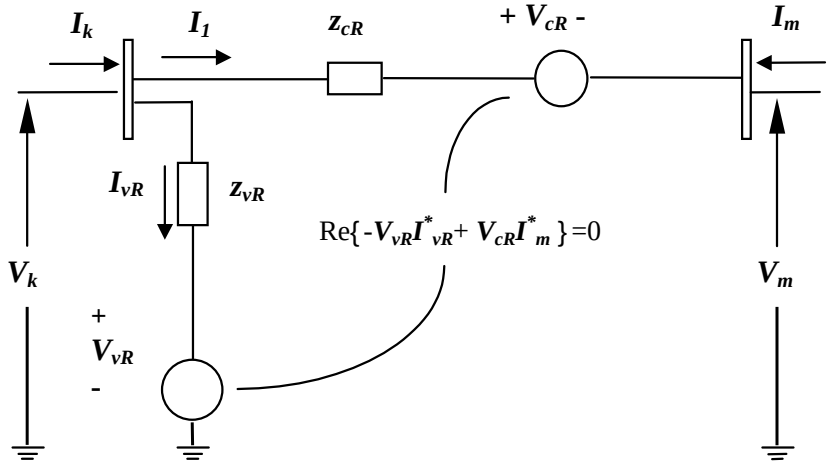


FIGURE B.5: Unified Power Flow Controller

The ideal voltages sources are:

$$\bar{V}_{vR} = V_{vR}(\cos\theta_{vR} + j\sin\theta_{vR}) \tag{B.166}$$

$$\bar{V}_{cR} = V_{cR}(\cos\theta_{cR} + j\sin\theta_{cR}) \tag{B.167}$$

where $V_{vR}$ and $\theta_{vR}$ (resp. $V_{cR}$ and $\theta_{cR}$) are the controllable magnitudes and angle of the ideal voltage source representing the shunt converter (resp. series converter).

The general admittance matrix:

$$\begin{bmatrix} I_k \\ I_m \end{bmatrix} = \begin{bmatrix} Y_{kk} & Y_{km} & Y_{km} & Y_{vR} \\ Y_{mk} & Y_{mm} & Y_{mm} & 0 \end{bmatrix} \begin{bmatrix} V_k \\ V_m \\ V_{cR} \\ V_{vR} \end{bmatrix} \tag{B.168}$$

where

$$y_{cR} = \frac{1}{z_{cR}} = \frac{1}{R_{cR} + jX_{cR}} \tag{B.169}$$

$$y_{vR} = \frac{1}{z_{vR}} = \frac{1}{R_{vR} + jX_{vR}} \tag{B.170}$$

$$Y_{kk} = y_{cR} + y_{vR} = G_{kk} + jB_{kk} \tag{B.171}$$

$$Y_{mm} = y_{cR} = G_{mm} + jB_{mm} \tag{B.172}$$

$$Y_{km} = Y_{mk} = -y_{cR} = G_{km} + jB_{km} \tag{B.173}$$

$$Y_{vR} = -y_{vR} = G_{vR} + jB_{vR}. \tag{B.174}$$

Based on the equivalent circuit shown in Fig. B.5 the active and reactive power equations are given by:

At node k:

$$\begin{aligned} I_{km,\Re} &= V_k(G_{kk}\cos(\theta_k) - B_{kk}\sin(\theta_k)) + V_m(G_{km}\cos(\theta_m) - B_{km}\sin(\theta_m)) \\ &+ V_{cR}(G_{km}\cos(\theta_{cR}) - B_{km}\sin(\theta_{cR})) \\ &+ V_{vR}(G_{vR}\cos(\theta_{vR}) - B_{vR}\sin(\theta_{vR})) \end{aligned} \tag{B.175}$$

$$\begin{aligned} I_{km,\Im} &= V_k(G_{kk}\sin(\theta_k) + B_{kk}\cos(\theta_k)) + V_m(G_{km}\sin(\theta_m) + B_{km}\cos(\theta_m)) \\ &+ V_{cR}(G_{km}\sin(\theta_{cR}) + B_{km}\cos(\theta_{cR})) \\ &+ V_{vR}(G_{vR}\sin(\theta_{vR}) + B_{vR}\cos(\theta_{vR})) \end{aligned} \tag{B.176}$$

$$\begin{aligned} P_{km} &= V_k^2 G_{kk} + V_k V_m(G_{km}\cos(\theta_k - \theta_m) + B_{km}\sin(\theta_k - \theta_m)) \\ &+ V_k V_{cR}(G_{km}\cos(\theta_k - \theta_{cR}) + B_{km}\sin(\theta_k - \theta_{cR})) \\ &+ V_k V_{vR}(G_{vR}\cos(\theta_k - \theta_{vR}) + B_{vR}\sin(\theta_k - \theta_{vR})) \end{aligned} \tag{B.177}$$

$$\begin{aligned} Q_{km} &= -V_k^2 B_{kk} + V_k V_m(G_{km}\sin(\theta_k - \theta_m) - B_{km}\cos(\theta_k - \theta_m)) \\ &+ V_k V_{cR}(G_{km}\sin(\theta_k - \theta_{cR}) - B_{km}\cos(\theta_k - \theta_{cR})) \\ &+ V_k V_{vR}(G_{vR}\sin(\theta_k - \theta_{vR}) - B_{vR}\cos(\theta_k - \theta_{vR})). \end{aligned} \tag{B.178}$$

At node m:

$$\begin{aligned} I_{mk,\Re} &= V_k(G_{mk}\cos(\theta_k) - B_{mk}\sin(\theta_k)) + V_m(G_{mm}\cos(\theta_m) - B_{mm}\sin(\theta_m)) \\ &+ V_{cR}(G_{mm}\cos(\theta_{cR}) - B_{mm}\sin(\theta_{cR})) \qquad \text{(B.179)} \\ I_{mk,\Im} &= V_k(G_{mk}\sin(\theta_k) + B_{mk}\cos(\theta_k)) + V_m(G_{mm}\sin(\theta_m) + B_{mm}\cos(\theta_m)) \\ &+ V_{cR}(G_{mm}\sin(\theta_{cR}) + B_{mm}\cos(\theta_{cR})) \qquad \text{(B.180)} \\ P_{mk} &= V_m^2 G_{mm} + V_m V_k(G_{mk}\cos(\theta_m - \theta_k) + B_{mk}\sin(\theta_m - \theta_k)) \\ &+ V_m V_{cR}(G_{mm}\cos(\theta_m - \theta_{cR}) + B_{mm}\sin(\theta_m - \theta_{cR})) \qquad \text{(B.181)} \\ Q_{mk} &= -V_m^2 B_{mm} + V_m V_k(G_{mk}\sin(\theta_m - \theta_k) - B_{mk}\cos(\theta_m - \theta_k)) \\ &+ V_m V_{cR}(G_{mm}\sin(\theta_m - \theta_{cR}) - B_{mm}\cos(\theta_m - \theta_{cR})). \qquad \text{(B.182)} \end{aligned}$$

Series converter:

$$\begin{aligned} P_{cR} &= V_{cR}^2 G_{mm} + V_{cR} V_k(G_{km}\cos(\theta_{cR} - \theta_k) + B_{km}\sin(\theta_{cR} - \theta_k)) \\ &+ V_{cR} V_m(G_{mm}\cos(\theta_{cR} - \theta_m) + B_{mm}\sin(\theta_{cR} - \theta_m)) \qquad \text{(B.183)} \\ Q_{cR} &= -V_{cR}^2 B_{mm} + V_{cR} V_k(G_{km}\sin(\theta_{cR} - \theta_k) - B_{km}\cos(\theta_{cR} - \theta_k)) \\ &+ V_{cR} V_m(G_{mm}\sin(\theta_{cR} - \theta_m) - B_{mm}\cos(\theta_{cR} - \theta_m)). \qquad \text{(B.184)} \end{aligned}$$

Shunt converter:

$$\begin{aligned} P_{vR} &= V_{vR}^2 G_{vR} + V_{vR} V_k(G_{vR}\cos(\theta_{vR} - \theta_k) + B_{vR}\sin(\theta_{vR} - \theta_k)) \qquad \text{(B.185)} \\ Q_{vR} &= -V_{vR}^2 B_{vR} + V_{vR} V_k(G_{vR}\sin(\theta_{vR} - \theta_k) - B_{vR}\cos(\theta_{vR} - \theta_k)) \qquad \text{(B.186)} \end{aligned}$$

Furthermore the active power supplied to the shunt converter, $P_{vR}$, must satisfy the active power demanded by series converter, $P_{cR}$, i.e.

$$P_{vR} + P_{cR} = 0. \qquad \text{(B.187)}$$

The jacobian terms at node k:

$$\begin{aligned} H_{km} &= \frac{\partial P_{km}}{\partial \theta_m} = V_k V_m(G_{km}\sin(\theta_k - \theta_m) - B_{km}\cos(\theta_k - \theta_m)) \qquad \text{(B.188)} \\ H_{kcR} &= \frac{\partial P_{km}}{\partial \theta_{cR}} = V_k V_{cR}(G_{km}\sin(\theta_k - \theta_{cR}) - B_{km}\cos(\theta_k - \theta_{cR})) \qquad \text{(B.189)} \\ H_{kvR} &= \frac{\partial P_{km}}{\partial \theta_{vR}} = V_k V_{vR}(G_{vR}\sin(\theta_k - \theta_{vR}) - B_{vR}\cos(\theta_k - \theta_{vR})) \qquad \text{(B.190)} \\ H_{kk} &= \frac{\partial P_{km}}{\partial \theta_k} = -H_{km} - H_{kcR} - H_{kvR} \qquad \text{(B.191)} \end{aligned}$$

$$N_{km} = \frac{\partial P_{km}}{\partial V_m} V_m = V_k V_m (G_{km} \cos(\theta_k - \theta_m) + B_{km} \sin(\theta_k - \theta_m)) \quad \text{(B.192)}$$

$$N_{kcR} = \frac{\partial P_{km}}{\partial V_{cR}} V_{cR} = V_k V_{cR} (G_{km} \cos(\theta_k - \theta_{cR}) + B_{km} \sin(\theta_k - \theta_{cR})) \quad \text{(B.193)}$$

$$N_{kvR} = \frac{\partial P_{km}}{\partial V_{vR}} V_{vR} = V_k V_{vR} (G_{vR} \cos(\theta_k - \theta_{vR}) + B_{vR} \sin(\theta_k - \theta_{vR})) \quad \text{(B.194)}$$

$$N_{kk} = \frac{\partial P_{km}}{\partial V_k} V_k = 2V_k^2 G_{kk} + N_{km} + N_{kcR} + N_{kvR} \quad \text{(B.195)}$$

$$J_{km} = \frac{\partial Q_{km}}{\partial \theta_m} = -N_{km} \quad \text{(B.196)}$$

$$J_{kcR} = \frac{\partial Q_{km}}{\partial \theta_{cR}} = -N_{kcR} \quad \text{(B.197)}$$

$$J_{kvR} = \frac{\partial Q_{km}}{\partial \theta_{vR}} = -N_{kvR} \quad \text{(B.198)}$$

$$J_{kk} = \frac{\partial Q_{km}}{\partial \theta_k} = N_{km} + N_{kcR} + N_{kvR} \quad \text{(B.199)}$$

$$L_{km} = \frac{\partial Q_{km}}{\partial V_m} V_m = H_{km} \quad \text{(B.200)}$$

$$L_{kcR} = \frac{\partial Q_{km}}{\partial V_{cR}} V_{cR} = H_{kcR} \quad \text{(B.201)}$$

$$L_{kvR} = \frac{\partial Q_{km}}{\partial V_{vR}} V_{vR} = H_{kvR} \quad \text{(B.202)}$$

$$L_{kk} = \frac{\partial Q_{km}}{\partial V_k} V_k = -2V_k^2 B_{kk} - H_{kk}. \quad \text{(B.203)}$$

The jacobian terms at node m:

$$H_{mk} = \frac{\partial P_{mk}}{\partial \theta_k} = V_m V_k (G_{mk} \sin(\theta_m - \theta_k) - B_{mk} \cos(\theta_m - \theta_k)) \quad \text{(B.204)}$$

$$H_{mcR} = \frac{\partial P_{mk}}{\partial \theta_{cR}} = V_m V_{cR} (G_{mm} \sin(\theta_m - \theta_{cR}) - B_{mm} \cos(\theta_m - \theta_{cR})) \quad \text{(B.205)}$$

$$H_{mm} = \frac{\partial P_{mk}}{\partial \theta_m} = -H_{mk} - H_{mcR} \quad \text{(B.206)}$$

$$N_{mk} = \frac{\partial P_{mk}}{\partial V_k} V_k = V_m V_k (G_{mk} \cos(\theta_m - \theta_k) + B_{mk} \sin(\theta_m - \theta_k)) \quad \text{(B.207)}$$

$$N_{mcR} = \frac{\partial P_{mk}}{\partial V_{cR}} V_{cR} = V_m V_{cR} (G_{mm} \cos(\theta_m - \theta_{cR}) + B_{mm} \sin(\theta_m - \theta_{cR})) \quad \text{(B.208)}$$

$$N_{mm} = \frac{\partial P_{mk}}{\partial V_m} V_m = 2V_m^2 G_{mm} + N_{mk} + N_{mcR} \quad \text{(B.209)}$$

$$J_{mk} = \frac{\partial Q_{mk}}{\partial \theta_k} = -N_{mk} \tag{B.210}$$

$$J_{mcR} = \frac{\partial Q_{mk}}{\partial \theta_{cR}} = -N_{mcR} \tag{B.211}$$

$$J_{mm} = \frac{\partial Q_{mk}}{\partial \theta_m} = N_{mk} + N_{mcR} \tag{B.212}$$

$$L_{mk} = \frac{\partial Q_{mk}}{\partial V_k} V_k = H_{mk} \tag{B.213}$$

$$L_{mcR} = \frac{\partial Q_{mk}}{\partial V_{cR}} V_{cR} = H_{mcR} \tag{B.214}$$

$$L_{mm} = \frac{\partial Q_{mk}}{\partial V_m} V_m = -2V_m^2 B_{mm} - H_{mm}. \tag{B.215}$$

The jacobian terms of series converter:

$$H_{cRk} = \frac{\partial P_{cR}}{\partial \theta_k} = V_{cR}V_k(G_{km}\sin(\theta_{cR} - \theta_k) - B_{km}\cos(\theta_{cR} - \theta_k)) \tag{B.216}$$

$$H_{cRm} = \frac{\partial P_{cR}}{\partial \theta_m} = V_{cR}V_m(G_{mm}\sin(\theta_{cR} - \theta_m) - B_{mm}\cos(\theta_{cR} - \theta_m)) \tag{B.217}$$

$$H_{cRcR} = \frac{\partial P_{cR}}{\partial \theta_{cR}} = -H_{cRk} - H_{cRm} \tag{B.218}$$

$$N_{cRk} = \frac{\partial P_{cR}}{\partial V_k} V_k = V_{cR}V_k(G_{km}\cos(\theta_{cR} - \theta_k) + B_{mk}\sin(\theta_{cR} - \theta_k)) \tag{B.219}$$

$$N_{cRm} = \frac{\partial P_{cR}}{\partial V_m} V_m = V_{cR}V_m(G_{mm}\cos(\theta_{cR} - \theta_m) + B_{mm}\sin(\theta_{cR} - \theta_m)) \tag{B.220}$$

$$N_{cRcR} = \frac{\partial P_{cR}}{\partial V_{cR}} V_{cR} = 2V_{cR}^2 G_{mm} + N_{cRk} + N_{cRm}. \tag{B.221}$$

The jacobian terms of shunt converter:

$$H_{vRk} = \frac{\partial P_{vR}}{\partial \theta_k} = V_{vR}V_k(G_{vR}\sin(\theta_{vR} - \theta_k) - B_{vR}\cos(\theta_{vR} - \theta_k)) \tag{B.222}$$

$$H_{vRcR} = \frac{\partial P_{vR}}{\partial \theta_{vR}} = -H_{vRk} \tag{B.223}$$

$$N_{vRk} = \frac{\partial P_{vR}}{\partial V_k} V_k = V_{vR}V_k(G_{vR}\cos(\theta_{vR} - \theta_k) + B_{vR}\sin(\theta_{vR} - \theta_k)) \tag{B.224}$$

$$N_{vRvR} = \frac{\partial P_{vR}}{\partial V_{vR}} V_{vR} = 2V_{vR}^2 G_{vR} + N_{vRk}. \tag{B.225}$$

The jacobian terms for current flows are given by:

$$\frac{\partial I_{km,\Re}}{\partial \theta_k} = -V_k(G_{kk}sin(\theta_k) + B_{kk}cos(\theta_k)) \quad \text{(B.226)}$$

$$\frac{\partial I_{km,\Re}}{\partial \theta_m} = -V_m(G_{km}sin(\theta_m) + B_{km}cos(\theta_m)) \quad \text{(B.227)}$$

$$\frac{\partial I_{km,\Re}}{\partial V_k} = G_{kk}cos(\theta_k) - B_{kk}sin(\theta_k) \quad \text{(B.228)}$$

$$\frac{\partial I_{km,\Re}}{\partial V_m} = G_{km}cos(\theta_m) - B_{km}sin(\theta_m) \quad \text{(B.229)}$$

$$\frac{\partial I_{km,\Re}}{\partial \theta_{cR}} = -V_{cr}(G_{km}sin(\theta_{cr}) + B_{km}cos(\theta_{cr})) \quad \text{(B.230)}$$

$$\frac{\partial I_{km,\Re}}{\partial V_{cR}} = G_{km}cos(\theta_{cr}) - B_{km}sin(\theta_{cr}) \quad \text{(B.231)}$$

$$\frac{\partial I_{km,\Re}}{\partial \theta_{vR}} = -V_{vr}(G_{vr}sin(\theta_{vr}) + B_{vr}cos(\theta_{vr})) \quad \text{(B.232)}$$

$$\frac{\partial I_{km,\Re}}{\partial V_{vR}} = G_{vr}cos(\theta_{vr}) - B_{vr}sin(\theta_{vr}) \quad \text{(B.233)}$$

$$\frac{\partial I_{mk,\Re}}{\partial \theta_k} = -V_k(G_{mk}sin(\theta_k) + B_{mk}cos(\theta_k)) \quad \text{(B.234)}$$

$$\frac{\partial I_{mk,\Re}}{\partial \theta_m} = -V_m(G_{mm}sin(\theta_m) + B_{mm}cos(\theta_m)) \quad \text{(B.235)}$$

$$\frac{\partial I_{mk,\Re}}{\partial V_k} = G_{mk}cos(\theta_k) - B_{mk}sin(\theta_k) \quad \text{(B.236)}$$

$$\frac{\partial I_{mk,\Re}}{\partial V_m} = G_{mm}cos(\theta_m) - B_{mm}sin(\theta_m) \quad \text{(B.237)}$$

$$\frac{\partial I_{mk,\Re}}{\partial \theta_{cR}} = -V_{cr}(G_{mm}sin(\theta_{cr}) + B_{mm}cos(\theta_{cr})) \quad \text{(B.238)}$$

$$\frac{\partial I_{mk,\Re}}{\partial V_{cR}} = G_{mm}cos(\theta_{cr}) - B_{mm}sin(\theta_{cr}) \quad \text{(B.239)}$$

$$\frac{\partial I_{mk,\Re}}{\partial \theta_{vR}} = 0 \quad \text{(B.240)}$$

$$\frac{\partial I_{mk,\Re}}{\partial V_{vR}} = 0 \quad \text{(B.241)}$$

$$\frac{\partial I_{km,\Im}}{\partial \theta_k} = V_k(G_{kk}cos(\theta_k) - B_{kk}sin(\theta_k)) \quad \text{(B.242)}$$

$$\frac{\partial I_{km,\Im}}{\partial \theta_m} = V_m(G_{km}cos(\theta_m) - B_{km}sin(\theta_m)) \quad \text{(B.243)}$$

$$\frac{\partial I_{km,\Im}}{\partial V_k} = G_{kk}sin(\theta_k) + B_{kk}cos(\theta_k) \quad \text{(B.244)}$$

$$\frac{\partial I_{km,\Im}}{\partial V_m} = G_{km}sin(\theta_m) + B_{km}cos(\theta_m) \quad \text{(B.245)}$$

$$\frac{\partial I_{km,\Im}}{\partial \theta_{cR}} = V_{cr}(G_{km}cos(\theta_{cr}) - B_{km}sin(\theta_{cr})) \quad \text{(B.246)}$$

$$\frac{\partial I_{km,\Im}}{\partial V_{cR}} = G_{km}sin(\theta_{cr}) + B_{km}cos(\theta_{cr}) \quad \text{(B.247)}$$

$$\frac{\partial I_{km,\Im}}{\partial \theta_{vR}} = V_{vr}(G_{vr}cos(\theta_{vr}) - B_{vr}sin(\theta_{vr})) \quad \text{(B.248)}$$

$$\frac{\partial I_{km,\Im}}{\partial V_{vR}} = G_{vr}sin(\theta_{vr}) + B_{vr}cos(\theta_{vr}) \quad \text{(B.249)}$$

(B.250)

$$\frac{\partial I_{mk,\Im}}{\partial \theta_k} = V_k(G_{mk}cos(\theta_k) - B_{mk}sin(\theta_k)) \quad \text{(B.251)}$$

$$\frac{\partial I_{mk,\Im}}{\partial \theta_m} = V_m(G_{mm}cos(\theta_m) - B_{mm}sin(\theta_m)) \quad \text{(B.252)}$$

$$\frac{\partial I_{mk,\Im}}{\partial V_k} = G_{mk}sin(\theta_k) + B_{mk}cos(\theta_k) \quad \text{(B.253)}$$

$$\frac{\partial I_{mk,\Im}}{\partial V_m} = G_{mm}sin(\theta_m) + B_{mm}cos(\theta_m) \quad \text{(B.254)}$$

$$\frac{\partial I_{mk,\Im}}{\partial \theta_{cR}} = V_{cr}(G_{mm}cos(\theta_{cr}) - B_{mm}sin(\theta_{cr})) \quad \text{(B.255)}$$

$$\frac{\partial I_{mk,\Im}}{\partial V_{cR}} = G_{mm}sin(\theta_{cr}) + B_{mm}cos(\theta_{cr}) \quad \text{(B.256)}$$

$$\frac{\partial I_{mk,\Im}}{\partial \theta_{vR}} = 0 \quad \text{(B.257)}$$

$$\frac{\partial I_{mk,\Im}}{\partial V_{vR}} = 0. \quad \text{(B.258)}$$

## B.1.6 Wind Generators

### B.1.6.1 Fixed speed wind generator

A FSWG is equipped with a squirrel cage induction generator that is directly connected to the grid and with fixed shunt capacitors for compensating the reactive power demanded by the generator. The active and reactive powers at the FSWG's terminals are mathematically derived from the steady state equivalent model of an induction machine shown in Fig. B.6, where the subscripts 1 and 2 represent stator and rotor variables, respectively, $m$ symbolizes the magnetization branch and $s$ is the slip of the induction generator.

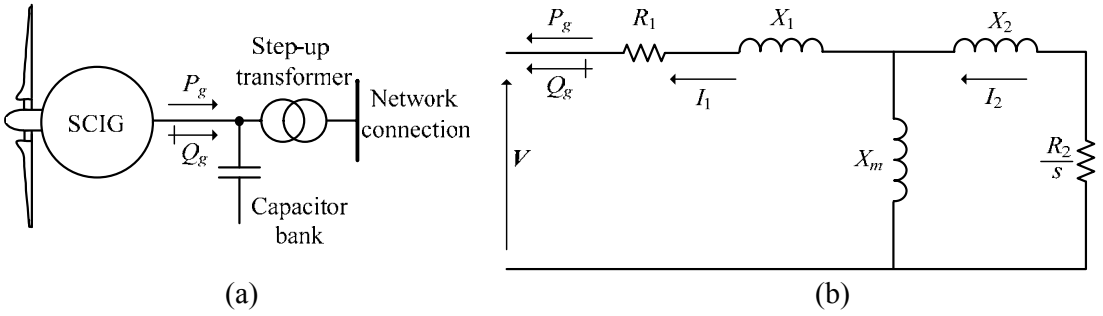


FIGURE B.6: Fixed speed wind generator: (a) schematic diagram (b) steady-state model

The FSWG's active and reactive powers are given by:

$$P_{k,FSWG}(V,s) = -V_k^2\left(\frac{K+Hs+Ls^2}{[C-Ds]^2+[E+Fs]^2}\right) \quad \text{(B.259)}$$

$$Q_{k,FSWG}(V,s) = -V_k^2\left(\frac{A+Bs^2}{[C-Ds]^2+[E+Fs]^2}\right). \quad \text{(B.260)}$$

On the other hand, the rectangular components of current phasor injected at node $k$ are given by:

$$I_{k,FSWG}(V,s) = V_k\left(\frac{(K+Hs+Ls^2)\cos\theta+(A+Bs^2)\sin\theta}{[C-Ds]^2+[E+Fs]^2}\right) \quad \text{(B.261)}$$

$$I_{k,FSWG}(V,s) = V_k\left(\frac{(K+Hs+Ls^2)\sin\theta-(A+Bs^2)\cos\theta}{[C-Ds]^2+[E+Fs]^2}\right) \quad \text{(B.262)}$$

where the constants are defined as,

$$A = R_2^2(X_1 + X_m) \tag{B.263}$$
$$B = (X_2 + X_m)(X_2X_m + X_1(X_2 + Xm)) \tag{B.264}$$
$$C = R_1R_2 \tag{B.265}$$
$$D = (X_2 + X_m) + X_1(X_2 + Xm) \tag{B.266}$$
$$E = R_2(X_1 + Xm) \tag{B.267}$$
$$F = R_1(X_2 + Xm) \tag{B.268}$$
$$H = R_2X_m^2 \tag{B.269}$$
$$K = R_1R_2^2 \tag{B.270}$$
$$L = R_1(X_2 + Xm)^2. \tag{B.271}$$

The jacobian terms are given by:

$$\frac{\partial P_{k,FSWG}}{\partial V} = -2V_k\frac{K + Hs + Ls^2}{(C - Ds)^2 + (E + Fs)^2} \tag{B.272}$$
$$\frac{\partial P_{k,FSWG}}{\partial s} = -V_k^2\frac{((C - Ds)^2 + (E + Fs)^2)(H + 2Ls)}{((C - Ds)^2 + (E + Fs)^2)^2} + V_k^2\frac{(K + Hs + Ls^2)(2(EF - CD) + 2(D^2 + F^2)s)}{((C - Ds)^2 + (E + Fs)^2)^2} \tag{B.273}$$
$$\frac{\partial Q_{k,FSWG}}{\partial V} = -2V_k\frac{A + Bs^2}{(C - Ds)^2 + (E + Fs)^2} \tag{B.274}$$
$$\frac{\partial Q_{k,FSWG}}{\partial s} = -V_k^2\frac{((C - Ds)^2 + (E + Fs)^2)(2Bs)}{((C - Ds)^2 + (E + Fs).^2).^2} + V_k^2\frac{(A + Bs^2)(2(EF - CD) + 2(D^2 + F^2)s)}{((C - Ds)^2 + (E + Fs)^2)^2} \tag{B.275}$$

In this case, B.259 and B.260 correspond to the estimated measures representing the measurements of active and reactive power injections at the generator's node. The FSWG state variable to be estimated corresponds to the slip , which is updated at each iteration of the SE according to $s^{i+1} = s^i + \Delta s^i$.

#### B.1.6.2 Semi-variable speed wind generator

A SSWG uses a Wound Rotor Induction Generator (WRIG) to provide a limited variable speed operation by controlling the rotor circuit resistance through an optical controlled converter mounted on the rotor shaft. This variable rotor

resistance permits the control of the generator's slip, and hence the generator's power output is also controlled [22-24].

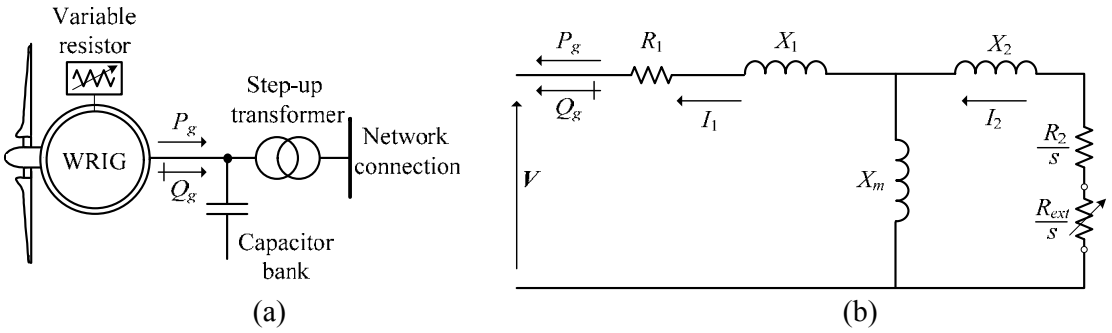


FIGURE B.7: Semi-variable speed wind generator: (a) schematic diagram (b) steady-state model

The mathematical model of the SSWG is also derived from the steady state equivalent model shown in Fig. B.7, but the rotor resistance $R_2/2$ is now replaced by $R_X = (R_2 + R_{ext})/s$. Since the variables $s$ and $R_{ext}$ are directly correlated by one single equation, the total resistance $R_X$ of the rotor circuit has been considered as the WTG's state variable to be estimated. Based on the information mentioned above, the active and reactive powers at the generator's terminals are given by [9]:

$$P_{k,SSWG}(V, R_x) = -V_k^2 \left( \frac{K' R_x^2 + H' R_x + L}{[C' R_x - D]^2 + [E' R_x + F]^2} \right) \quad \text{(B.276)}$$

$$Q_{k,SSWG}(V, R_x) = -V_k^2 \left( \frac{A' R_x^2 + B}{[C' R_x - D]^2 + [E' R_x + F]^2} \right) \quad \text{(B.277)}$$

where

$$A' = X_1 + X_m \quad \text{(B.278)}$$

$$C' = R_1 \quad \text{(B.279)}$$

$$E' = X_1 + X_m \quad \text{(B.280)}$$

$$H' = X_m^2 \quad \text{(B.281)}$$

$$K' = R_1 \quad \text{(B.282)}$$

while the current phasor in rectangular components is given by

$$I_{k,FSWG}(V, s) = V_k \left( \frac{(K' R_x^2 + H' R_x + L)\cos\theta + (A + Bs^2)\sin\theta}{[C' R_x - D]^2 + [E' R_x + F]^2} \right) \quad \text{(B.283)}$$

$$I_{k,FSWG}(V, s) = V_k \left( \frac{(K' R_x^2 + H' R_x + L)\sin\theta - (A + Bs^2)\cos\theta}{[C' R_x - D]^2 + [E' R_x + F]^2} \right) \quad \text{(B.284)}$$

The jacobian terms are given by:

$$\frac{\partial P_{k,SSWG}}{\partial V} = -2V_k \frac{KR_x^2 + HR_x + L}{(CR_x - D)^2 + (ER_x + F)^2} \tag{B.285}$$

$$\frac{\partial P_{k,SSWG}}{\partial R_x} = -V_k^2 \frac{(KR_x^2 + HR_x + L)(2(CR_x - D)C + 2(ER_x + F)E)}{(CR_x - D)^2 + (ER_x + F)^2)^2} + V_k^2 \frac{((CR_x - D)^2 + (ER_x + F)^2)(2KR_x + H)}{(CR_x - D)^2 + (ER_x + F)^2)^2} \tag{B.286}$$

$$\frac{\partial Q_{k,SSWG}}{\partial V} = -2V_k \frac{AR_x^2 + B}{(CR_x - D)^2 + (ER_x + F)^2} \tag{B.287}$$

$$\frac{\partial Q_{k,SSWG}}{\partial R_x} = -V_k^2 \frac{((CR_x - D)^2 + (ER_x + F)^2)(2AR_x)}{((CR_x - D)^2 + (ER_x + F)^2)^2} + V_k^2 \frac{(AR_x^2 + B)(2(CR_x - D)C + 2(ER_x + F)E)}{((CR_x - D)^2 + (ER_x + F)^2)^2} \tag{B.288}$$

### B.1.6.3 Variable speed wind generator DFIG

This type of WTG has become very popular because of its ability to achieve maximum efficiency over large speed variations around the synchronous speed. The DFIG uses a WRIG with slip rings and the rotor winding is fed by a partial scale frequency converter for allowing variable-speed operation of the wind turbine. The DFIG's power flow model proposed in [11], based on the equivalent circuit shown in Fig. 3 [11], has been adopted in this paper for estimating the seven state variables associated with this WTGs and two network's state variables. The former set of variables are , , , , , and , where subscripts m, r and g represent the magnetization branch, the rotor and the grid side converter variables, respectively. Moreover, the two network's state variables are defined by the stator variables, , .

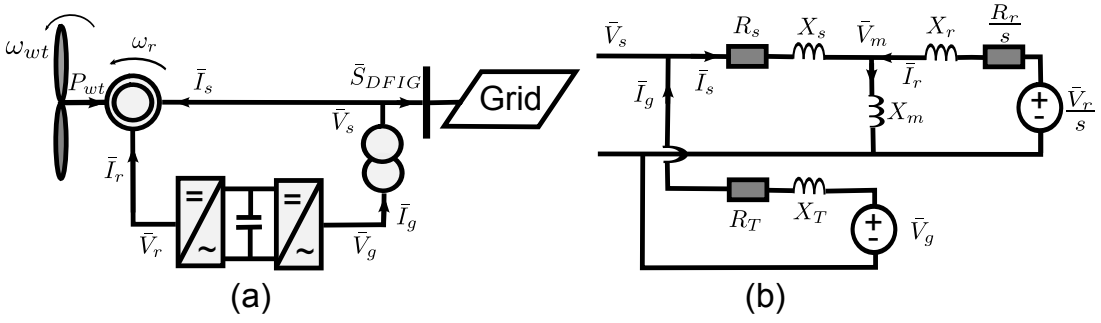


FIGURE B.8: Variable speed wind generator DFIG: (a) schematic diagram (b) steady-state model

The estimated measurements relating active and reactive power injections to measures provided by the SCADA system are:

$$P_{DFIG} = P_{wt} - \frac{P_{sm}^2 + Q_{sm}^2}{V_s^2} R_s - \frac{P_{mr}^2 + Q_{mr}^2}{V_m^2} R_r - \frac{P_{gs}^2 + Q_{gs}^2}{V_g^2} R_T \quad \text{(B.289)}$$

$$Q_{DFIG} = -Q_{sm} - Q_{sg} \quad \text{(B.290)}$$

Lastly, six equality constraints obtained from the DFIG's equivalent circuit are used as pseudo-measurements in order to facilitate the estimation of its internal state variables. These constraints correspond to the mismatch equations of active power in the stator winding (23), active and reactive powers at node m (24) and (25), active power at the back-to-back converter (26), reactive power setting at the grid-side converter (27) and the electromagnetic torque (28), respectively

$$\Delta P_s = -P_{DFIG} - P_{sm} - P_{sg} = 0 \quad \text{(B.291)}$$

$$\Delta P_m = -P_{ms} - P_{mr} = 0 \quad \text{(B.292)}$$

$$\Delta Q_m = -Q_{ms} - Q_{mm} - Q_{mr} = 0 \quad \text{(B.293)}$$

$$\Delta P_g = -P_{rm} - P_{gs} = 0 \quad \text{(B.294)}$$

$$\Delta Q_g = -Q_{g,set} - Q_{gs} = 0 \quad \text{(B.295)}$$

$$\Delta T = -\frac{P_{wt}}{1-s} - P_{em} = 0 \quad \text{(B.296)}$$

#### B.1.6.4 Permanent magnet synchronous generator

This configuration uses a PMSG connected to the grid through a full-scale frequency converter, the generator is therefore completely decoupled from the network permitting variable-speed operation: the network frequency remains unchanged to variations of the generator's electrical frequency because of changes in the wind speed. The schematic diagram and equivalent circuit of this topology is shown in Fig. 4, where and are the voltages at the machine-side converter and grid-side converter terminals, respectively, and is the step-up transformer impedance.

Based on Fig. B.9, the active and reactive powers flowing from the grid-side converter terminal to the k-th network's node are (29) and (30), respectively, where is the WTG's state variable to be estimated. The estimated real and imaginary

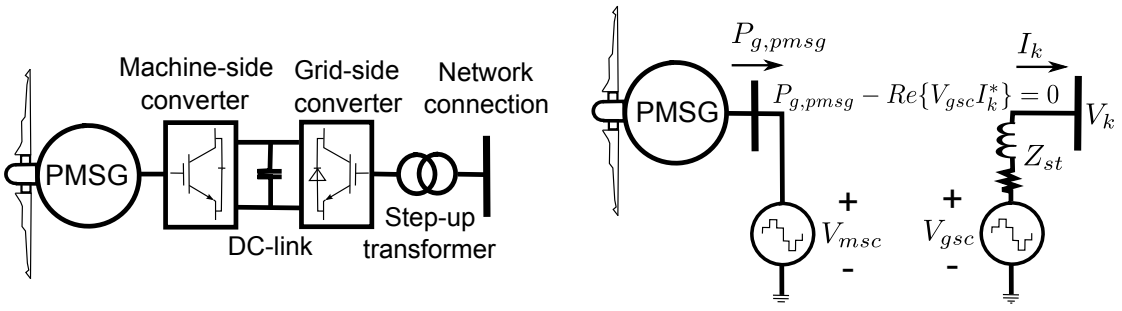


FIGURE B.9: Permanent magnet synchronous generator: (a) schematic diagram (b) steady-state model

currents representing the current phasor measured by a PMU at the PMSG's terminals are given by (31) and (32), respectively

$$P_{k,PMSG} = V_{gsc}^2 G_{st} + V_{gsc}V_k[G_{st}\cos(\delta_{gsc} - \theta_k) + B_{st}\sin(\delta_{gsc} - \theta_k)] \quad \text{(B.297)}$$

$$Q_{k,PMSG} = -V_{gsc}^2 B_{st} + V_{gsc}V_k[G_{st}\sin(\delta_{gsc} - \theta_k) - B_{st}\cos(\delta_{gsc} - \theta_k)] \quad \text{(B.298)}$$

The jacobian terms are given by:

$$\frac{\partial P_{k,PMSG}}{\partial \theta_k} = -V_{gsc}V_k(G_{st}sin(\theta_k - \theta_{gsc}) - B_{st}cos(\theta_k - \theta_{gsc})) \quad \text{(B.299)}$$

$$\frac{\partial P_{k,PMSG}}{\partial V_k} = -2V_kG_{st} - V_{gsc}(-G_{st}cos(\theta_k - \theta_{gsc}) - B_{st}sin(\theta_k - \theta_{gsc})) \quad \text{(B.300)}$$

$$\frac{\partial P_{k,PMSG}}{\partial \theta_{gsc}} = -V_{gsc}V_k(-G_{st}sin(\theta_k - \theta_{gsc}) + B_{st}cos(\theta_k - \theta_{gsc})) \quad \text{(B.301)}$$

$$\frac{\partial P_{k,PMSG}}{\partial V_{gsc}} = -V_k(-G_{st}cos(\theta_k - \theta_{gsc}) - B_{st}sin(\theta_k - \theta_{gsc})) \quad \text{(B.302)}$$

$$\frac{\partial Q_{k,PMSG}}{\partial \theta_k} = -V_{gsc}V_k(-G_{st}cos(\theta_k - \theta_{gsc}) - B_{st}sin(\theta_k - \theta_{gsc})) \quad \text{(B.303)}$$

$$\frac{\partial Q_{k,PMSG}}{\partial V_k} = 2V_kB_{st} - V_{gsc}(-G_{st}sin(\theta_k - \theta_{gsc}) + B_{st}cos(\theta_k - \theta_{gsc})) \quad \text{(B.304)}$$

$$\frac{\partial Q_{k,PMSG}}{\partial \theta_{gsc}} = V_{gsc}V_k(G_{st}cos(\theta_{gsc} - \theta_k) + B_{st}sin(\theta_{gsc} - \theta_k)) \quad \text{(B.305)}$$

$$\frac{\partial Q_{k,PMSG}}{\partial V_{gsc}} = -V_k(-G_{st}sin(\theta_k - \theta_{gsc}) + B_{st}cos(\theta_k - \theta_{gsc})) \quad \text{(B.306)}$$

### B.1.7 Automatic Load Frequency Control

The automatic control action of primary frequency regulation permits balancing the short-term wind power variability by driving the conventional generators to an

off-nominal frequency operating point. This frequency deviation from its nominal value is estimated in the proposed approach based on the generator and load models proposed in [42], which are reported below.

In order to consider the governor's effect on the power generation, the estimated active power generated by the i-th machine is given by [42],

$$P_{Gi} = P_{Gi-set} - \frac{P_{Ri}}{R_i}\Delta f \tag{B.307}$$

where $P_{Gi-set}$ is the active scheduled output of generator, $P_{Ri}$ is the rated output, $R_i$ is the speed regulation, and $\Delta f$ is the estimated system's frequency deviation. Besides, the estimated value of reactive power supplied or absorbed by the i-th machine is mathematically represented by

$$Q_{Gi} = Q_{Gi-set} - a_{Qi}\left(\frac{P_{Ri}}{R_i}\Delta f\right) + b_{Qi}\left(\frac{P_{Ri}}{R_i}\Delta f\right)^2 \tag{B.308}$$

where $Q_{Gi-set}$ is the reactive scheduled output of generator whilst $a_{Qi}$ and $b_{Qi}$ are the coefficients of reactive power generation control characteristics.

The load model at the i-th node is expressed as a function of voltage magnitude and frequency variations by

$$P_{Li} = P_{Lset,i}\left(1 + K_{pi}\Delta f\right)\left(p_{pi} + p_{ci}\left(\frac{V_i}{V_{LBi}}\right)^{N1} + p_{zi}\left(\frac{V_i}{V_{LBi}}\right)^2\right) \tag{B.309}$$

$$Q_{Li} = Q_{Lset,i}\left(1 + K_{qi}\Delta f\right)\left(q_{pi} + q_{ci}\left(\frac{V_i}{V_{LBi}}\right)^{N2} + q_{zi}\left(\frac{V_i}{V_{LBi}}\right)^2\right) \tag{B.310}$$

where $P_{Li}$ and $Q_{Li}$ are the estimations of active and reactive powers demanded by the load, respectively. $P_{Li-set}$ and $Q_{Li-set}$ are the rated power of load. In addition, $K_{pi}$ and $K_{qi}$ are frequency characteristic coefficients and $p_{zi}$ and $q_{zi}$ are the portion of total load proportional to constant impedance load. Furthermore, $p_{ci}$ and $q_{ci}$ are the portion of total load proportional to $N^{th}$ power of voltage, while $p_{pi}$ and $q_{pi}$ are the portion of total load proportional to constant power load. Lastly, $V_{LBi}$ and $V_i$ are the nominal and actual voltage magnitude at load node, respectively.

# Appendix C

# Cases of Study and System Data

## C.1 Nordic system

Nordic system documented in [84] for long-term voltage stability analysis, is used in this thesis to test the state estimation performance under severe disturbance. The one-line diagram of Nordic system is shown in Figure C.1 and the summary of devices in Table C.1.

TABLE C.1: Nordic system summary

| Bus | Machines | T. Lines | Transformers | LTCs | Loads | FSC |
|---|---|---|---|---|---|---|
| 74 | 20 | 52 | 50 | 22 | 22 | 11 |

As can be observed in Figure C.1, Nordic system is composed of a transmission system 400-220kV, a sub-transmission 130kV and 22 distribution buses where loads are connected. The system is divided in four areas, named: *north*, *equiv*, *central* and *south*. Hydro units with primary frequency control are placed in *north* and *equiv* areas, while thermal units with constant mechanical power in areas *central* and *south*. Also long series compensated 400kv lines connected from north to central.

A detailed time simulation of Nordic system has been performed in RAMSES [79], a dynamic simulation tool developed in ULg, in order to obtain the "exact" system evolution after a severe disturbance. The simulated model involves:

- detailed representation of the 20 synchronous generators;
- generic models for AVRs, excitation systems, prime movers and speed governors;

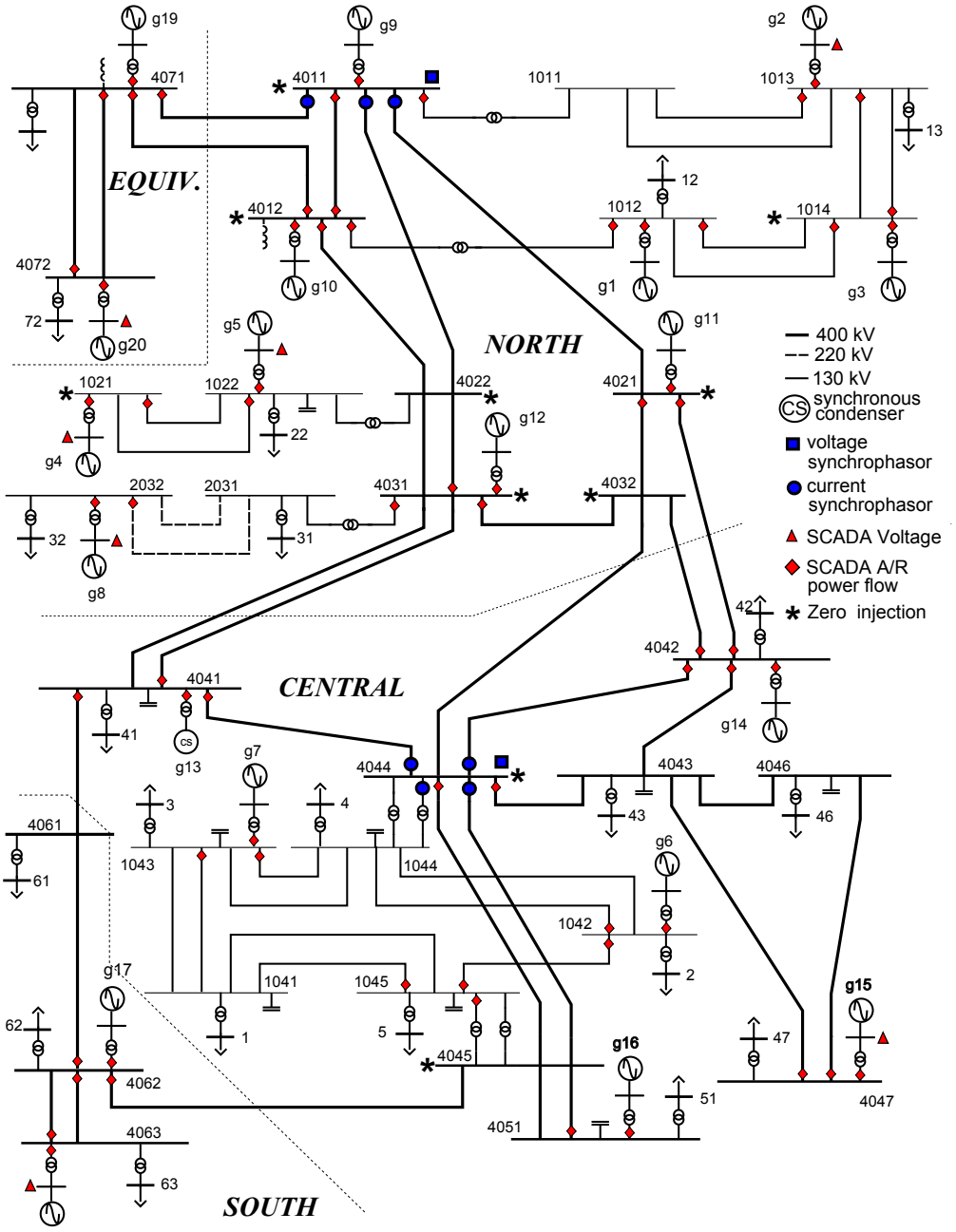


FIGURE C.1: One-line diagram of Nordic system

- 20 step-up transformers for generators (including one synchronous condenser), 8 transformers 400/220 and 400/130 and 22 step-down transformers;
- 22 Load Tap Changers (LTCs) controlling with various delays with voltage deadband of [0.99 1.01] pu and range of transformer ratio of [0.88 1.20] pu/pu;
- exponential model for load power variation with voltage;
- OverExcitation Limiters (OELs) with either fixed- or inverse-time response;

- Under voltage load shedding (UVLS).

### C.1.1 Operating without disturbance

In this case, also referred as *normal operation scenario* in this dissertations, no disturbance is applied to the system, hence all system voltages remain constant and only Gaussian Random Noise affect the state estimation.

On the other hand, two scenarios with disturbances have been considered. In all cases a three-phase solid fault was applied on line 4032-4044 and cleared after five cycles by opening the line.

### C.1.2 Operating Point A. Voltage Collapse

This first scenario does not include remedial actions, and after the fault the system experiences long-term voltage instability under the effect of load tap changers and overexcitation limiters.

The following sequence of events have been considered:

- three-phase solid fault applied on line 4032-4044, near bus 4032, at $t = 1s$, and cleared 5 cycles later at $t = 1.1s$ by opening that line, which remains opened;
- in response to the initial disturbance the system undergoes electromechanical oscillations that die out around 10 seconds;
- the voltage is kept fairly constant by the automatic voltage regulator, until the field current gets limited (a total of seven generators get limited during the simulation: g12, g14, g7, g11, g6, g15 and g16);
- Jumps at $t \approx 65s$ and $t \approx 132s$ correspond to machines switching under field current limit which causes voltages drops;
- at $t \approx 140s$ generator g7 is tripped due to the effect of an under-voltage protection set to act at a generator voltage of 0.85 pu;
- at $t \approx 164s$ the machine g6 loss of synchronism with respect to the other machines, which causes the final system voltage collapse;

- during all the simulation the system experiment 117 LTCs operations.

### C.1.3 Operating Point A. Undervoltage Load Shedding

This case includes emergency system stabilization by under-voltage load shedding which makes the system long-term voltage stable. Distributed controllers have been considered, each controller monitors the voltage at a transmission bus and acts on the load at the nearest distribution bus, according to the following logic: shed 50 MW of load when the monitored voltage $V$ goes below a threshold 0.9pu for more than 3 seconds. As in previous case at $t \approx 65s$ machines switching under field current limit causes voltages drops, however in this case, in order to avoid the voltage collapse six blocks of load are shed, two at the MV bus connected to bus 1041 (at $t \approx 100s$ and $143s$) and four at the MV bus connected to bus 1044 (at $t \approx 112s$, 123s, $180s$ and $292s$), for a total of 300 MW.

Figure C.2 shows main events that occur during the simulation.

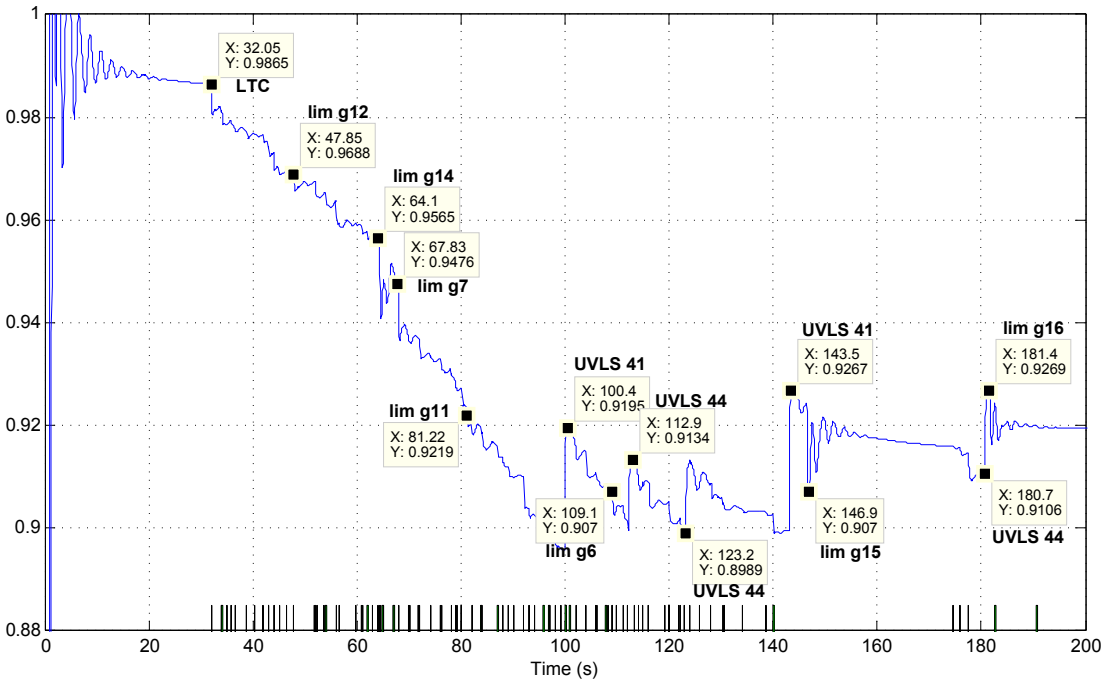


FIGURE C.2: Main events occurred during operating point A simulation. Black bars show the time in which LTC's are operating.

Tables C.2 to C.5 show the parameters of devices used for state estimation analysis.

TABLE C.2: Parameters of transmission lines

| Line Name | from bus | to bus | $R$ ($\Omega$) | $X$ $\Omega$ | $\omega C/2$ $\mu S$ | $S_{nom}$ MVA |
|---|---|---|---|---|---|---|
| 1011-1013 | 1011 | 1013 | 1.69 | 11.83 | 40.841 | 350 |
| 1011-1013b | 1011 | 1013 | 1.69 | 11.83 | 40.841 | 350 |
| 1012-1014 | 1012 | 1014 | 2.37 | 15.21 | 53.407 | 350 |
| 1012-1014b | 1012 | 1014 | 2.37 | 15.21 | 53.407 | 350 |
| 1013-1014 | 1013 | 1014 | 1.18 | 8.45 | 29.845 | 350 |
| 1013-1014b | 1013 | 1014 | 1.18 | 8.45 | 29.845 | 350 |
| 1021-1022 | 1021 | 1022 | 5.07 | 33.8 | 89.535 | 350 |
| 1021-1022b | 1021 | 1022 | 5.07 | 33.8 | 89.535 | 350 |
| 1041-1043 | 1041 | 1043 | 1.69 | 10.14 | 36.128 | 350 |
| 1041-1043b | 1041 | 1043 | 1.69 | 10.14 | 36.128 | 350 |
| 1041-1045 | 1041 | 1045 | 2.53 | 20.28 | 73.827 | 350 |
| 1041-1045b | 1041 | 1045 | 2.53 | 20.28 | 73.827 | 350 |
| 1042-1044 | 1042 | 1044 | 6.42 | 47.32 | 177.5 | 350 |
| 1042-1044b | 1042 | 1044 | 6.42 | 47.32 | 177.5 | 350 |
| 1042-1045 | 1042 | 1045 | 8.45 | 50.7 | 177.5 | 350 |
| 1043-1044 | 1043 | 1044 | 1.69 | 13.52 | 47.124 | 350 |
| 1043-1044b | 1043 | 1044 | 1.69 | 13.52 | 47.124 | 350 |
| 2031-2032 | 2031 | 2032 | 5.81 | 43.56 | 15.708 | 500 |
| 2031-2032b | 2031 | 2032 | 5.81 | 43.56 | 15.708 | 500 |
| 4011-4012 | 4011 | 4012 | 1.6 | 12.8 | 62.832 | 1400 |
| 4011-4021 | 4011 | 4021 | 9.6 | 96 | 562.34 | 1400 |
| 4011-4022 | 4011 | 4022 | 6.4 | 64 | 375.42 | 1400 |
| 4011-4071 | 4011 | 4071 | 8 | 72 | 438.25 | 1400 |
| 4012-4022 | 4012 | 4022 | 6.4 | 56 | 328.3 | 1400 |
| 4012-4071 | 4012 | 4071 | 8 | 80 | 468.1 | 1400 |
| 4021-4032 | 4021 | 4032 | 6.4 | 64 | 375.42 | 1400 |
| 4021-4042 | 4021 | 4042 | 16 | 96 | 937.77 | 1400 |
| 4022-4031 | 4022 | 4031 | 6.4 | 64 | 375.42 | 1400 |
| 4022-4031b | 4022 | 4031 | 6.4 | 64 | 375.42 | 1400 |
| 4031-4032 | 4031 | 4032 | 1.6 | 16 | 94.248 | 1400 |
| 4031-4041 | 4031 | 4041 | 9.6 | 64 | 749.27 | 1400 |
| 4031-4041b | 4031 | 4041 | 9.6 | 64 | 749.27 | 1400 |
| 4032-4042 | 4032 | 4042 | 16 | 64 | 625.18 | 1400 |
| 4032-4044 | 4032 | 4044 | 9.6 | 80 | 749.27 | 1400 |
| 4041-4044 | 4041 | 4044 | 4.8 | 48 | 281.17 | 1400 |
| 4041-4061 | 4041 | 4061 | 9.6 | 72 | 406.84 | 1400 |
| 4042-4043 | 4042 | 4043 | 3.2 | 24 | 155.51 | 1400 |
| 4042-4044 | 4042 | 4044 | 3.2 | 32 | 186.93 | 1400 |
| 4043-4044 | 4043 | 4044 | 1.6 | 16 | 94.248 | 1400 |
| 4043-4046 | 4043 | 4046 | 1.6 | 16 | 94.248 | 1400 |
| 4043-4047 | 4043 | 4047 | 3.2 | 32 | 186.93 | 1400 |
| 4044-4045 | 4044 | 4045 | 3.2 | 32 | 186.93 | 1400 |
| 4044-4045b | 4044 | 4045 | 3.2 | 32 | 186.93 | 1400 |
| 4045-4051 | 4045 | 4051 | 6.4 | 64 | 375.42 | 1400 |
| 4045-4051b | 4045 | 4051 | 6.4 | 64 | 375.42 | 1400 |
| 4045-4062 | 4045 | 4062 | 17.6 | 128 | 749.27 | 1400 |
| 4046-4047 | 4046 | 4047 | 1.6 | 24 | 155.51 | 1400 |
| 4061-4062 | 4061 | 4062 | 3.2 | 32 | 186.93 | 1400 |
| 4062-4063 | 4062 | 4063 | 4.8 | 48 | 281.17 | 1400 |
| 4062-4063b | 4062 | 4063 | 4.8 | 48 | 281.17 | 1400 |
| 4071-4072 | 4071 | 4072 | 4.8 | 48 | 937.77 | 1400 |
| 4071-4072b | 4071 | 4072 | 4.8 | 48 | 937.77 | 1400 |

TABLE C.3: Parameters of step-up transformers

| Transformer Name | from bus | to bus | $X$ p.u | $n$ pu/pu | $S_{nom}$ MVA |
|---|---|---|---|---|---|
| g1 | g1 | 1012 | 0.15 | 1 | 800 |
| g2 | g2 | 1013 | 0.15 | 1 | 600 |
| g3 | g3 | 1014 | 0.15 | 1 | 700 |
| g4 | g4 | 1021 | 0.15 | 1 | 600 |
| g5 | g5 | 1022 | 0.15 | 1.05 | 250 |
| g6 | g6 | 1042 | 0.15 | 1.05 | 400 |
| g7 | g7 | 1043 | 0.15 | 1.05 | 200 |
| g8 | g8 | 2032 | 0.15 | 1.05 | 850 |
| g9 | g9 | 4011 | 0.15 | 1.05 | 1000 |
| g10 | g10 | 4012 | 0.15 | 1.05 | 800 |
| g11 | g11 | 4021 | 0.15 | 1.05 | 300 |
| g12 | g12 | 4031 | 0.15 | 1.05 | 350 |
| g13 | g13 | 4041 | 0.1 | 1.05 | 300 |
| g14 | g14 | 4042 | 0.15 | 1.05 | 700 |
| g15 | g15 | 4047 | 0.15 | 1.05 | 1200 |
| g16 | g16 | 4051 | 0.15 | 1.05 | 700 |
| g17 | g17 | 4062 | 0.15 | 1.05 | 600 |
| g18 | g18 | 4063 | 0.15 | 1.05 | 1200 |
| g19 | g19 | 4071 | 0.15 | 1.05 | 500 |
| g20 | g20 | 4072 | 0.15 | 1.05 | 4500 |

TABLE C.4: Parameters of 400/220 and 400/130 transformers

| Transformer Name | from bus | to bus | $X$ p.u | $n$ pu/pu | $S_{nom}$ MVA |
|---|---|---|---|---|---|
| 1011-4011 | 1011 | 4011 | 0.1 | 0.95 | 1250 |
| 1012-4012 | 1012 | 4012 | 0.1 | 0.95 | 1250 |
| 1022-4022 | 1022 | 4022 | 0.1 | 0.93 | 833.3 |
| 2031-4031 | 2031 | 4031 | 0.1 | 1 | 833.3 |
| 1044-4044 | 1044 | 4044 | 0.1 | 1.03 | 1000 |
| 1044-4044b | 1044 | 4044 | 0.1 | 1.03 | 1000 |
| 1045-4045 | 1045 | 4045 | 0.1 | 1.04 | 1000 |
| 1045-4045b | 1045 | 4045 | 0.1 | 1.04 | 1000 |

TABLE C.5: Shunt Compensation

| Bus | $Q_{nom}$ MVAR |
|---|---|
| 1022 | 50 |
| 1041 | 250 |
| 1043 | 200 |
| 1044 | 200 |
| 1045 | 200 |
| 4012 | -100 |
| 4041 | 200 |
| 4043 | 200 |
| 4046 | 100 |
| 4051 | 100 |
| 4071 | -400 |

## C.2 Modified IEEE118-bus network

The IEEE 118-bus test system which a portion of the American Electric Power System has been employed as a benchmark system to illustrate proposals associated with steady state analysis of power system. The system has been modified and decomposed into nine observable subareas, as shown in Figure C.3 [23], and has been modified to include five FACTS controllers, five WTGs, nine generators

participating in the frequency regulation, one per area, and three loads whose power demand depends on the voltage magnitude and frequency values. The parameters and control settings of FACTS controllers are reported in Tables 1 and 2, respectively, where the acronyms SVC, TCSC, UPFC, LTC and PS stand for the static VARs compensator, thyristor-controlled series compensator, unified power flow controller, load tap changer and phase shifter transformers, respectively. Detailed models of these controllers for SE are given in [15]. The parameters of WTGs are also reported in Table 1, while data related to regulated generators and dependent loads are given in Table 3.

TABLE C.6: IEEE-118 modified system summary

| Bus | Gen | GLFC | Lines | Transfo | Loads | SC | LTC | PST | FACTS | WG |
|---|---|---|---|---|---|---|---|---|---|---|
| 122 | 45 | 9+3 | 177 | 9 | 115 | 13 | 1 | 1 | 3 | 3 |

TABLE C.7: Slack bus IEEE-118 modified

| Slack | C1 | C2 | C3 | C4 | C5 | C6 | C7 | C8 | C9 |
|---|---|---|---|---|---|---|---|---|---|
| 69 | 30 | 0 | 548.51 | -101.38 | 1.035 | 1 | 0.04 | 1 | 1 |

TABLE C.8: Transformer parameters

| from bus | to bus | Primary winding | | | | Secondary winding | | | | Magnetizing branch | |
|---|---|---|---|---|---|---|---|---|---|---|---|
| | | $R_1$ p.u | $X_{L1}$ p.u | $V_{1tap}$ p.u | $\theta_{1tap}$ p.u | $R_2$ p.u | $X_{L2}$ p.u | $V_{2tap}$ p.u | $\theta_{2tap}$ p.u | $G_{shunt}$ p.u | $B_{shunt}$ p.u |
| 8 | 5 | 0 | 0 | 0.985 | 0 | 0 | 0.0267 | 1 | 0 | 0 | 0 |
| 26 | 25 | 0 | 0 | 0.96 | 0 | 0 | 0.0382 | 1 | 0 | 0 | 0 |
| 30 | 17 | 0 | 0 | 0.96 | 0 | 0 | 0.0388 | 1 | 0 | 0 | 0 |
| 38 | 37 | 0 | 0 | 0.935 | 0 | 0 | 0.0375 | 1 | 0 | 0 | 0 |
| 63 | 59 | 0 | 0 | 0.96 | 0 | 0 | 0.0386 | 1 | 0 | 0 | 0 |
| 64 | 61 | 0 | 0 | 0.985 | 0 | 0 | 0.0268 | 1 | 0 | 0 | 0 |
| 65 | 66 | 0 | 0 | 0.935 | 0 | 0 | 0.037 | 1 | 0 | 0 | 0 |
| 68 | 69 | 0 | 0 | 0.935 | 0 | 0 | 0.037 | 1 | 0 | 0 | 0 |
| 81 | 80 | 0 | 0 | 0.935 | 0 | 0 | 0.037 | 1 | 0 | 0 | 0 |

TABLE C.9: Load Tap Changer parameters

| from bus | to bus | Primary winding | | | | Secondary winding | | | | Magnetizing branch | |
|---|---|---|---|---|---|---|---|---|---|---|---|
| | | $R_1$ p.u | $X_{L1}$ p.u | $V_{1tap}$ p.u | $\theta_{1tap}$ p.u | $R_2$ p.u | $X_{L2}$ p.u | $V_{2tap}$ p.u | $\theta_{2tap}$ p.u | $G_{shunt}$ p.u | $B_{shunt}$ p.u |
| 21 | 122 | 0 | 0.1 | 0 | 0.1 | 0 | 0 | 1 | 1 | 0 | 0 |

TABLE C.10: Phase Shifter parameters

| from bus | to bus | Primary winding | | | | Secondary winding | | | | Magnetizing branch | |
|---|---|---|---|---|---|---|---|---|---|---|---|
| | | $R_1$ p.u | $X_{L1}$ p.u | $V_{1tap}$ p.u | $\theta_{1tap}$ p.u | $R_2$ p.u | $X_{L2}$ p.u | $V_{2tap}$ p.u | $\theta_{2tap}$ p.u | $G_{shunt}$ p.u | $B_{shunt}$ p.u |
| 70 | 121 | 0 | 0.05 | 0 | 0.05 | 0 | 0 | 1 | 1 | 0 | 0 |

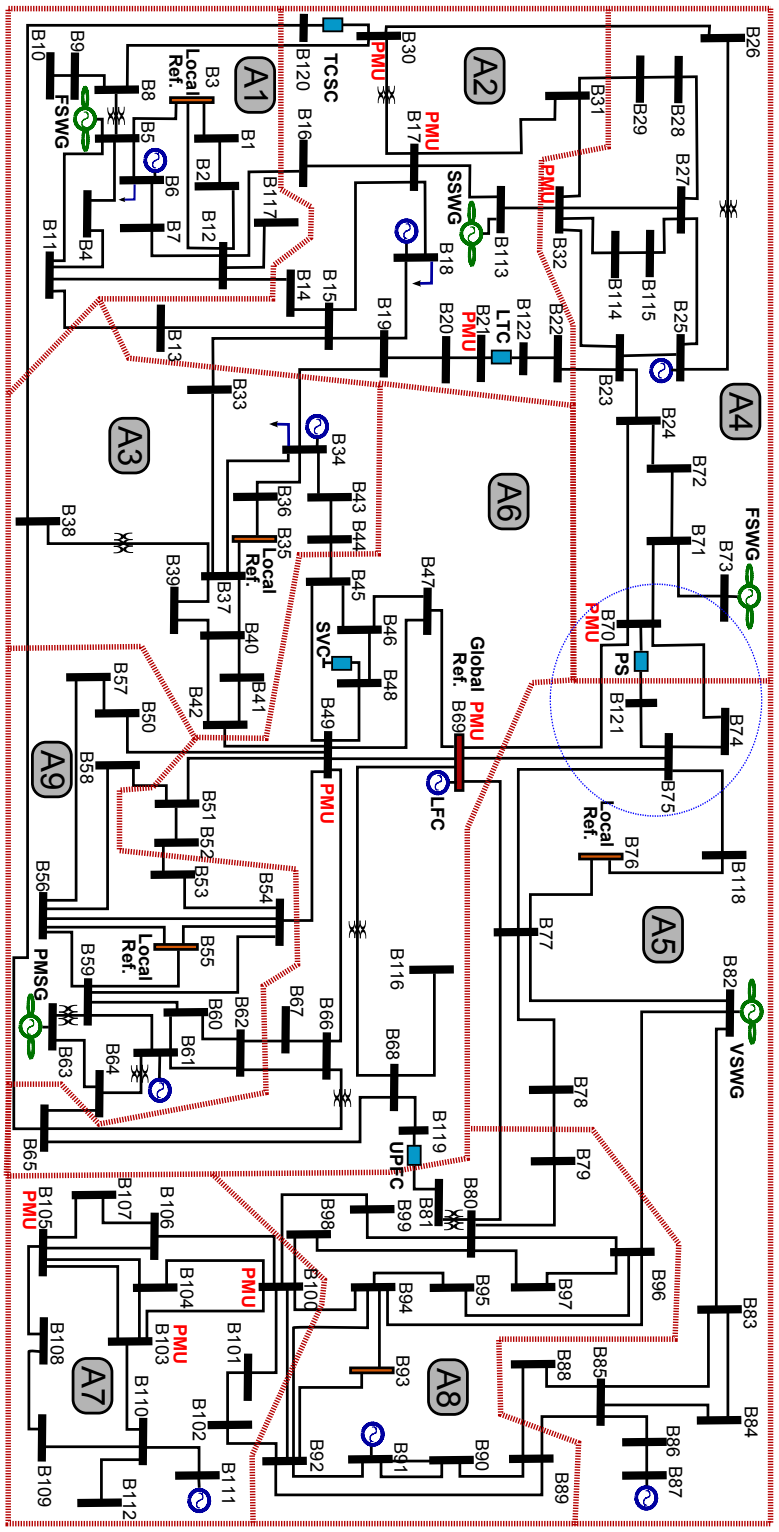


FIGURE C.3: One-line diagram of modified IEEE-118 test system

TABLE C.11: Parameters of transmission lines

| from bus | to bus | $R$ p.u | $X_L$ p.u | $G_{shunt}$ p.u | $B_{shunt}$ p.u |
|---|---|---|---|---|---|
| 1 | 2 | 0.03030 | 0.09990 | 0 | 0.02540 |
| 1 | 3 | 0.01290 | 0.04240 | 0 | 0.01082 |
| 4 | 5 | 0.00176 | 0.00798 | 0 | 0.00210 |
| 3 | 5 | 0.02410 | 0.10800 | 0 | 0.02840 |
| 5 | 6 | 0.01190 | 0.05400 | 0 | 0.01426 |
| 6 | 7 | 0.00459 | 0.02080 | 0 | 0.00550 |
| 8 | 9 | 0.00244 | 0.03050 | 0 | 1.16200 |
| 9 | 10 | 0.00258 | 0.03220 | 0 | 1.23000 |
| 4 | 11 | 0.02090 | 0.06880 | 0 | 0.01748 |
| 5 | 11 | 0.02030 | 0.06820 | 0 | 0.01738 |
| 11 | 12 | 0.00595 | 0.01960 | 0 | 0.00502 |
| 2 | 12 | 0.01870 | 0.06160 | 0 | 0.01572 |
| 3 | 12 | 0.04840 | 0.16000 | 0 | 0.04060 |
| 7 | 12 | 0.00862 | 0.03400 | 0 | 0.00874 |
| 11 | 13 | 0.02225 | 0.07310 | 0 | 0.01876 |
| 12 | 14 | 0.02150 | 0.07070 | 0 | 0.01816 |
| 13 | 15 | 0.07440 | 0.24440 | 0 | 0.06268 |
| 14 | 15 | 0.05950 | 0.19500 | 0 | 0.05020 |
| 12 | 16 | 0.02120 | 0.08340 | 0 | 0.02140 |
| 15 | 17 | 0.01320 | 0.04370 | 0 | 0.04440 |
| 16 | 17 | 0.04540 | 0.18010 | 0 | 0.04660 |
| 17 | 18 | 0.01230 | 0.05050 | 0 | 0.01298 |
| 18 | 19 | 0.01119 | 0.04930 | 0 | 0.01142 |
| 19 | 20 | 0.02520 | 0.11700 | 0 | 0.02980 |
| 15 | 19 | 0.01200 | 0.03940 | 0 | 0.01010 |
| 20 | 21 | 0.01830 | 0.08490 | 0 | 0.02160 |
| 122 | 22 | 0.02090 | 0.09700 | 0 | 0.02460 |
| 22 | 23 | 0.03420 | 0.15900 | 0 | 0.04040 |
| 23 | 24 | 0.01350 | 0.04920 | 0 | 0.04980 |
| 23 | 25 | 0.01560 | 0.08000 | 0 | 0.08640 |
| 25 | 27 | 0.03180 | 0.16300 | 0 | 0.17640 |
| 27 | 28 | 0.01913 | 0.08550 | 0 | 0.02160 |
| 28 | 29 | 0.02370 | 0.09430 | 0 | 0.02380 |
| 8 | 30 | 0.00431 | 0.05040 | 0 | 0.51400 |
| 26 | 30 | 0.00799 | 0.08600 | 0 | 0.90800 |
| 17 | 31 | 0.04740 | 0.15630 | 0 | 0.03990 |
| 29 | 31 | 0.01080 | 0.03310 | 0 | 0.00830 |
| 23 | 32 | 0.03170 | 0.11530 | 0 | 0.11730 |
| 31 | 32 | 0.02980 | 0.09850 | 0 | 0.02510 |
| 27 | 32 | 0.02290 | 0.07550 | 0 | 0.01926 |
| 15 | 33 | 0.03800 | 0.12440 | 0 | 0.03194 |
| 19 | 34 | 0.07520 | 0.24700 | 0 | 0.06320 |
| 35 | 36 | 0.00224 | 0.01020 | 0 | 0.00268 |
| 35 | 37 | 0.01100 | 0.04970 | 0 | 0.01318 |
| 33 | 37 | 0.04150 | 0.14200 | 0 | 0.03660 |
| 34 | 36 | 0.00871 | 0.02680 | 0 | 0.00568 |
| 34 | 37 | 0.00256 | 0.00940 | 0 | 0.00984 |
| 37 | 39 | 0.03210 | 0.10600 | 0 | 0.02700 |
| 37 | 40 | 0.05930 | 0.16800 | 0 | 0.04200 |
| 120 | 38 | 0.00464 | 0.05400 | 0 | 0.42200 |
| 39 | 40 | 0.01840 | 0.06050 | 0 | 0.01552 |
| 40 | 41 | 0.01450 | 0.04870 | 0 | 0.01222 |
| 40 | 42 | 0.05550 | 0.18300 | 0 | 0.04660 |
| 41 | 42 | 0.04100 | 0.13500 | 0 | 0.03440 |

*Continued on next page*

Table C.11 – *Continued from previous page*

| from bus | to bus | $R$ p.u | $X_L$ p.u | $G_{shunt}$ p.u | $B_{shunt}$ p.u |
|---|---|---|---|---|---|
| 43 | 44 | 0.06080 | 0.24540 | 0 | 0.06068 |
| 34 | 43 | 0.04130 | 0.16810 | 0 | 0.04226 |
| 44 | 45 | 0.02240 | 0.09010 | 0 | 0.02240 |
| 45 | 46 | 0.04000 | 0.13560 | 0 | 0.03320 |
| 46 | 47 | 0.03800 | 0.12700 | 0 | 0.03160 |
| 46 | 48 | 0.06010 | 0.18900 | 0 | 0.04720 |
| 47 | 49 | 0.01910 | 0.06250 | 0 | 0.01604 |
| 42 | 49 | 0.07150 | 0.32300 | 0 | 0.08600 |
| 42 | 49 | 0.07150 | 0.32300 | 0 | 0.08600 |
| 45 | 49 | 0.06840 | 0.18600 | 0 | 0.04440 |
| 48 | 49 | 0.01790 | 0.05050 | 0 | 0.01258 |
| 49 | 50 | 0.02670 | 0.07520 | 0 | 0.01874 |
| 49 | 51 | 0.04860 | 0.13700 | 0 | 0.03420 |
| 51 | 52 | 0.02030 | 0.05880 | 0 | 0.01396 |
| 52 | 53 | 0.04050 | 0.16350 | 0 | 0.04058 |
| 53 | 54 | 0.02630 | 0.12200 | 0 | 0.03100 |
| 49 | 54 | 0.07300 | 0.28900 | 0 | 0.07380 |
| 49 | 54 | 0.08690 | 0.29100 | 0 | 0.07300 |
| 54 | 55 | 0.01690 | 0.07070 | 0 | 0.02020 |
| 54 | 56 | 0.00275 | 0.00955 | 0 | 0.00732 |
| 55 | 56 | 0.00488 | 0.01510 | 0 | 0.00374 |
| 56 | 57 | 0.03430 | 0.09660 | 0 | 0.02420 |
| 50 | 57 | 0.04740 | 0.13400 | 0 | 0.03320 |
| 56 | 58 | 0.03430 | 0.09660 | 0 | 0.02420 |
| 51 | 58 | 0.02550 | 0.07190 | 0 | 0.01788 |
| 54 | 59 | 0.05030 | 0.22930 | 0 | 0.05980 |
| 56 | 59 | 0.08250 | 0.25100 | 0 | 0.05690 |
| 56 | 59 | 0.08030 | 0.23900 | 0 | 0.05360 |
| 55 | 59 | 0.04739 | 0.21580 | 0 | 0.05646 |
| 59 | 60 | 0.03170 | 0.14500 | 0 | 0.03760 |
| 59 | 61 | 0.03280 | 0.15000 | 0 | 0.03880 |
| 60 | 61 | 0.00264 | 0.01350 | 0 | 0.01456 |
| 60 | 62 | 0.01230 | 0.05610 | 0 | 0.01468 |
| 61 | 62 | 0.00824 | 0.03760 | 0 | 0.00980 |
| 63 | 64 | 0.00172 | 0.02000 | 0 | 0.21600 |
| 38 | 65 | 0.00901 | 0.09860 | 0 | 1.04600 |
| 64 | 65 | 0.00269 | 0.03020 | 0 | 0.38000 |
| 49 | 66 | 0.01800 | 0.09190 | 0 | 0.02480 |
| 49 | 66 | 0.01800 | 0.09190 | 0 | 0.02480 |
| 62 | 66 | 0.04820 | 0.21800 | 0 | 0.05780 |
| 62 | 67 | 0.02580 | 0.11700 | 0 | 0.03100 |
| 66 | 67 | 0.02240 | 0.10150 | 0 | 0.02682 |
| 65 | 68 | 0.00138 | 0.01600 | 0 | 0.63800 |
| 47 | 69 | 0.08440 | 0.27780 | 0 | 0.07092 |
| 49 | 69 | 0.09850 | 0.32400 | 0 | 0.08280 |
| 69 | 70 | 0.03000 | 0.12700 | 0 | 0.12200 |
| 24 | 70 | 0.00221 | 0.41150 | 0 | 0.10198 |
| 70 | 71 | 0.00882 | 0.03550 | 0 | 0.00878 |
| 24 | 72 | 0.04880 | 0.19600 | 0 | 0.04880 |
| 71 | 72 | 0.04460 | 0.18000 | 0 | 0.04444 |
| 71 | 73 | 0.00866 | 0.04540 | 0 | 0.01178 |
| 70 | 74 | 0.04010 | 0.13230 | 0 | 0.03368 |
| 121 | 75 | 0.04280 | 0.14100 | 0 | 0.03600 |
| 69 | 75 | 0.04050 | 0.12200 | 0 | 0.12400 |

*Continued on next page*

Table C.11 – *Continued from previous page*

| from bus | to bus | $R$ p.u | $X_L$ p.u | $G_{shunt}$ p.u | $B_{shunt}$ p.u |
|---|---|---|---|---|---|
| 74 | 75 | 0.01230 | 0.04060 | 0 | 0.01034 |
| 76 | 77 | 0.04440 | 0.14800 | 0 | 0.03680 |
| 69 | 77 | 0.03090 | 0.10100 | 0 | 0.10380 |
| 75 | 77 | 0.06010 | 0.19990 | 0 | 0.04978 |
| 77 | 78 | 0.00376 | 0.01240 | 0 | 0.01264 |
| 78 | 79 | 0.00546 | 0.02440 | 0 | 0.00648 |
| 77 | 80 | 0.01700 | 0.04850 | 0 | 0.04720 |
| 77 | 80 | 0.02940 | 0.10500 | 0 | 0.02280 |
| 79 | 80 | 0.01560 | 0.07040 | 0 | 0.01870 |
| 68 | 119 | 0.00175 | 0.02020 | 0 | 0.80800 |
| 77 | 82 | 0.02980 | 0.08530 | 0 | 0.08174 |
| 82 | 83 | 0.01120 | 0.03665 | 0 | 0.03796 |
| 83 | 84 | 0.06250 | 0.13200 | 0 | 0.02580 |
| 83 | 85 | 0.04300 | 0.14800 | 0 | 0.03480 |
| 84 | 85 | 0.03020 | 0.06410 | 0 | 0.01234 |
| 85 | 86 | 0.03500 | 0.12300 | 0 | 0.02760 |
| 86 | 87 | 0.02828 | 0.20740 | 0 | 0.04450 |
| 85 | 88 | 0.02000 | 0.10200 | 0 | 0.02760 |
| 85 | 89 | 0.02390 | 0.17300 | 0 | 0.04700 |
| 88 | 89 | 0.01390 | 0.07120 | 0 | 0.01934 |
| 89 | 90 | 0.05180 | 0.18800 | 0 | 0.05280 |
| 89 | 90 | 0.02380 | 0.09970 | 0 | 0.10600 |
| 90 | 91 | 0.02540 | 0.08360 | 0 | 0.02140 |
| 89 | 92 | 0.00990 | 0.05050 | 0 | 0.05480 |
| 89 | 92 | 0.03930 | 0.15810 | 0 | 0.04140 |
| 91 | 92 | 0.03870 | 0.12720 | 0 | 0.03268 |
| 92 | 93 | 0.02580 | 0.08480 | 0 | 0.02180 |
| 92 | 94 | 0.04810 | 0.15800 | 0 | 0.04060 |
| 93 | 94 | 0.02230 | 0.07320 | 0 | 0.01876 |
| 94 | 95 | 0.01320 | 0.04340 | 0 | 0.01110 |
| 80 | 96 | 0.03560 | 0.18200 | 0 | 0.04940 |
| 82 | 96 | 0.01620 | 0.05300 | 0 | 0.05440 |
| 94 | 96 | 0.02690 | 0.08690 | 0 | 0.02300 |
| 80 | 97 | 0.01830 | 0.09340 | 0 | 0.02540 |
| 80 | 98 | 0.02380 | 0.10800 | 0 | 0.02860 |
| 80 | 99 | 0.04540 | 0.20600 | 0 | 0.05460 |
| 92 | 100 | 0.06480 | 0.29500 | 0 | 0.04720 |
| 94 | 100 | 0.01780 | 0.05800 | 0 | 0.06040 |
| 95 | 96 | 0.01710 | 0.05470 | 0 | 0.01474 |
| 96 | 97 | 0.01730 | 0.08850 | 0 | 0.02400 |
| 98 | 100 | 0.03970 | 0.17900 | 0 | 0.04760 |
| 99 | 100 | 0.01800 | 0.08130 | 0 | 0.02160 |
| 100 | 101 | 0.02770 | 0.12620 | 0 | 0.03280 |
| 92 | 102 | 0.01230 | 0.05590 | 0 | 0.01464 |
| 101 | 102 | 0.02460 | 0.11200 | 0 | 0.02940 |
| 100 | 103 | 0.01600 | 0.05250 | 0 | 0.05360 |
| 100 | 104 | 0.04510 | 0.20400 | 0 | 0.05410 |
| 103 | 104 | 0.04660 | 0.15840 | 0 | 0.04070 |
| 103 | 105 | 0.05350 | 0.16250 | 0 | 0.04080 |
| 100 | 106 | 0.06050 | 0.22900 | 0 | 0.06200 |
| 104 | 105 | 0.00994 | 0.03780 | 0 | 0.00986 |
| 105 | 106 | 0.01400 | 0.05470 | 0 | 0.01434 |
| 105 | 107 | 0.05300 | 0.18300 | 0 | 0.04720 |
| 105 | 108 | 0.02610 | 0.07030 | 0 | 0.01844 |

*Continued on next page*

Table C.11 – *Continued from previous page*

| from bus | to bus | $R$ p.u | $X_L$ p.u | $G_{shunt}$ p.u | $B_{shunt}$ p.u |
|---|---|---|---|---|---|
| 106 | 107 | 0.05300 | 0.18300 | 0 | 0.04720 |
| 108 | 109 | 0.01050 | 0.02880 | 0 | 0.00760 |
| 103 | 110 | 0.03906 | 0.18130 | 0 | 0.04610 |
| 109 | 110 | 0.02780 | 0.07620 | 0 | 0.02020 |
| 110 | 111 | 0.02200 | 0.07550 | 0 | 0.02000 |
| 110 | 112 | 0.02470 | 0.06400 | 0 | 0.06200 |
| 17 | 113 | 0.00913 | 0.03010 | 0 | 0.00768 |
| 32 | 113 | 0.06150 | 0.20300 | 0 | 0.05180 |
| 32 | 114 | 0.01350 | 0.06120 | 0 | 0.01628 |
| 27 | 115 | 0.01640 | 0.07410 | 0 | 0.01972 |
| 114 | 115 | 0.00230 | 0.01040 | 0 | 0.00276 |
| 68 | 116 | 0.00034 | 0.00405 | 0 | 0.16400 |
| 12 | 117 | 0.03290 | 0.14000 | 0 | 0.03580 |
| 75 | 118 | 0.01450 | 0.04810 | 0 | 0.01198 |
| 76 | 118 | 0.01640 | 0.05440 | 0 | 0.01356 |

Table C.12: Static Vars Compensator

| Bus | $X_C$ | $X_L$ | $R_T$ | $X_T$ | $\alpha_{SVC}$ |
|---|---|---|---|---|---|
| 48 | 9.365e-3 | 1.60e-3 | 0.0 | 0.0 | 140 |

Table C.13: TCSC data

| from bus | to bus | $X_C$ | $X_L$ | $\alpha_{TCSC}$ |
|---|---|---|---|---|
| 30 | 120 | 9.375e-3 | 1.625e-3 | 145 |

Table C.14: UPFC data

| from | to | $R_S$ | $X_S$ | $R_sh$ | $X_sh$ | $V_S$ | $\theta_S$ | $V_sh$ | $\theta_sh$ |
|---|---|---|---|---|---|---|---|---|---|
| 81 | 119 | 0.05 | 0.1 | 0.05 | 0.1 | 0.1 | 81.86 | 1.0 | 0 |

Table C.15: FSWG data

| Bus | $kV$ | $S_{nom}$ | $R_1$ | $X_1$ | $R_2$ | $X_2$ | $X_m$ | $s_0$ |
|---|---|---|---|---|---|---|---|---|
| 5 | 0.69 | -0.005 | 0.0027 | 0.025 | 0.0022 | 0.046 | 1.38 | -0.005 |
| 73 | 0.69 | 17 | 0.00 | 0.09985 | 0.00373 | 0.10906 | 3.54708 | -0.005799 |

Table C.16: SSWG data

| Bus | $kV$ | $V_w$ | $R_1$ | $X_1$ | $R_2$ | $X_2$ | $X_m$ | $R_{X,0}$ |
|---|---|---|---|---|---|---|---|---|
| 113 | 0.69 | 12 | 0.0026999631 | 0.07260525 | 0.002199582 | 0.0459998298 | 1.37997585 | -100.6981 |

Table C.17: PMSG data

| Bus | $R_st$ | $X_st$ | $V_w$ | $V_{gsc}$ | $\theta_{gsc}$ |
|---|---|---|---|---|---|
| 63 | 0.0 | 0.1 | 12 | 1.0 | 0.0 |

TABLE C.18: Control targets of FACTS controllers

| FACTS Controller | Controlled Variable | Original Value | Target Value |
|---|---|---|---|
| SVC | $V_{48}$ | 1.0206300 p.u | 1.02 p.u |
| TCSC | $P_{30-120}$ | 62.532900 MW | 80 MW |
| | $V_{81}$ | 0.996808 p.u | 1.05 p.u |
| UPFC | $P_{119-81}$ | -44.303400 MW | -70 MW |
| | $Q_{119-81}$ | -4.605200 MW | -10 MW |
| LTC | $V_{21}$ | 0.958623 p.u | 0.955 p.u |
| PS | $P_{70-121}$ | -0.140660 | 15 MW |

TABLE C.19: Generator Parameters

| Bus | Active power | | Reactive power limits | | Voltage setpoint |
|---|---|---|---|---|---|
| | MWs | MVARs | min (MVARs) | max (MVARs) | p.u. |
| 1 | 0 | 0 | -5 | 15 | 0.955 |
| 4 | -9 | 0 | -300 | 300 | 0.998 |
| 8 | -28 | 0 | -300 | 300 | 1.015 |
| 10 | 450 | 0 | -147 | 200 | 1.05 |
| 12 | 85 | 0 | -35 | 120 | 0.99 |
| 15 | 0 | 0 | -10 | 30 | 0.97 |
| 19 | 0 | 0 | -8 | 24 | 0.962 |
| 24 | -13 | 0 | -300 | 300 | 0.992 |
| 26 | 314 | 0 | -1000 | 1000 | 1.015 |
| 27 | -9 | 0 | -300 | 300 | 0.968 |
| 31 | 7 | 0 | -300 | 300 | 0.967 |
| 32 | 0 | 0 | -14 | 42 | 0.963 |
| 36 | 0 | 0 | -8 | 24 | 0.98 |
| 40 | -46 | 0 | -300 | 300 | 0.97 |
| 42 | -59 | 0 | -300 | 300 | 0.985 |
| 46 | 19 | 0 | -100 | 100 | 1.005 |
| 49 | 204 | 0 | -85 | 210 | 1.025 |
| 54 | 48 | 0 | -300 | 300 | 0.955 |
| 55 | 0 | 0 | -8 | 23 | 0.952 |
| 56 | 0 | 0 | -8 | 15 | 0.954 |
| 59 | 155 | 0 | -60 | 180 | 0.985 |
| 62 | 0 | 0 | -20 | 20 | 0.998 |
| 65 | 391 | 0 | -67 | 200 | 1.005 |
| 66 | 392 | 0 | -67 | 200 | 1.05 |
| 70 | 0 | 0 | -10 | 32 | 0.984 |
| 72 | -12 | 0 | -100 | 100 | 0.98 |
| 73 | -6 | 0 | -100 | 100 | 0.991 |
| 74 | 0 | 0 | -6 | 9 | 0.958 |
| 76 | 0 | 0 | -8 | 23 | 0.943 |
| 77 | 0 | 0 | -20 | 70 | 1.006 |
| 80 | 477 | 0 | -165 | 280 | 1.04 |
| 85 | 0 | 0 | -8 | 23 | 0.985 |
| 89 | 607 | 0 | -210 | 300 | 1.005 |
| 90 | -85 | 0 | -300 | 300 | 0.985 |
| 92 | 0 | 0 | -3 | 9 | 0.99 |
| 99 | -42 | 0 | -100 | 100 | 1.01 |
| 100 | 252 | 0 | -50 | 155 | 1.017 |
| 103 | 40 | 0 | -15 | 40 | 1.01 |
| 104 | 0 | 0 | -8 | 23 | 0.971 |
| 105 | 0 | 0 | -8 | 23 | 0.965 |
| 107 | -22 | 0 | -200 | 200 | 0.952 |
| 110 | 0 | 0 | -8 | 23 | 0.973 |
| 112 | -43 | 0 | -100 | 1000 | 0.975 |
| 113 | -6 | 0 | -100 | 200 | 0.993 |
| 116 | -184 | 0 | -1000 | 1000 | 1.005 |

TABLE C.20: Loads parameters

| Bus | Load | |
|---|---|---|
| | MWs | MVARs |
| 1 | 51 | 27 |
| 2 | 20 | 9 |
| 3 | 39 | 10 |
| 4 | 30 | 12 |
| 7 | 19 | 2 |
| 8 | 0 | 0 |
| 9 | 0 | 0 |
| 10 | 0 | 0 |
| 11 | 70 | 23 |
| 12 | 47 | 10 |
| 13 | 34 | 16 |
| 14 | 14 | 1 |
| 15 | 90 | 30 |
| 16 | 25 | 10 |
| 17 | 11 | 3 |
| 19 | 45 | 25 |
| 20 | 18 | 3 |
| 21 | 14 | 8 |
| 22 | 10 | 5 |
| 23 | 7 | 3 |
| 24 | 0 | 0 |
| 25 | 0 | 0 |
| 26 | 0 | 0 |
| 27 | 62 | 13 |
| 28 | 17 | 7 |
| 29 | 24 | 4 |
| 30 | 0 | 0 |
| 31 | 43 | 27 |
| 32 | 59 | 23 |
| 33 | 23 | 9 |
| 35 | 33 | 9 |
| 36 | 31 | 17 |
| 37 | 0 | 0 |
| 38 | 0 | 0 |
| 39 | 27 | 11 |
| 40 | 20 | 23 |
| 41 | 37 | 10 |
| 42 | 37 | 23 |
| 43 | 18 | 7 |
| 44 | 16 | 8 |
| 45 | 53 | 22 |
| 46 | 28 | 10 |
| 47 | 34 | 0 |
| 48 | 20 | 11 |
| 49 | 87 | 30 |
| 50 | 17 | 4 |
| 51 | 17 | 8 |
| 52 | 18 | 5 |
| 53 | 23 | 11 |
| 54 | 113 | 32 |
| 55 | 63 | 22 |
| 56 | 84 | 18 |
| 57 | 12 | 3 |
| 58 | 12 | 3 |
| 59 | 277 | 113 |

| Bus | Load | |
|---|---|---|
| | MWs | MVARs |
| 60 | 78 | 3 |
| 61 | 0 | 0 |
| 62 | 77 | 14 |
| 64 | 0 | 0 |
| 65 | 0 | 0 |
| 66 | 39 | 18 |
| 67 | 28 | 7 |
| 68 | 0 | 0 |
| 69 | 0 | 0 |
| 70 | 66 | 20 |
| 71 | 0 | 0 |
| 72 | 0 | 0 |
| 74 | 68 | 27 |
| 75 | 47 | 11 |
| 76 | 68 | 36 |
| 77 | 61 | 28 |
| 78 | 71 | 26 |
| 79 | 39 | 32 |
| 80 | 130 | 26 |
| 81 | 154 | 57 |
| 83 | 20 | 10 |
| 84 | 11 | 7 |
| 85 | 24 | 15 |
| 86 | 21 | 10 |
| 87 | 0 | 0 |
| 88 | 48 | 10 |
| 89 | 0 | 0 |
| 90 | 78 | 42 |
| 91 | 0 | 0 |
| 92 | 65 | 10 |
| 93 | 12 | 7 |
| 94 | 30 | 16 |
| 95 | 42 | 31 |
| 96 | 38 | 15 |
| 97 | 15 | 9 |
| 98 | 34 | 8 |
| 99 | 0 | 0 |
| 100 | 37 | 18 |
| 101 | 22 | 15 |
| 102 | 5 | 3 |
| 103 | 23 | 16 |
| 104 | 38 | 25 |
| 105 | 31 | 26 |
| 106 | 43 | 16 |
| 107 | 28 | 12 |
| 108 | 2 | 1 |
| 109 | 8 | 3 |
| 110 | 39 | 30 |
| 111 | 0 | 0 |
| 112 | 25 | 13 |
| 114 | 8 | 3 |
| 115 | 22 | 7 |
| 116 | 0 | 0 |
| 117 | 20 | 8 |
| 118 | 33 | 15 |

TABLE C.21: GLFC data

| c1 | c2 | c3 | c4 | c5 | c7 | c8 | c9 | c10 | c11 | c16 | c17 | c18 | c19 |
|---|---|---|---|---|---|---|---|---|---|---|---|---|---|
| 6 | 0 | 0.52 | 0.159260 | 0.22 | 0.04 | 0.04 | 0.2 | 0.3 | 0.5 | 0.001 | 0.2 | 0.3 | 0.5 |
| 18 | 0 | 0.6 | 0.195028 | 0.34 | 0.04 | 0.04 | 0.2 | 0.3 | 0.5 | 0.001 | 0.2 | 0.3 | 0.5 |
| 25 | 2.2 | 0 | 0.572213 | 0 | 0.04 | 0.04 | 0.2 | 0.3 | 0.5 | 0.001 | 0.2 | 0.3 | 0.5 |
| 34 | 0 | 0.59 | -0.080000 | 0.26 | 0.04 | 0.04 | 0.2 | 0.3 | 0.5 | 0.001 | 0.2 | 0.3 | 0.5 |
| 61 | 1.6 | 0 | -0.403871 | 0 | 0.04 | 0.04 | 0.2 | 0.3 | 0.5 | 0.001 | 0.2 | 0.3 | 0.5 |
| 87 | 0.04 | 0 | 0.110216 | 0 | 0.04 | 0.04 | 0.2 | 0.3 | 0.5 | 0.001 | 0.2 | 0.3 | 0.5 |
| 91 | -0.1 | 0 | -0.148017 | 0 | 0.04 | 0.04 | 0.2 | 0.3 | 0.5 | 0.001 | 0.2 | 0.3 | 0.5 |
| 111 | 0.36 | 0 | -0.018438 | 0 | 0.04 | 0.04 | 0.2 | 0.3 | 0.5 | 0.001 | 0.2 | 0.3 | 0.5 |
| 69 | 5.4851 | 0 | -1.013800 | 0 | 0.04 | 0.04 | 0.2 | 0.3 | 0.5 | 0.001 | 0.2 | 0.3 | 0.5 |

TABLE C.22: Shunt compensation data

| Bus | $G_{shunt}$ p.u | $B_{shunt}$ p.u |
|---|---|---|
| 5 | 0 | -0.4 |
| 34 | 0 | 0.14 |
| 37 | 0 | -0.25 |
| 44 | 0 | 0.1 |
| 45 | 0 | 0.1 |
| 46 | 0 | 0.1 |
| 74 | 0 | 0.12 |
| 79 | 0 | 0.2 |
| 82 | 0 | 0.2 |
| 83 | 0 | 0.1 |
| 105 | 0 | 0.2 |
| 107 | 0 | 0.06 |
| 110 | 0 | 0.06 |

# Appendix D

# Forecasting methods

## D.1 Single exponential smoothing

Exponential smoothing is a technique for smoothing time series data, for which just one parameter needs to be estimated, and is given by:

$$F_{t+1} = F_t + \alpha(Y_t - F_t) = \alpha Y_t + (1 - \alpha)F_t \tag{D.1}$$

where $F_t$ is the forecast, $Y_t$ is the observation and $\alpha$ is a constant between 0 and 1. It can be seen that the new forecast is simply the old forecast plus an adjustment for the error that occurred in the last forecast [77]. On the other hand, when $\alpha = 1$ the new forecast is simply the last observation.

## D.2 Holt's linear method

Holt's linear method was designed to handle trends and it consists of the following recursive equations [77]:

$$L_t = \alpha Y_t + (1 - \alpha)(L_{t-1} + b_{t-1}) \tag{D.2}$$

$$b_t = \beta(L_t - L_{t-1}) + (1 - \beta)b_{t-1} \tag{D.3}$$

$$F_{t+m} = L_t + b_t m \tag{D.4}$$

where $L_t$ denotes an estimate of the level of the series at time $t$ and $b_t$ denotes an estimate of the slope of the series at time t. Equation 3.4 adjusts $L_t$ directly for the

trend of the previous period, $b_{t-1}$, by adding it to the last smoothed value, $L_{t-1}$. Equation 3.5 then updates the trend which is modified by smoothing parameter $\beta$. Finally, $m$ is the number of periods ahead to be forecast. The implementation of Holt linear method for state forecasting is explained in [51].

# Bibliography


[1] S. C. Savulescu, *Real-Time Stability Assessment in Modern Power System Control Centers*. IEEE Press Wiley, 2009.

[2] A. G. Exposito, A. J. Conejo, and C. Cañizares, *Electric energy systems analysis and operation*. Taylor & Francis Group, LLC, 2009.

[3] A. Farzanehrafat and N. R. Watson, "Review of power quality state estimation," in *20th Australasian Universities Power Engineering Conference (AUPEC)*, Christchurch, December 2010.

[4] F. Li, W. Qiao, H. Sun, H. Wan, J. Wang, Y. Xia, Z. Xu, and P. Zhang, "Smart transmission: vision and framework," *IEEE Trans. Smart Grid*, vol. 1, pp. 168–177, September 2010.

[5] A. Bose, "Smart transmission grid applications and their supporting infrastructure," *IEEE Trans. Smart Grid*, vol. 1, pp. 11–19, June 2010.

[6] A. Phadke and J. Thorp, "History and applications of phasor measurements," in *Power Systems Conference and Exposition 2006*, Atlanta, GA USA, November 2006, pp. 331–335.

[7] A. Phadke, "Synchronized phasor measurements in power systems," *IEEE Comput. Appl. Power*, vol. 6, pp. 10–15, April 1993.

[8] A. Gomez-Exposito, A. Abur, P. Rousseaux, A. de la Villa Jaen, and C. Gomez-Quiles, "On the use of pmus in power system state estimation," in *17th Power Systems Computation Conference 2011*, Stockholm, Sweden, August 2011, pp. 1–13.

[9] A. Wood and B. Wollenberg, *Power Generation, Operation, and Control*. John Wiley & Sons, New York, NY, 1996.

[10] A. Gomez-Exposito, A. Abur, A. de la Villa Jaen, and C. Gomez-Quiles, "A multilevel state estimation paradigm for smart grids," in *Proc. IEEE 99*, April 2011, pp. 952–976.

[11] G. Korres, "A distributed multiarea state estimation," *IEEE Trans. Power Syst*, vol. 26, pp. 73–84, April 2010.

[12] M. Zhou, V. Centeno, J. Thorp, and A. Phadke, "An alternative for including phasor measurements in state estimators," *IEEE Trans. Power Syst.*, vol. 21, pp. 1930–1937, November 2006.

[13] T. Bi, X. Qin, and Q. Yang, "A novel hybrid state estimator for including synchronized phasor measurements," *Electr. Power Syst. Res.*, vol. 78, pp. 1343–1352, August 2008.

[14] E. A. A. Abur, B. Gou, "State estimation of networks containing power flow control devices," in *13th Power Systems Computation Conference 1999*, Trondheim, Norway, June 1999, pp. 427–433.

[15] A. Zamora-Cárdenas and C. Fuerte-Esquivel, "State estimation of power systems containing facts controllers," *Electr. Power Syst. Res.*, vol. 81, pp. 995–1002, April 2011.

[16] S. Gsanger and J. D. Pitteloud, "World wind energy report 2012," in *XII World Wind Energy Conf. & Renew. Energy Exhibition*, Havana, Cuba, June 2013.

[17] L. Zhao and A. Abur, "Multiarea state estimation using synchronized phasor measurements," *IEEE Trans. Power Syst.*, pp. 611–617, May 2005.

[18] W. Jiang, V. Vittal, and G. Geydt, "A distributed state estimator utilizing synchronized phasor measurements," *IEEE Trans. Power Syst.*, vol. 22, pp. 563–571, May 2007.

[19] Q. Huang, N. Schulz, A. Srivastava, and T. Haupt, "Distributed state estimation with pmu using grid computing," in *IEEE Power Engineering Society General Meeting 2009*, Calgary, AB, July 2009, pp. 1–7.

[20] J. Zhu and A. Abur, "Effect of phasor measurements on the choice of reference bus for state estimation," in *IEEE Power Engineering Society General Meeting 2007*, Tampa, FL USA, June 2007, pp. 1–5.

[21] G. Korres and N. Manousakis, "State estimation and bad data processing for systems including pmu and scada measurements," *Electr. Power Syst. Res.*, vol. 81, pp. 1514–1524, July 2011.

[22] S. Chacrabarti, E. Kyriakides, G. Ledwich, and A. Ghosh, "Inclusion of pmu current phasor measurements in a power system state estimator," *IET Generat. Transm. Distrib.*, vol. 4, pp. 1104–1115, October 2010.

[23] D. Qifeng, Z. Boming, and T. Chung, "State estimation for power systems embedded with facts devices and mtdc systems by a sequential solution approach," *Electr. Power Syst. Res.*, vol. 55, pp. 147–156, September 2010.

[24] B. Xu and A. Abur, "State estimation of systems with upfcs using the interior point method," *IEEE Trans. Power Syst.*, vol. 19, pp. 1635–1641, August 2004.

[25] C. Rakpenthai, S. Premrudeepreechacharn, S. Uatrongjit, and N. Watson, "An interior point method for wlav state estimation of power system with upfcs," *Int. J. Electr. Power Energy Syst.*, vol. 32, pp. 671–677, July 2010.

[26] A. D. la Villa Jaen, E. Acha, and A. G. Exposito, "Voltage source converter modeling for power system state estimation: Statcom and vsc-hvdc," *IEEE Trans. Power Syst.*, vol. 23, pp. 1552–1559, September 2008.

[27] S. Gou-qiang and W. Zhi-nong, "Power system state estimation with unified power flow controller," in *i-nong, Power system state estimation with unified power flow controller, in: Third International Conference on Electric Utility Deregulation and Restructuring and Power Technologies*, Nanjing, China, April 2008.

[28] B. Xu and A. Abur, "State estimation of systems with embedded facts devices," in *Proc. Powertech Conf.*, Bologna Italy, June 2003.

[29] C. Rakpenthai, S. Premrudeepreechacharn, S. Uatrongjit, and N. R. Watson, "State estimation of power system with upfc using interior point wlav method," in *Proc. of 38th North American Power Symposium (NAPS)*, Carbondale, IL, September 2006.

[30] C. Rakpenthai, S. Premrudeepreechacharn, and S. Uatrongjit, "Power system with multi-type facts devices state estimation based on predictor-corrector interior point algorithm," *Electr. Power Energy Syst.*, vol. 31, pp. 160–166, May 2009.

[31] G. Q. Sun, Z. N. Wei, and B. Pang, "Impact of wind generators on power system state estimation," in *Proc. Sust. Power Gen. and Supply Conf*, Nanjing China, April 1999, pp. 1–4.

[32] ——, "Power system state estimation containing wind generators," in *Proc. Power and Energy Eng. Conf. (APPEEC 2009)*, Asia-Pacific, 20009.

[33] A. Rankovic and A. T. Saric, "Modeling of photovoltaic and wind turbine based distributed generation in state estimation," in *Proc. 15th EPE-PEMC 2012 ECCE Europe*, Novi Sad, September 2012.

[34] Z. Wei, X. Yang, G. Q. Sun, Y. Sun, and P. Ju, "Wind power system state estimation with automatic differentiation technique," *Int. J. Electr. Power Energy Syst.*, vol. 53, pp. 297–306, December 2013.

[35] P. W. Carlin, A. S. Laxson, and E. B. Muljadi, "The history and state of the art of variable-speed wind turbine technology," Natl. Renew. Energy Lab., Tech. Rep., 2001. [Online]. Available: http://www.nrel.gov/docs/fy01osti/28607.pdf

[36] C. R. Fuerte-Esquivel, J. H. Tovar-Hernandez, G. Gutierrez-Alcaraz, and F. Cisneros-Torres, "Discussion of modeling of wind farms in the load flow analysis," *IEEE Trans. Power Syst.*, vol. 16, p. 951–951, November 2001.

[37] L. M. Castro, C. R. Fuerte-Esquivel, and J. H. Tovar-Hernandez, "A unified approach for the solution of power flows in electric power systems including wind farms," *Electr. Power Syst. Res..*, vol. 81, pp. 1859–1865, October 2011.

[38] ——, "Solution of power flow with automatic load-frequency control devices including wind farms," *IEEE Trans. Power Syst.*, vol. 27, pp. 2186–2195, November 2012.

[39] S. Li, "Power flow modeling to doubly-fed induction generators (dfigs) under power regulation," *IEEE Trans. Power Syst.*, vol. 28, pp. 3292–3301, August 2013.

[40] P. Sorensen, N. A. Cutululis, A. Vigueras-Rodriguez, L. E. Jensen, J. Hjerrild, M. Donovan, and H. Madsen, "Power fluctuations from large wind farms," *IEEE Trans. Power Syst.*, vol. 22, pp. 958–965, August 2007.

[41] J. G. Slootweg and W. L. Kling, "The impact of large scale wind power generation on power system oscillations," *Electr. Power Syst. Res.*, vol. 67, pp. 9–20, October 2003.

[42] M. Okamura, Y. O-ura, S. Hayashi, K. Uemura, and F. Ishiguro, "A new power flow model and solution method including load and generator characteristics and effects of system control devices," *IEEE Trans. Power App. Syst.*, vol. PAS-94, no. 3, pp. 1042—-1050, May 1975.

[43] E. A. Zamora-Cardenas, B. A. Alcaide-Moreno, and C. R. Fuerte-Esquivel, "State estimation of flexible ac transmission systems considering synchronized phasor measurements," *Electr. Power Syst. Res.*, vol. 106, pp. 120–133, January 2014.

[44] J. L. H. T. Van Cutsem and M. Ribbens-Pavela, "A two level static state estimator for electric power systems," *IEEE Trans. Power App. Syst.*, vol. PAS-100, pp. 3722–3732, August 1981.

[45] A. Gomez-Exposito, A. de la Villa Jaen, C. Gomez-Quiles, P. Rousseaux, and T. Van Cutsem, "A taxonomy of multiarea state estimation methods," *Electr. Power Syst. Res.*, vol. 81, pp. 1060–1069, April 2011.

[46] A. R. Khatib, L. Milli, A. Phadke, J. D. L. Ree, and Y. Liu, "Internet based wide area information sharing and its roles in power system state estimation," in *Proc. 2001 IEEE PES General Meeting Conf.*, Columbus, OH, June 2001.

[47] A. S. Debs and R. E. Larson, "A dynamic state estimator for tracking the state of power sytems," *IEEE Trans. Power App. and Syst.*, vol. PAS-89, pp. 1670–1678, September 1970.

[48] R. Masiello and F. C. Schweppe, "A tracking state estimator," *IEEE Trans. Power App. and Syst.*, vol. PAS-90, pp. 1025–1033, March 1971.

[49] D. M. Falcao, P. A. Cooke, and A. Brameller, "Power system tracking state estimation and bad data processing," *IEEE Trans. Power App. Syst.*, vol. PAS-101, pp. 325–333, February 1982.

[50] W. W. Kotiuga, "Development of a least absolute value power system tracking state estimator," *IEEE Trans. Power App. Syst.*, vol. PAS-104, pp. 1160–1166, May 1985.

[51] A. M. L. da Silva, M. B. D. C. Filho, and J. F. de Queiroz, "State forecasting in electric power systems," *Proc. IEE on Gener, Transm. and Distrib.*, vol. 30, pp. 237–244, September 1983.

[52] M. Brown, D. C. Filho, and J. C. S. de Souza, "Forecasting-aided state estimation - part i: Panorama," *IEEE Trans. Power Syst.*, vol. 24, pp. 1667–1677, November 2009.

[53] A. Abur and A. G. Exposito, *Power system state estimation: theory and implementation.* New York: Marcel Dekker, 2004.

[54] A. G. Phadke and J. S. Thorp, *Synchronized Phasor Measurements and Their Application.* New York: Springer, 2008.

[55] M. Pignati, L. Zanni, S. Sarri, R. Cherkaoui, J.-Y. L. Boudec, and M. Paolone, "A pre-estimation filtering process of bad data for linear power systems state estimators using pmus," in *Proc. 18th Power System Computation Conference (PSCC)*, Wroclaw, Poland, August 2014.

[56] S. Wang, W. Gao, and A. P. S. Meliopoulos, "An alternative method for power system dynamic state estimation based on unscented transform," *IEEE Trans. Power Syst.*, vol. 27, no. 2, pp. 942–950, May 2012.

[57] P. Zhang, F. Li, and N. Bhatt, "Next-generation monitoring, analysis, and control for the future smart control center," *IEEE Trans. Smart Grid*, vol. 1, no. 2, pp. 186–192, September 2010.

[58] M. Zhou, V. A. Centeno, J. S. Thorp, and G. Phadke, "An alternative for including phasor measurements in state estimators," *IEEE Trans. Power Syst.*, vol. 21, no. 4, pp. 1930–1937, November 2006.

[59] A. S. Costa, A. Albuquerque, and D. Bez, "An estimation fusion method for including phasor measurements into power system real-time modeling," *IEEE Trans. Power Syst.*, vol. 28, no. 2, pp. 1910–1920, May 2013.

[60] M. Glavic and T. Van Cutsem, "Reconstructing and tracking network state from a limited number of synchrophasor measurements,," *IEEE Trans. Power Syst.*, vol. 28, p. 1921–1929, May 2013.

[61] ——, "Tracking network state from combined scada and synchronized phasor measurements," in *Bulk Power Systems Dynamics and Control-IX (IREP)*, Rethymnon (Greece), August 2013. [Online]. Available: IEEEXplore,DOI:10.1109/IREP.2013.6629376

[62] M. Gol and A. Abur, "A hybrid state estimator for systems with limited number of PMUs," *IEEE Trans. Power Syst.*, vol. 30, pp. 1511–1517, August 2015.

[63] M. Asprou, S. Chakrabarti, and E. Kyriakides, "A two-stage state estimator for dynamic monitoring of powersystems," *IEEE Systems Journal*, vol. PP, pp. 1–10, December 2014.

[64] H. Karimipour and V. Dinavahi, "Extended kalman filter-based parallel dynamic state estimation," *IEEE Trans. Smart Grid*, vol. 6, pp. 1539–1549, January 2015.

[65] J. Zhao, G. Zhang, K. Das, G. N. Korres, N. M. Manousakis, A. K.Sinha, and Z. He, "Power system real-time monitoring by using pmu-based robust state estimation method," *IEEE Trans. Smart Grid*, vol. pp, no. 99, pp. 1–10, May 2015.

[66] R. F. Nuqui, "State estimation and voltage security monitoring using synchronized phasor measurements," Ph.D. dissertation, Virginia Polytech. Inst. State Univ., Blacksburg, A., Jul 2001.

[67] B. A. Alcaide-Moreno, C. R. Fuerte-Esquivel, M. Glavic, and T. Van Cutsem, "Hybrid processing of scada and synchronized phasor measurements for tracking network state," in *IEEE PES General Meeting*, Denver (CO), July 2015.

[68] G. N. Korres, A. Tzavellas, and E. Galinas, "A distributed implementation of multi-area power system state estimation on a cluster of computers," *Electr. Power Syst. Res.*, vol. 102, pp. 20–32, September 2013.

[69] I. Slutsker, S. Mokhtari, L. Jaques, J. Gonzalez, M. Baena, J. Benaventa, F. Gonzalez, and J. Montes, "Implementation of phasor measurements in state estimator at sevillana de electricidad," in *Power Industry Computer Application Conference*, Salt Lake City, UT, June 1995.

[70] A. Monticelli, "Electric power system state estimation," in *Proceedings of the IEEE*, vol. 88, February 2000, pp. 262–282.

[71] C. Fuerte-Esquivel, E. Acha, S. Tan, and J. Rico, "Efficient object oriented power systems software for the analysis of large-scale networks containing facts-controlled branches," *IEEE Trans. Power Syst.*, vol. 13, no. 2, pp. 464–472, 1998.

[72] P. A., *Probanility Random Variables, and Stocastic Processes.* Mc Graw Hill, 1989.

[73] Power systems test cases archive university of washington. [Online]. Available: http://www.ee.washington.edu/research/pstca/

[74] J. Zhu, A. Abur, M. J. Rice, G. T. Heydt, and S. Meliopolus, "Enhanced state estimators," Power Syst. Eng. Res. Center, Tech. Rep., 2006. [Online]. Available: http://www.pserc.wisc.edu/documents/publications/reports/2006reports/aburstateestimatorss22reports.pdf

[75] R. Ramirez-Betancour, V. J. Gutierrez-Martinez, and C. R. Fuerte-Esquivel, "Static simulation of voltage instability considering effects of governor characteristics and voltage and frequency dependence of loads," in *Proc. 2010 North American Power Symp.*, Arlington, TX, September 2010.

[76] K. C. Budka, J. G. Deshpande, and M. Thottan, *Communication Networks for Smart Grids: Making Smart Grid Real*. New York: Springer, 2014.

[77] S. Makridakis and S. Wheelwright, *Forecasting methods and applications*. John Wiley and Sons, 1978.

[78] T. Van Cutsem, "Test systems for voltage stability and security analysis - PES-TR19," IEEE PES, Tech. Rep., August 2015. [Online]. Available: http://resourcecenter.ieee-pes.org/

[79] P. Aristidou and T. Van Cutsem. (2014, September) An overview of ramses (rapid multiprocessor simulation of electric power systems). introduction_to_RAMSES.pdf. [Online]. Available: http://www.montefiore.ulg.ac.be/~vct/software/

[80] A. P. S. Meliopoulos, *Power System Modeling, Analysis and Control*. Georgia Institute of Technology, 1990–2006.

[81] , "IEEE Standard for SCADA and Automation Systems," *IEEE Std C37.1-2007*, pp. 1 – 134, 2008.

[82] , "IEEE Standard for Synchrophasor Measurements for Power Systems," *IEEE Std C37.118.1-2011*, pp. 1 – 49, 2011.

[83] E. Acha, C. R. Fuerte-Esquivel, and H. Ambriz-Perez, *FACTS: Modeling and Simulation in Power Networks*. London, U.K.: Wiley, 2004.

[84] T. Van Cutsem and L. Papangelis, "Description, modeling and simulation results of a test system for voltage stability analysis (version 6)," University of Liège, Belgium, Tech. Rep., November 2013.